

Fatigue, fracture and damage of synthetic polymers

by

Guillaume Lostec

B.S., Université Paris-Saclay, 2016

M.S., Université Paris-Saclay, 2018

A thesis submitted to the
Faculty of the Graduate School of the
University of Colorado in partial fulfillment
of the requirements for the degree of
Doctor of Philosophy
Department of Mechanical Engineering
2025

Committee Members:

Rong Long, Chair

Yida Zhang

Francois Barthelat

Maryam Shakiba

Jianliang Xiao

Lostec, Guillaume (Ph.D., Mechanical Engineering)

Fatigue, fracture and damage of synthetic polymers

Thesis directed by Prof. Rong Long

In this dissertation, I first propose a continuum theory of fatigue fracture in viscoelastic solids. I predict the crack extension per loading cycle for various loading amplitudes, loading frequencies and viscoelastic properties. This is achieved by examining the energy dissipated through viscous effects and the energy available for driving crack growth. In particular, energy dissipation is controlled by an interplay of three time scales: the material relaxation time, the timescale associated with crack propagation (i.e., crack speed) and the loading frequency. By tracking the stress history of material points around the crack tip under concurrent crack propagation and cyclic loading, I derive an integral equation governing crack speed within a loading cycle. Comparisons between numerical solutions of the theory and finite element simulations demonstrate that it predicts the influence of material parameters and loading conditions on fatigue fracture at a much lower computational cost.

The second part of this work focuses on the interpretation of toughness measurements in neo-Hookean solids with Mullins effect. Specifically, I present a series of finite element simulations of pure shear fracture tests, where I varied the sample geometry and the material properties to study their influence on toughness measurements. Based on my results, I provide guidelines to meaningfully compare different materials through simple mechanical tests.

Finally, in the last part of this dissertation I propose a multi-scale modeling approach to understand damage in carbon fiber reinforced polymers.

Dedication

To my wife Kristen, mon frère Alexis, ma sœur Kiara, et mes parents.

Acknowledgements

First I want to thank Rong Long. He is an inspiring researcher, a great teacher and a patient and helpful academic advisor. His good mood and scientific curiosity are contagious.

I would also like to thank my labmates and friends Hemant, Hendrik, Huiqi, Saleh, Xingwei and Salil. I enjoyed drinking coffee and learning with you all. I was also lucky to learn a great deal from students in my first lab, in particular my friends Shankar, Tong, Sam and Rob.

And finally, I want to thank Anna Guy for helping me navigate the administrative hurdles that come with being an international student. She is very helpful and compassionate.

Contents

Chapter

1	Introduction	1
2	Background	3
2.1	Structure and mechanics of synthetic polymers	3
2.1.1	Structure	3
2.1.2	Mechanical behavior of synthetic polymers	4
2.1.3	Free energy imbalance	8
2.1.4	Constitutive modeling of synthetic polymers	10
2.2	Fracture of synthetic polymers	13
2.2.1	Basic concepts	14
2.2.2	Fundamentals of linear elastic fracture mechanics	16
2.2.3	Fracture of synthetic polymers	20
2.2.4	Fatigue fracture of synthetic polymers	24
3	A theory of fatigue fracture in viscoelastic solids	28
3.1	Introduction	28
3.2	Energy Balance and Fracture Criterion	32
3.2.1	Thermodynamics	32
3.2.2	Fracture criterion	37
3.2.3	Energy release rates	39

3.3	Material Behavior	40
3.3.1	Linear viscoelasticity	41
3.3.2	Correspondence principle and stress field	42
3.3.3	Creep compliance	44
3.3.4	Free energy density	45
3.4	The Pure Shear Problem	46
3.4.1	Simplifying assumptions	46
3.4.2	Importance of the far field	50
3.4.3	The phantom state	51
3.4.4	Limitations	52
3.4.5	Beyond pure shear fracture	54
3.5	Numerical Methods	55
3.5.1	Implicit scheme	55
3.5.2	Numerical spatial integration	56
3.5.3	The spatial integral $\mathcal{D}_{cc'}$ as a function of crack extension	59
3.5.4	Limiting crack speed	61
3.6	Results and Discussion	61
3.6.1	Comparison to finite element simulations	61
3.6.2	Fatigue fracture behavior	65
3.6.3	Dynamic effect	70
3.6.4	Influence of the polarization	73
3.7	Conclusion	75
4	Fracture toughness of soft solids with Mullins effect	78
4.1	Introduction	78
4.2	Model	80
4.2.1	Material model	80

4.2.2	Pure shear fracture test	83
4.2.3	Power budget	83
4.2.4	Energy release rate for steady state crack propagation	86
4.3	Finite elements simulations	87
4.3.1	ABAQUS model	87
4.3.2	Post-processing	87
4.4	Results	90
4.4.1	Shape of the resistance curve	90
4.4.2	Toughness: definition and interpretation	92
4.4.3	Effect of the sample height	101
4.5	Conclusion	103
5	Investigating the mechanical failure mechanisms of a novel CFRP composite to inform computational models	105
5.1	Introduction	105
5.2	Methods	107
5.2.1	Problem breakdown	107
5.2.2	Preparation of the samples	107
5.2.3	Experimental testing	109
5.2.4	Multiscale modeling of CFRPs mechanics	109
5.2.5	Reduced model	112
5.3	Results	113
5.3.1	Stress relaxation under low stretch	113
5.3.2	DMA: model prediction	115
5.3.3	Scanning Electron Microscopy results	116
5.4	Preliminary conclusion and future work	117
5.4.1	Experimental plan to study damage	118

5.4.2 Extension of the model to study damage	119
6 Summary and future work	121

Bibliography	123
---------------------	------------

Appendix

A Cohesive zone model and the fracture energy	134
B Standard linear solid: creep compliance and free energy	136
B.0.1 Creep compliance	136
B.0.2 Free energy	137
C Intrinsic energy release rate for the pure shear configuration	140
D Nominal intrinsic energy release rate in the phantom state	141
E Derivatives of spatial distribution	143
F Gains in computational time	145
F.0.1 Computational time for the numerical method	145
F.0.2 Computational time for the FEA simulation	146
G Influence of the ratio T/τ: supplementary data	148
H Table of parameters for the finite element simulations	149

Tables

Table

Figures

Figure

2.1	(a) Sample scale. (b) Micrometer scale, showing filler aggregates. (c) Molecular network at $\sim 100\text{nm}$ scale, showing entangled and crosslinked polymer chains.	4
2.2	(a) Elastic behavior of synthetic polymers. Comparison to metallic materials. (b) Mullins effect in synthetic polymers.	5
2.3	(a) Eight-chain model of Arruda and Boyce. (b) Full network model, as in transient network theories, with the Gaussian distribution represented in 2D. (c) Microsphere model, where each facet of the polyhedron represents a direction in the chain configuration space.	12
2.4	(a) Schematic associated to Eq.(2.16). (b) The three modes of fracture.	17
2.5	(a) Uncracked body. (b) Cracked body. (c) Gurtin's domain.	19
2.6	(a) Pure shear strip, points A, P, B are taken on a line $y = Y$ at different distances x . (b) Tensile component of stress at points A, P, B for three times t_A, t_P, t_B corresponding to when the crack tip was under each point. (c) Tensile stress at point P , over time.	23

2.7 (a) Rate of crack propagation per cycle dc/dN at tearing energy G_{max} for SBR. Data gathered by Lake, reproduced from [69]. (b) Fracture energy at reduced propagation velocity for different materials. Reproduced from [18]. (□) SBR, data from Gent <i>et al</i> [33]. (◇) Polyurethane rubber, data from Cristiano <i>et al</i> [19]. (△) Double network hydrogel, data from Tanaka <i>et al</i> [132]. (●) Gelatin gel, data from Baumberger <i>et al</i> [7].(c) Experimental evidence for the dynamic effect: $A(f)$ is the coefficient of Eq.(2.30). Frequency is given in <i>cpm</i> , meaning cycles/min and $1/A(f)$ in c.g.s units (centimeter-gram-second system). Reproduced from [71].	25
3.1 (a) Kinematics of a cracked continuum body. We denote Ω the continuum in the reference configuration and Ω_t at time t in the deformed configuration. The same logic is applied to the crack areas A and A_t . (b) Crack surface A delimited by crack front \mathcal{C} . The orange shaded area corresponds to the extension dA happening over the time interval dt	33
3.2 (a) Illustration of a process zone around the moving crack tip. (b) Mechanistic representation of the process zone by a cohesive zone model.	35
3.3 Extended correspondence principle for a 2D Mode-I semi-infinite crack in an infinite solid. The boundary regions B_1 and B_2 represent the crack surface and the surface directly ahead of the crack tip. Crack propagation causes both B_1 and B_2 to vary with time.	42
3.4 (a) Pure shear strip with $H \ll L_s$, initial crack length $c_0 \ll L_s$ and thickness $w \ll L_s$. The material point located at \mathbf{X} in the fixed reference frame $(\mathbf{e}_1, \mathbf{e}_2)$ is denoted \mathbf{X}_c in the translating reference frame centered at the moving crack tip. (b) Biaxially loaded center-cracked plate. (c) Single edge notch configuration. (d) Simple extension configuration.	47

- 3.7 (a) History of various energy release rates over three loading cycles. The maximum value of the energy release rate G_{FEA} in the FEA simulation is set to match the maximum value of G imposed in the theory. The dissipative energy release rate G_d^s is computed numerically according to Section 3.5. The match with imposed $(G_d^s)_{im}$ is proof for the validity of the numerical solution. Note the mismatch at the end of each cycle during unloading: see comments in Section 3.6.1.4. (b) Illustration of the cut-off length l assumed in theory and the cohesive zone with bilinear traction-separation law implemented in the FEA simulation. (c) Crack length over time: comparison between FEA simulation and theory solutions. $\rho_s = 0.735$ is obtained such that $c(3T)/c_{FEA}(3T) = \rho_s l/\delta_m$. (d) Crack speed within the first cycle: comparison of FEA and theory results. 63
- 3.8 (a) Increase in crack size per cycle as a function of the maximum global energy release rate. $\bar{c} = c/l$ is the normalized crack size, N is the number of cycles and $G_{max} = G(t = T/2)$ is the maximum value of G achieved during a cycle. The plots are provided on a base 10 logarithm scale. The green plot shows crack length increase for the first cycle (FC), the black plot for the first 5 cycles (F5C), the blue plot for all 40 cycles (AC), and the red plot for all but the first cycle (ABFC) or any of the subsequent cycles (SC). (b) The slope m of the curves in (a). The departure of the FC from the SC curve defines the initial regime (i) and the critical regime (ii). (c) For two given values $G_{max}/\Gamma_0 = 10^{1.5}$ and $G_{max}/\Gamma_0 = 10^2$ in regime (ii), the value of $G(t)/\Gamma_0$ is provided. (d) The resulting $\bar{c}(t) = c(t)/l$ is plotted and we highlighted the increase per cycle for FC, F5C and SC. (e) The dotted lines correspond to the FC curves while the plain lines are the SC curves, for each value of T/τ . (f) $\Delta c_{cy} = \bar{c}(NT) - \bar{c}((N-1)T)$ is the increase in normalized crack length per cycle N . The data is provided for $T/\tau = 100$ and $G_{max}/\Gamma_0 = 10^2$, corresponding to the last point of the blue plot on (e). (g) Similar to (f), but for $T/\tau = 10$ and $G_{max}/\Gamma_0 = 2.2$ (last point of the black plot on (e)). 68

3.9 (a) Increase in normalized crack length $\bar{c} = c/l$ per cycle N with normalized maximum global energy release rate G_{max}/Γ_0 , for varying E_0/E_∞ and fixed $T/\tau = 100$. (b) Same data for varying T/τ and fixed $E_0/E_\infty = 8$.	70
3.10 (a) History of $G(t)/\Gamma_0$ within a loading cycle. For a given time, the value $G(t^*)$ is recorded and reported on plot (c). (b) Corresponding crack speed within the cycle, solved using the numerical method in Section 3.5. The area under the curve is the crack extension per cycle under cyclic loading Δc_{cy} . (c) For static loading with energy release rate G/Γ_0 , the constant crack speed \bar{V}_{st} is predicted (Section 3.5). This result is used to predict the crack speed $\bar{V}_{st}(t^*)$ at a given time t^* corresponding to the value $G(t^*)$. It allows one to obtain (d) from (a). (d) At all times within a cycle, the static loading equivalent for the crack speed \bar{V}_{st} is obtained by considering the operating $G(t)$ and using (c). The area under the curve is the crack extension per cycle under equivalent static loading Δc_{st} . (e) The ratio $\Delta c_{cy}/\Delta c_{st}$ is a measure of the dynamic effect due to cyclic loading at period T . It is plotted for 200 values of T/τ , with τ being constant (i.e., the same material). Results are provided for increasing values of E_0/E_∞ . (f) The curves on (d) can be partially collapsed by plotting against T/τ_c , with $\tau_c = E_0/E_\infty \tau$.	71
3.11 (a) Crack extension per cycle versus the maximum global energy release rate for different polarization values p (with $T/\tau = 100$ and $E_0/E_\infty = 8$ kept constant). (b) History of the energy release rates in two loading cycles for $p = 0.5$ (black arrow on (a)). The first cycle starts with $G(0) = 0$ but is unloaded only up to $G_{min} = pG_{max}$. The subsequent cycles start from and end at G_{min} . (c) The resulting normalized crack extension \bar{c} . Data is given for the points on (a) indicated by the arrows. Note only the extension in the second cycle is accounted for to define $d\bar{c}/dN$ on (a).	74

4.1 (a) Tensile stress P_{22} for different values of α . (b) Energy density dissipated within a cycle of loading-unloading for different values of α . The red line is the linear fit with determination coefficient 0.997.	82
4.2 Pure shear fracture test with a thin-sheet strip sample geometry (i.e., $L \gg 2H$). The top and bottom boundaries of the sample are fixed to two rigid grips that are separated by a displacement loading.	84
4.3 (a) Original mesh of the pure shear sample (for clarity we show a coarser mesh than that used for simulations). The damage zone defined by the contour given as Eq.4.17 is represented: it does not follow the mesh since the field ϕ is interpolated inside elements. The true area of the damage zone is colored in red. (b) A finer, uniform mesh is created and Φ_e is calculated for all its elements. Elements $\{1..E\}$ as defined per Eq.(4.19) are colored in blue. The area of the blue elements provides a numerical approximation of the area of the damage zone.	89
4.4 (a) Resistance curve. The operational ERR \mathcal{G} is normalized by the fracture toughness imposed through the cohesive zone model (CZM) and the increase in crack length $c - c_0$ is normalized by the maximum separation δ enforced in the CZM. The points labeled I (for initiation) and P (for peak) correspond to $c > c_0$ and $F(P) = \max(F)$ respectively. The parameters used in the simulation are listed in Table H.1 (SIM-A). The gray plot corresponds to the resistance curve of an ideally elastic material. (b) Corresponding force-stretch curves. (a) Evolution of the size of the damage zone \tilde{S}_Z (normalized by the half height of the sample) with crack extension. (d) Snapshots of the field $\phi(\mathbf{X}, \lambda)$ over the undeformed domain, for the points A, P, B and C labeled on Fig.(4.4c). For each plot, the colorbar is rescaled to the extrema of $\phi(\lambda_*)$ where λ_* is the value of stretch at that specific point. The red line represents the crack. In blue, we show the damage zone $\mathcal{Z}(\lambda, \nu = 0.5)$, growing between points A and C. . .	91

4.7 (a) Resistance curves for varying α . The competition of $d\mathcal{G}/d\lambda$ with $dc/d\lambda$ leads to the slope of the resistance curve $d\mathcal{G}/dc$. (b) Rates of increase of \mathcal{G}/Γ_0 and c/L with λ after the force peak. (c) Force-stretch curves for varying α . The force peak is labeled (P). The slope of the curve $dF/d\lambda$ drops after the peak. (d) Slope of the resistance curves after the force peak. For all values of α , the slope drops to almost zero and takes longer propagation for increasing α . (e) The drop in the slope of the resistance curve is correlated to a sharp drop in the slope of the force-stretch curve. Retaining the points for which the drop in force is larger than a limiting value ($-dF/d\lambda > 40N$) ensures the increase of \mathcal{G}/Γ_0 with further crack extension remains slow. (f) The values of \mathcal{G}/Γ_0 for the points filtered using this criterion are reported for each value of α . The lowest measurement is controlled by the filtering criterion while the largest is controlled by the length of the sample. Parameters are listed in Table H.1 (SIM-F).	99
4.8 (a) Resistance curves for increasing sample height. The initiation points are labeled (I). (b) Force-stretch curves for increasing sample height. Other parameters are listed in Table H.1 (SIM-G).	101
4.9 (a) Increase in the size of the damage zone with crack extension for different H . (b) Same data with the size of the damage zone normalized by H . Parameters are listed in Table H.1 (SIM-G).	102
5.1 (a) Elementary volume of material containing the polymer network. (b) In the conformation space Ω , \mathbf{r} represents chains end-to-end vectors. (c) The distribution $P(\mathbf{r})$ projected over $(\mathbf{e}_1, \mathbf{e}_2)$, the components of $\boldsymbol{\mu}$ measure average chain stretch in principal directions. A 1d projection is also provided: note the typically higher likelihood of short versus long chains.	111

B.1	Schematic representation of the standard linear solid model under uniaxial tension. The differential equation between $\sigma(t)$ and $\epsilon(t)$ is obtained from the spring/dashpot models and the rules of parallel/series components.	136
B.2	Standard linear solid model. Total strain ϵ , strain in the dashpot γ , stress in the top branch σ and stress in the Maxwell branch q	137
G.1	(a) Increase in normalized crack length $\bar{c} = c/l$ per cycle N with normalized max- imum global energy release rate G_{max}/Γ_0 , for varying T/τ and $E_0/E_\infty = 2$. (b) Same result for $E_0/E_\infty = 4$. (c) Same result for $E_0/E_\infty = 12$	148

Chapter 1

Introduction

Polymers: polus-meros: many-parts. These materials are made of many long chains of repeating molecules, intertwined and sometimes chemically crosslinked into a network. Picture a bowl of spaghetti (chains) connected by cheese (crosslinks). Above their glass transition temperature, these molecular networks are affected by thermal fluctuations and low energy interactions. Their mechanical behavior emerges from the dynamic re-organization of their network under load. In nature, bio-polymers produced by the cells of living organisms are involved in reproduction, growth, and movement. In engineering, synthetic polymers are used as adhesives, joints or tires for their ability to sustain large deformations and dissipate energy without permanent alteration.

Fatigue corresponds to the progressive propagation of cracks in materials under prolonged cyclic loading of low amplitude: it is an important failure mode in tires, sealants or dampeners. Damage refers to the irreversible alteration of a material: it can lead to cracking when it becomes localized, but also consumes the energy available to propagate existing cracks, which helps preventing the failure of components. Establishing a more comprehensive picture of the fatigue, fracture and damage of synthetic polymers is desirable to enhance the reliability, durability and performances of polymer-based components for industrial applications.

Linear elastic fracture mechanics (LEFM), the theoretical foundation of fracture mechanics, has been established primarily for stiff materials. Because it is based on linear elasticity, it fails at capturing the complexity of the fracture behaviors exhibited by synthetic polymers. Since the 1950s, with the pioneering works of Lake, Thomas, Rivlin and Greensmith [73, 133, 114, 45], significant

progress has been made in our understanding. Notably, the non-linear behavior of these materials at large strains significantly modified the theoretical picture proposed by LEFM in the region near the crack tip [84]. Additionally, synthetic polymers being inelastic, the energy balance approach proposed by Griffith for elastic materials had to be revisited to account for energy dissipation [20, 107]. Finally, it is clear the fracture of synthetic polymers is a multi-scale problem: inelasticity isn't limited to a region of negligible size at the crack tip and is controlled by bond scission, molecular friction and the relaxation of polymer chains. While the main difficulties have been identified, the fracture of synthetic polymers remains a complex and poorly understood subject, at the interface of physics, chemistry and mechanical engineering.

An important gap in our understanding is the role played by dissipation in the fatigue of synthetic polymers. While experimental data to characterize fatigue in elastomers is available, there is a need to develop a theoretical framework to understand how the energy balance is affected by dissipation under cyclic loading. Additionally, while it is well accepted that increasing energy dissipation and maintaining elasticity enhances the toughness of synthetic polymers [153], there is no clear consensus on how to define, measure or interpret toughness in these materials. Because fracture toughness is often used as a metric to quantify the resistance to crack growth, guidelines are needed to distinguish what is related to the intrinsic properties of materials from what is an artifact of the testing protocol. Finally, connecting the strain-induced softening and the hysteresis observed in synthetic polymers to the degradation of their molecular network remains difficult. In particular for novel materials that feature both viscous and damage-induced dissipation.

This dissertation addresses these challenges as follows. In chapter 3, I present a continuum theory of fatigue fracture for viscoelastic solids which predicts the crack extension per loading cycle for various loading amplitudes, loading frequencies and viscoelastic parameters. In chapter 4 I carried out finite element simulations for a neo-Hookean solid with Mullins effect to analyze the influence of the sample geometry and material properties on the outcome of pure shear fracture tests. Finally, chapter 5 focuses on modeling deformation and damage in carbon fiber reinforced polymers (CFRPs) with a multi-scale approach. Mathematical notations are specific to each chapter.

Chapter 2

Background

2.1 Structure and mechanics of synthetic polymers

2.1.1 Structure

While there exists a large variety of synthetic polymers, they share an underlying network-like molecular structure. In this thesis, I focus on amorphous polymers with flexible chains above their glass transition temperature. To describe their structure, let me start with a drawing (Fig.(2.1)) relevant to the particular case of an elastomer filled with carbon-black nano-particles. To the naked-eye ($\sim mm$ scale) the material appears homogeneous (Fig.(2.1a)). At the micron-scale (Fig.(2.1b)), we notice carbon-black nano-particles ($\sim 10 - 100 nm$) are aggregated into $\sim 100 nm - 1 \mu m$ clusters (this is revealed by transmission electron microscopy [100]). Fig.(2.1c) focuses on the polymer matrix at a few $100 nm$, revealing a network of entangled and bonded polymer chains.

Note this schematic picture may vary from a polymer to another. First, chains may be branched, their length can vary depending on the degree of polymerization (which can be determined from the molecular weight of the polymer), and they may be more or less bonded to one another. Additionally, fillers may not be present or of a different nature, in which case their characteristic size will also differ (in chapter 5, the composite studied is filled with $\sim 100 \mu m$ -long carbon fibers). What is important to notice is the separation of scales: we may define an elementary volume that is large enough to be statistically representative of the underlying molecular structure of the polymer and yet small enough to be considered a volume element in the sense of continuum

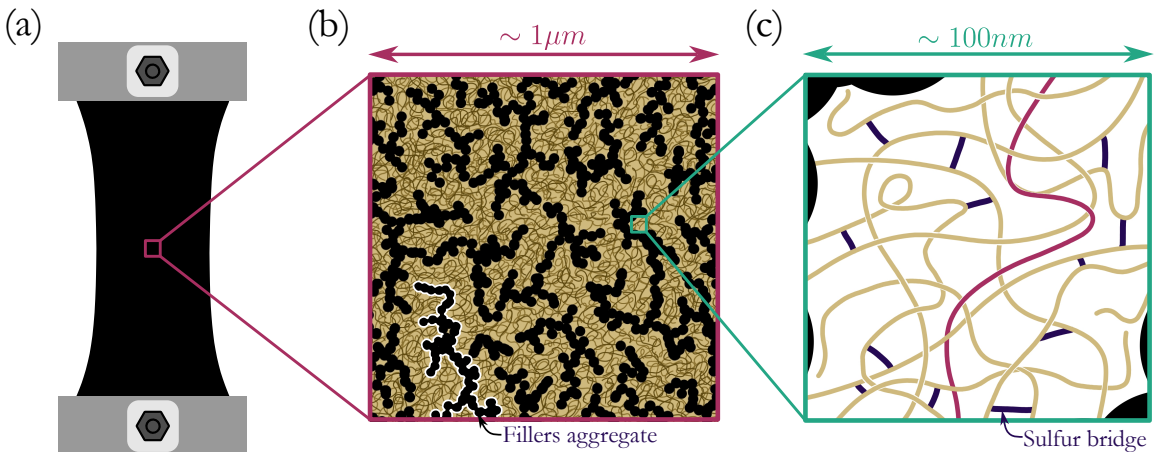


Figure 2.1: (a) Sample scale. (b) Micrometer scale, showing filler aggregates. (c) Molecular network at $\sim 100\text{nm}$ scale, showing entangled and crosslinked polymer chains.

mechanics. Another important aspect that cannot be represented by Fig.(2.1), is the dynamic nature of the molecular network: in synthetic polymers made of flexible chains, the conformation of chains is constantly changing due to thermal fluctuations. For synthetic rubbers, the bonds represented on Fig.(2.1c) are covalent sulfur crosslinks formed at $\sim 150^\circ\text{C}$ through a process called vulcanization. At temperatures corresponding to the operating conditions of rubber components, these bonds are stable and their degradation by temperature or extreme stretching is permanent. In supramolecular polymers, the physical bonds (hydrogen bonds, ionic bonds, ...) are weaker and can be broken or reformed with low energy barriers with order of magnitude similar to thermal fluctuations. In this case both the chain conformation and the bonds between them are dynamic.

2.1.2 Mechanical behavior of synthetic polymers

Observed mechanical behavior

Despite the great diversity of materials represented under the term *synthetic polymers*, we can identify a few common characteristics in their mechanical behavior. Their elastic behavior is compared to a metallic material on Fig.(2.2a). The first observation is of course that synthetic polymers are much softer, with Young's modulus typically within the range $\sim 1\text{kPa} - 10\text{MPa}$ [18]. In comparison, their bulk modulus is much higher ($\sim 1\text{GPa}$), which makes their mechanical

behavior especially sensible to hydrostatic stress. Additionally, as illustrated, these materials fail at much larger strains than metals and are characterized by non-linear elasticity at large strains.

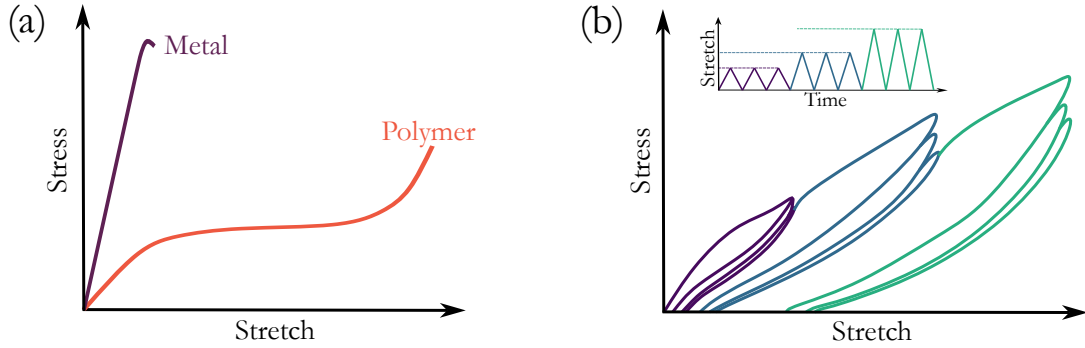


Figure 2.2: (a) Elastic behavior of synthetic polymers. Comparison to metallic materials. (b) Mullins effect in synthetic polymers.

Synthetic polymers also dissipate energy. We may distinguish two principal sources: viscous dissipation, producing a dependence of the stress on the strain rate; and damage, which refers to permanent alterations to the molecular structure that produce a dependence of the stress on the maximum strain.

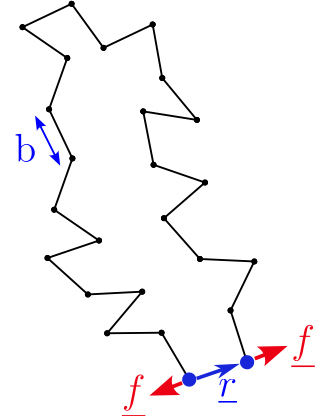
At small strains, the viscoelastic behavior of synthetic polymers can be assessed through dynamic mechanical analysis (DMA), stress relaxation or creep tests. In DMA, a sample is subjected to sinusoidal strain and its stress response is monitored over a range of temperature and frequency. The data reported typically includes the variation of the storage modulus (a measure of the energy stored elastically in the material) and the loss modulus (a measure of the energy dissipated through viscous effects) as functions of the loading frequency or temperature. Rapid changes in storage and loss moduli upon small changes in loading frequency or temperature reveal phase transitions that reflect significant changes at the molecular level. In unfilled polymers, we observe that an increase in loading frequency has similar effects on the viscoelastic response to a decrease in temperature. Specifically, from DMA data it is observed that increasing temperature has the same effect as applying a multiplicative factor $a_T < 1$ to the time axis: this is called the time-temperature

superposition principle [29]. In filled elastomers, relaxation of the filler network also affects the viscoelastic response [64].

The effects of damage in synthetic polymers are generally reflected through a softening that depends on the maximum level of stretch experienced throughout the entire history of deformation. This type of observation in elastomers has been called *Mullins effect* due to the extensive contribution of L. Mullins in this area. This effect is illustrated on Fig.(2.2b), where a sample is stretched in uniaxial tension for a series of cycles with increasing maximum stretch. We observe that the first cycle is associated to a large dissipation, while the subsequent cycles at the same stretch dissipate much less. Upon further increase of the stretch, a new cycle with large dissipation is obtained. Experimental curves showing this type of softening in filled rubbers are available in literature (the table 1 in Diani *et al*'s review [24] is an organized list of the relevant references).

Connection to molecular origin

In polymers made of flexible chains, elasticity is mainly of entropic origin and enthalpic contributions only become relevant under extreme stretch. The concept of *entropic elasticity* can be explained at the scale of a single chain using the ideal chain model. In this model, a chain that is not stretched is represented as *N Kuhn segments* of size b . The Kuhn segments are considered rigid to represent the inability of a few monomers to orient in random directions with respect to each other at scales $<< b$. And these segments are *freely-jointed* to represent the loss of correlation that occurs when assembling monomers over a length $>> b$, which allows sufficiently long chains to be flexible. Therefore, according to this model, drawing an unstretched polymer chain consists in drawing a succession of randomly-oriented Kuhn segments: this can be seen as a random walk in the 3D space with N steps of size b . Now this drawing only represents a particular conformation of the chain, but due to thermal fluctuations, the chain explores all possible



conformations over a sufficiently long time. To understand what is so entropic about polymers elasticity, we need to ask: what is the expected norm of the end-to-end vector $\mathbf{r} = \sum_{i=0}^N \mathbf{b}_i$ of the chain? In the limit of large N , the central limit theorem provides the probability distribution of the end-to-end vector as,

$$P_0(\mathbf{r}) = \left(\frac{3}{2\pi Nb^2}\right)^{3/2} \exp\left(-\frac{3\mathbf{r}^2}{2Nb^2}\right) \quad (2.1)$$

Clearly, coiled configurations are favored, with an average $|\mathbf{r}| = 0$. This result also tells us it is highly unlikely to find a chain in a fully stretch configuration $|\mathbf{r}| = Nb$. This is because coiled macrostates (small end-to-end vectors) may be obtained from a larger number of microstates (individual positions of Kuhn segments). On the contrary, extended macrostates (large end-to-end vectors) may only be constructed from a handful of microstates. All microstates being equally likely, an emerging coiled state is more likely. Now we may express the relation between the probability of \mathbf{r} and the free energy of the macrostate $\psi_c(\mathbf{r})$ using the Boltzmann distribution $P_0(\mathbf{r}) \propto \exp(-\psi_c(\mathbf{r})/kT)$.

We identify,

$$\psi_c(\mathbf{r}) = \frac{3kT}{2Nb^2} \mathbf{r}^2 \quad (2.2)$$

The proportionality with temperature highlights the assumption of the purely entropic contribution at the basis of the ideal chain model: we may write the entropy associated with the macrostate \mathbf{r} as $S = (-3k/2Nb^2)\mathbf{r}^2$. Trying to maintain a chain in a stretched configuration such that $|\mathbf{r}| > 0$ requires the application of a force $\mathbf{f} = \partial\psi_c/\partial\mathbf{r} = -T\partial S/\partial\mathbf{r}$, which is why we talk about *entropic* elasticity. By summing the entropic elasticity of the chains over the network, Treloar [134] provided a satisfactory explanation for the elastic behavior of polymers at moderate stretch. However, this alone cannot explain the stiffening observed at large extensions (Fig.(2.2a)). More complex chain models have been developed that feature a stiffening of individual chains. Notably, the Langevin chain model by Kuhn and Grün [68]. Note this model still attributes the elasticity to a purely entropic contribution, but takes into account the force acting upon the chain. As the material is stretched further, individual chains may reach their contour length, and Kuhn segments can no longer simply align in the direction of stretch: they have to deform: there is an additional enthalpic

cost to stretching. Mao *et al* [90] proposed an extensible Langevin chain model, where they account for the stretching of Kuhn segments.

Viscoelasticity in crosslinked and entangled polymers can be attributed to time dependent molecular processes. For example in unfilled rubbers, entangled chains (Fig.(2.1c)) need time to slither through one another due to non-covalent interactions between the molecules they are made of. Higher temperatures speeds up the slithering while strong intermolecular forces slows it down. In polymers that have dynamic bonds, like the CFRPs studied in chapter 5, the chemical reactions for the formation, disappearance or exchange of bonds are typically associated to energy barriers: at a given temperature, the probability for thermal noise to overcome these barriers sets the characteristic time of these reactions, thereby controlling relaxation or creep at the macroscopic scale.

Damage in polymers refers to irreversible chains or bonds breaking events as well as the irreversible alterations of filler aggregates and filler-chains interfaces. This is a vast area of research, where many molecular theories are proposed to explain observed macroscopic phenomena. Detailed review of these theories isn't directly useful to follow the rest of the work presented in this dissertation. Interested readers will find insightful discussions on the proposed molecular origins of Mullins softening in the review of Diani *et al* [24], the thesis of Y. Merckel [95] and references therein.

2.1.3 Free energy imbalance

In many continuum mechanics theories, the physical admissibility of a constitutive relation is often required to obey the Clausius-Duhem inequality, or the free energy imbalance. Additionally, in fracture mechanics theories, the free energy imbalance is taken as a starting point to arrive at a fracture criterion. In the following, I briefly review the origin of this imbalance for a deforming continuum body.

Let us identify a continuum solid to the region $\Omega \subset \mathbb{R}^3$ it occupies prior to deformation (the reference configuration), with volume \mathcal{V} . We denote $\partial\Omega \subset \mathbb{R}^2$ its external boundary, with surface S

and outward unit normal vector \mathbf{n} . Upon deformation, a material point located at \mathbf{X} in the solid is displaced to the current position at \mathbf{x} according to the mapping $\mathbf{x} = \chi(\mathbf{X}, t)$, where t denotes time. The displacement vector and the deformation gradient tensor are respectively defined as $\mathbf{u} = \mathbf{x} - \mathbf{X}$ and $\mathbf{F} = \partial\mathbf{x}/\partial\mathbf{X}$. For processes in which thermodynamic equilibrium is satisfied at all times, the first law of thermodynamics requires the change in the total energy of the system (internal energy \mathcal{E} + kinetic energy K) to be equal to the sum of the power of external forces on the body P_{ext} and the heat flow Q .

The power of external forces on the solid is comprised of two terms, one associated to surface tractions \mathbf{t} on $\partial\Omega$ and a body force per unit reference volume \mathbf{b} . For the heat flow, we consider a heat flux \mathbf{q} per unit reference surface area together with a heat supply per unit reference volume q so that,

$$P_{ext} = \int_{\partial\Omega} \mathbf{t} \cdot \frac{d\mathbf{u}}{dt} dS + \int_{\partial\Omega} \mathbf{b} \cdot \frac{d\mathbf{u}}{dt} d\mathcal{V} \quad (2.3)$$

$$Q = - \int_{\partial\Omega} \mathbf{q} \cdot \mathbf{n} dS + \int_{\Omega} q d\mathcal{V}. \quad (2.4)$$

However, in mechanical theories, the first principle is rarely expressed as $d\mathcal{E}/dt + dK/dt = P_{ext} + Q$ but rather as $d\mathcal{E}/dt = P_{int} + Q$ by defining the internal power $P_{int} = P_{ext} - dK/dt$. It can be shown that (see proof in [52] chapter 19),

$$P_{int} = \int_{\Omega} \mathbf{P} : \frac{d\mathbf{F}}{dt} d\mathcal{V} = \int_{\Omega} \mathbf{S} : \frac{d\mathbf{E}}{dt} d\mathcal{V} \quad (2.5)$$

with \mathbf{P} the first Piola-Kirchhoff stress tensor (power conjugate to the deformation gradient tensor), or alternatively with \mathbf{S} the second Piola-Kirchhoff tensor (power conjugate to the Green-Lagrangian strain tensor \mathbf{E}). Denoting e the internal energy density per unit reference volume and applying the divergence theorem to the relevant terms, the first principle can thus be expressed under the form,

$$\int_{\Omega} \frac{de}{dt} d\mathcal{V} = \int_{\Omega} \left(\mathbf{S} : \frac{d\mathbf{E}}{dt} - \nabla \cdot \mathbf{q} + q \right) d\mathcal{V}. \quad (2.6)$$

The second principle of thermodynamics expresses an entropy imbalance: the increase of

entropy has to be greater than the entropy flow toward the solid,

$$\frac{d}{dt} \int_{\Omega} \eta dV \geq - \int_{\partial\Omega} \mathbf{J} \cdot \mathbf{n} dS + \int_{\Omega} \mathcal{J} dV \quad (2.7)$$

with η be the entropy density per unit reference volume, \mathbf{J} an entropy flux through the surface and \mathcal{J} a volumetric entropy supply. Note we have $\mathbf{J} = \mathbf{q}/T$ and $\mathcal{J} = q/T$ where the scalar field T is the absolute temperature and replacement in Eq.(2.7) yields the Clausius-Duhem inequality.

For processes where isothermal conditions apply, this inequality can be expressed as a free energy imbalance. For this, we use the expression of the first principle given as Eq.(2.6) to replace the right hand side of Eq.(2.7),

$$\begin{aligned} \int_{\Omega} \left(-\nabla \cdot \left(\frac{\mathbf{q}}{T} \right) + \frac{q}{T} \right) dV &= \int_{\Omega} \left(\frac{1}{T} (-\nabla \cdot \mathbf{q} + q) + \frac{1}{T^2} \mathbf{q} \cdot \nabla T \right) dV \\ &= \int_{\Omega} \frac{1}{T} \left(\frac{de}{dt} - \mathbf{S} : \frac{d\mathbf{E}}{dt} + \frac{1}{T} \mathbf{q} \cdot \nabla T \right) dV \end{aligned} \quad (2.8)$$

Replacing the right hand side of Eq.(2.7) with this expression yields,

$$\int_{\Omega} \left(\mathbf{S} : \frac{d\mathbf{E}}{dt} - \dot{\psi} - \eta \dot{T} - \frac{1}{T} \mathbf{q} \cdot \nabla T \right) dV \geq 0 \quad (2.9)$$

where we introduced the Helmholtz free energy density per unit reference volume $\psi = e - T\eta$. We may localize this equation to obtain the following local free energy imbalance,

$$\mathbf{S} : \frac{d\mathbf{E}}{dt} - \dot{\psi} - \eta \dot{T} - \frac{1}{T} \mathbf{q} \cdot \nabla T = D \geq 0, \quad (2.10)$$

where D is the rate of energy dissipation per unit reference volume, which is equal to the temperature times the rate of entropy production per unit volume, and therefore positive. Additionally, under isothermal conditions, the last two terms vanish and $\mathbf{S} : \frac{d\mathbf{E}}{dt} - \dot{\psi} = D \geq 0$.

This equation is another way to view the second principle, tailored for mechanical theories. It conveys that, in materials there is a part of the internal power that is not accounted for in the change in free energy, which is associated to dissipative processes.

2.1.4 Constitutive modeling of synthetic polymers

To describe the behavior of synthetic polymers in continuum mechanics, one needs to establish a connection between the stresses developed in the body and its motion: a constitutive model.

These models are of course expected to be consistent with basic physics principles. Mathematically it means the relationship is consistent with the free energy imbalance (Eq.(2.10)) and invariant upon changing the frame of reference. But these necessary conditions are insufficient to arrive at useful constitutive models of materials. Enforcing further appropriate restrictions using a combination of physical intuition and experimental observation is a form of art. We can distinguish two main approaches relevant to synthetic polymers: phenomenological models and network models.

Successful phenomenological models produce a satisfactory fit of the stress-strain experimental data, preferably with a limited set of parameters (capturing first order effects makes the model more generalizable and parameters have more chances to be physically interpretable). For example, in chapter 3 I use the standard-linear solid model to describe the viscoelastic behavior of synthetic polymers at low strains; and I use the Ogden-Roxburgh model in chapter 4 to capture the Mullins effect.

Network models, as their name suggests, are attempts to motivate the constitutive model by drawing a connection to the underlying network of entangled and crosslinked chains. In this bottom up approach, the parameters describing the tendency of chains to increase their entropy or the bonds to reorganize dynamically is connected to the elastic modulus and the viscosity observed at the continuum scale. This type of modeling involves three main steps. First, a link between the macroscopic deformation and the stretch acting on individual chains is established. Second, the free energy density defined at the continuum scale is written as a sum of the free energies of individual chains. Finally, the stress is obtained from the free energy density through a constitutive equation that is either assumed or derived from the free energy imbalance (Eq.(2.10)). For example in the eight-chain model proposed by Arruda and Boyce [5], it is assume that when a reference volume of the continuum is transformed by a macroscopic deformation gradient \mathbf{F} , the chains experience a stretch proportional to the average of the macroscopic stretches in the principal directions, $\lambda_{chain} = \sqrt{(\lambda_1^2 + \lambda_2^2 + \lambda_3^2)/3}$. This can be viewed as a network connected from the center to the 8 corners of a cubic reference volume Fig.(2.3a).

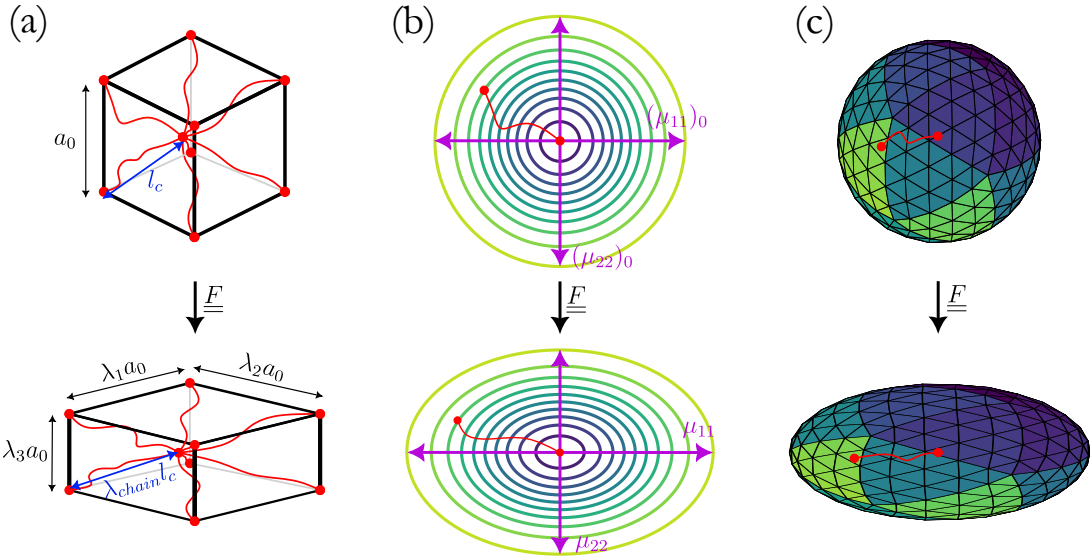


Figure 2.3: (a) Eight-chain model of Arruda and Boyce. (b) Full network model, as in transient network theories, with the Gaussian distribution represented in 2D. (c) Microsphere model, where each facet of the polyhedron represents a direction in the chain configuration space.

The free energy associated from stretching the chains may be computed using a given chain model, for example Diani *et al* use the Langevin chain model ($\psi_c(\lambda_{chain})$) in [23], obtaining the total strain energy density as $W = n\psi_c$, where n is the number of chains per unit reference volume. Assuming hyperelastic behavior, they obtain the Cauchy stress as $\boldsymbol{\sigma} = (\partial W / \partial \mathbf{F}) \mathbf{F}^T - p \mathbf{I}$, with p enforcing incompressibility.

Another approach consists in starting with a Gaussian distribution of chains end-to-end vectors in a network, and computing its evolution by applying the macroscopic deformation \mathbf{F} to each individual chain. This is the approach of transient network theories [130, 136]. The assumption that individual chains are affected by the macroscopic gradient is called the affinity assumption, and is written as $\mathbf{r} = \mathbf{Fr}_0$, where \mathbf{r}_0 is initially distributed according to Eq.(2.1). The chains end-to-end vectors change according to $\dot{\mathbf{r}} = \mathbf{L}\mathbf{r}$ where $\mathbf{L} = \dot{\mathbf{F}}\mathbf{F}^{-1}$ is the velocity gradient, which gives the evolution of $P(\mathbf{r}, t)$,

$$\frac{\partial P}{\partial t}(\mathbf{r}, t) = - \left(\frac{\partial P(\mathbf{r}, t)}{\partial r_i} r_j + P(\mathbf{r}, t) \delta_{ij} \right) L_{ij}. \quad (2.11)$$

The effect on the distribution of applying Eq.(2.11) is illustrated in 2 dimensions on Fig.(2.3b). The free energy stored by each chain is then obtained using Eq.(2.2) for example, and the total elastic energy stored in the network comes as the sum over all chains in the distribution (see Eq.(5.4) in chapter 5). The free energy imbalance, connecting the change in free energy to the power density of internal forces, can then be used to obtain the stress [136]. Note that the effect of bond dynamics can be considered in this type of framework, through Eq.(2.11).

Tracking the full distribution $P(\mathbf{r}, t)$ can be computationally challenging. For example, if this type of model is used in a fracture problem within a finite element solver [122], solving Eq.(2.11) for all elements of the mesh and all time steps is resource intensive. This is why the moments of the distribution are followed instead, through a tensor $\boldsymbol{\mu}$ [136], as illustrated on Fig.(2.3b). Of course such averaging and gain in computational time comes at the cost of a loss of information: if physical phenomena affect $P(\mathbf{r}, t)$ in an anisotropic way, they are wiped out in the averaging operation. This is typically the case for damage: authors have shown that damage in elastomers induces anisotropy [23]. Both the 8-chain model and the reduced transient network theory fall short at describing this phenomenon. The developments of microsphere theories [96, 22, 74] are an effective way to compromise between the ability to account for anisotropy in network models and the computational cost of following the full distribution. The idea is illustrated on Fig.(2.3c), where a discrete number of chain directions are retained across the unit sphere.

2.2 Fracture of synthetic polymers

Fracture mechanics became an engineering discipline following the failure of the Liberty ships steel hull during World War II [4]. Early theoretical developments therefore considered linear elastic behavior, with metals in mind, known today as linear elastic fracture mechanics (LEFM). After the 1960s, models developed to account for non-linear and inelastic behavior, were building upon the knowledge of LEFM. Even though several assumptions at the basis of LEFM are challenged when studying the fracture of synthetic polymers, the relevant literature borrows concepts to LEFM and extends them. So I start with a brief review of the fundamental concepts from this early work.

2.2.1 Basic concepts

How do materials break? Can we establish a fracture criterion?

To answer these questions, it seems relevant to start with an estimation of the cohesive stress σ_c , that is the stress required to separate two atomic layers. Orowan [104] proposed the following scaling,

$$\sigma_c \sim \sqrt{\frac{E\gamma}{d_0}} \quad (2.12)$$

with E the Young modulus, γ the surface energy and d_0 the equilibrium atomic distance.

Experimentally however, industrially relevant materials have a failure stress $\sigma_f \ll \sigma_c$. This is because these materials are not perfect crystals. They contain flaws, and flaws amplify stress in their vicinity. This amplification allows the stress to reach σ_c locally, near the flaw, propagating it, rather than affecting all atomic bonds in the material equally.

The first to calculate this amplification was Inglis [13]. He considered an elliptic crack (with major axis c and minor axis b) in a linear elastic plate, and computed the stress. He showed that, away from the crack, the tensile stress in the plate is similar to the remotely applied stress σ_∞ . However, approaching the crack, the stress increases and reaches the value of $\sigma_{tip} = \sigma_\infty(1 + 2c/b)$ at the crack tip. This is why sharp cracks with $c \gg b$ lead to large stress concentration in their vicinity, such that σ_c may be overcome locally, even under external loads $\sigma_\infty \ll \sigma_c$.

To estimate the stress at failure, let us first rewrite the stress at the crack tip, for a sharp crack, as $\sigma_{tip} \simeq K\sigma_\infty$ with $K = \sqrt{2c/\rho}$ and $\rho = b^2/2c$ the radius of curvature of the elliptic crack. Considering an atomically sharp crack with $\rho \sim d_0$, failure happens for $\sigma_\infty = \sigma_f$ when $\sigma_{tip} = K\sigma_f = \sigma_c$, therefore:

$$\sigma_f \sim \sqrt{\frac{E\gamma}{c}} \quad (2.13)$$

Notice the similarity with Eq.(2.12), where the atomic length scale d_0 has been replaced with the crack size c .

Another way to arrive at an estimation of the failure stress has been provided by Griffith.

He proposed that, when a crack propagates, the total energy of the system is conserved: it is the loss in potential energy $-d\Pi$ following an increment of crack area dA that provides the work of adhesion dW_s required to create new surfaces. Irwin defined the energy release rate as the drop in potential energy per unit cracked area,

$$G = -\frac{d\Pi}{dA} \quad (2.14)$$

where $\Pi = \Psi - W_{ext}$ with Ψ the internal strain energy stored in the material and W_{ext} the work of external forces. With this definition, Griffith energy balance during crack propagation reads,

$$G = \Gamma \quad (2.15)$$

with Γ the fracture toughness: the relevant threshold after which the crack propagates. For the problem of the elliptic crack in the linear elastic plate, we have $\Pi = \Pi_0 - \pi\sigma_\infty^2 c^2 w / 4E$ where w is the thickness of the plate. Since it is the work of adhesion that has to be overcome for crack propagation, we set $\Gamma = dW_s/dA \sim w\gamma$ and we may show that we also arrive at a failure stress $\sigma_f \sim \sqrt{E\gamma/c}$: this is consistent with Eq.(2.13). This estimate of the failures stress is reasonable for brittle materials like glass. However, this is an underestimation in metals because cracks are not atomically sharp and necking is observed close to the crack tip: clearly an inelastic behavior occurs in this region. The elastic theory may still be used successfully on the account of the fact that the region where inelastic effects occur remains small and Eq.(2.13) can still be relevant if γ is reinterpreted as the surface energy together with the plastic work consumed in growing the crack of a unit.

This is obviously a very brief summary of early fracture mechanics and I did not cover the extensions that made the analysis of fracture in metallic structures successful. The important takeaways are (i) materials contain pre-existing defects with characteristic size c , they fail through the propagation of these cracks; and (ii) to arrive at a fracture criterion, there has been two main approaches: stress analysis and energy balance. The goal with stress analysis is to estimate the amplification of stress in the vicinity of a crack: this amplification, written K in the example of Irwin's plate containing an elliptic crack, has been generalized in LEFM into so-called stress

intensity factors (SIF). Their value at failure K_c are reported throughout literature as material properties and fracture criteria are often given as $K \geq K_c$. In the energy balance approach, it is the energy release rate (measured as the drop in the potential energy held by the solid per unit growth of crack area) that becomes the basis for a fracture criterion: authors write $G \geq \Gamma$, where the fracture toughness Γ is reported as a material property. These approaches have been shown to be equivalent for linear elastic materials: K and G are related.

2.2.2 Fundamentals of linear elastic fracture mechanics

In this section I review the two principal methods that have been developed to arrive at fracture criteria for elastic materials: the stress analysis of cracks and the energy balance. The work presented in this thesis to formulate a fracture criterion for synthetic polymers being based on the energy balance approach, I will provide more in-depth background on this aspect. In particular, I review the work of M.E. Gurtin on the thermodynamic basis for the Griffith criterion.

2.2.2.1 Stress analysis of cracks

Irwin and his colleagues developed a framework to describe the elastic fields near the cracks, often referred to as the stress analysis of cracks. They start with the schematic of Fig.(2.4a), considering a stress-free straight crack in an isotropic, homogeneous, linear elastic body under arbitrary loading. The linearity of the problem allowed them to decompose the arbitrary loading into three distinct modes, illustrated on Fig.(2.4b). For any one of the modes (M), they showed that force balance, kinematics and Hooke's law lead to a stress field near the crack tip under the form,

$$\sigma_{ij}^M(l < r < R, \theta) = \frac{K_M}{\sqrt{2\pi r}} f_{ij}^M(\theta) + h.o.t \quad (2.16)$$

where the K_M are the stress intensity factors (SIF). The functions $f_{ij}^M(\theta)$ are universal and describe the angular variation of the fields. Note that, for modes I and II, the components $ij \in \{11, 22, 12\}$ while for mode III $ij \in \{13, 23\}$. Displacement fields are also given under similar form, it is omitted here for conciseness.

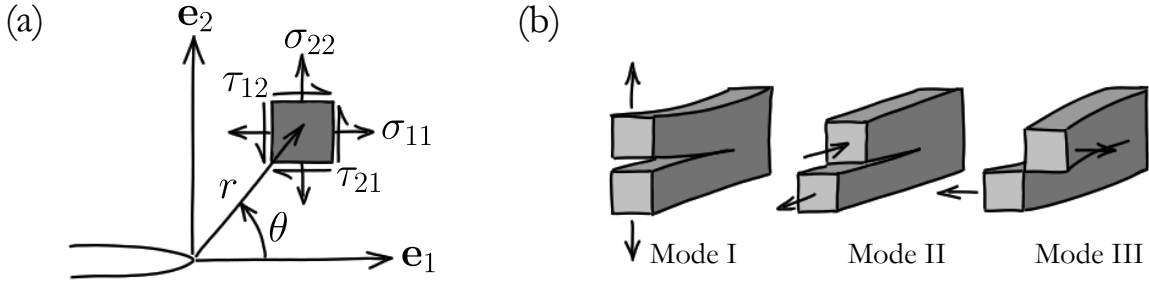


Figure 2.4: (a) Schematic associated to Eq.(2.16). (b) The three modes of fracture.

These fields are valid near the crack only, for $r < R$, with $R \sim \min(c, H)$ the limit of a circular region where the higher order terms are not negligible anymore (H representing the sample size). For $r \gg R$, the state of stress recovers the value it would have in an uncracked body, which is not described by the leading term $\sim 1/\sqrt{r} \rightarrow 0$. Note also that, when $r \rightarrow 0$, the stress defined per Eq.(2.16) becomes infinite: the crack is a singularity. The region around the crack tip where $r \sim l$ is called the process zone (PZ). In the PZ, the stress becomes very large and leads to non-linear and inelastic effects in most materials. In LEFM, it is assumed that the PZ remains small compared to the crack and sample sizes $l \ll \min(c, H)$: this is called the small scale yielding assumption.

The expression of SIF may be calculated analytically for a set of particular geometries and loading conditions (expressions are found in handbooks [129]). They have units of stress $\sqrt{\text{length}}$ and are typically proportional to the magnitude of the applied stress σ_∞ . The relevant length scale varies depending on the problem: for situations where the crack is smaller than the sample dimensions $c \ll H$, we have $K_M \sim \sigma_\infty \sqrt{c}$; while for long cracks $c \gg H$ (for example an edge crack in a long strip of height H), we get $K_M \sim \sigma_\infty \sqrt{H}$. There are in-between situations where $c \sim H$, in which cases the geometric parameters describing the location of the crack with respect to the edges of the sample are involved in the expression of K_M .

2.2.2.2 Thermodynamic justification of Griffith criterion for elastic materials

Griffith's intuition that the energy required to increase the area of a crack by a unit should be compensated by a drop in the potential energy held by the solid is motivated by "the theorem of minimum [potential] energy" [47]. While this principle is equivalent to the first principle of thermodynamics for quasi-static and isothermal processes, Griffith's paper did not include a rigorous proof that this type of fracture criterion is consistent with thermodynamic principles and under what conditions. This work was later done by M.E. Gurtin for elastic solids [50, 51]. In order to rigorously formulate a thermodynamically sound fracture criterion for inelastic solids (chapter 3), I found Gurtin's work very useful. His analysis applies to homogeneous thermo-elastic materials, for which the constitutive equations are assumed to be under the form,

$$\begin{aligned}\psi &= \psi(\mathbf{C}, T, \nabla T) \\ \mathbf{S} &= \mathbf{S}(\mathbf{C}, T, \nabla T) \\ \eta &= \eta(\mathbf{C}, T, \nabla T) \\ \mathbf{q} &= \mathbf{q}(\mathbf{C}, T, \nabla T),\end{aligned}\tag{2.17}$$

where \mathbf{C} is the right Cauchy-Green tensor. Replacing Eqs.(2.17) in the local free-energy imbalance (Eq.(2.10)) yields (see chapter 57 in [52]),

$$\mathbf{S} = 2 \frac{\partial \psi}{\partial \mathbf{C}}(\mathbf{C}, T)\tag{2.18}$$

$$\eta = - \frac{\partial \psi}{\partial T}(\mathbf{C}, T)\tag{2.19}$$

$$\mathbf{q}(\mathbf{C}, T, \nabla T) \cdot \nabla T \leq 0 \quad \forall (\mathbf{C}, T, \nabla T).\tag{2.20}$$

Note that Eq.(2.18) can also be written as,

$$\mathbf{S} : \frac{d\mathbf{E}}{dt} - \dot{\tilde{\psi}} = 0,\tag{2.21}$$

which resembles the local free energy imbalance in isothermal conditions, but where the free energy is replaced by $\tilde{\psi}(\mathbf{C})$ (so that $\dot{\tilde{\psi}} = (\partial \psi / \partial \mathbf{C}) : \dot{\mathbf{C}}$), and interpreted as the strain energy density.

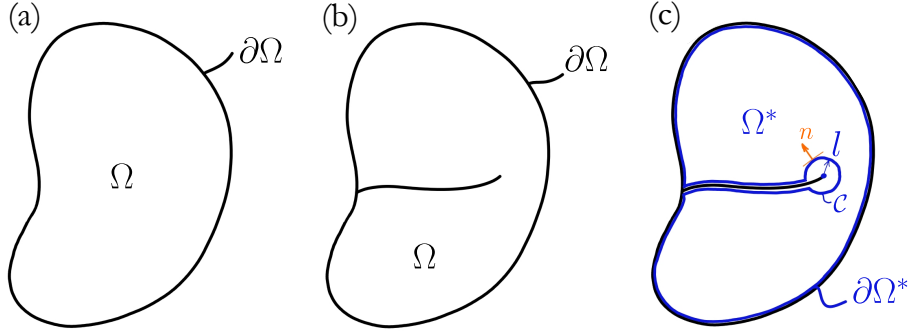


Figure 2.5: (a) Uncracked body. (b) Cracked body. (c) Gurtin’s domain.

Integrating Eq.(2.21) over the area of an uncracked body (Fig.(2.5a)) leads to the trivial result $d/dt(\int_{\Omega} \tilde{\psi} dV) = P_{ext}$: any change in the strain energy held by the solid is provided by the power of external forces. But what happens when the body contains a crack (Fig.(2.5b))? As long as the crack does not propagate, there is no obvious problem: the crack being stress free, no power of external forces is absorbed over its boundary and integrating Eq.(2.21) seems to yield the same trivial result. For a propagating crack however, there should be some amount of energy dissipated at the crack tip to propagate it of a unit area dA per increment dt . Following Griffith, we could assume there exists a value Γ such that we can add the power consumed at the crack tip in the global energy balance as,

$$\frac{d}{dt} \left(\int_{\Omega} \tilde{\psi} dV \right) + \Gamma \frac{dA}{dt} = P_{ext}. \quad (2.22)$$

However, it is unclear how to rigorously obtain Eq.(2.22) from Eq.(2.21) through integration. To avoid the mathematical difficulties of integrating in the presence of a singularity at the crack tip, Gurtin proposed to carve out a small volume around it. On Fig.(2.5c) I have represented this idea in dimension 2 (as in Gurtin’s original publications): a small circular domain \mathcal{C} of size l , connected to the external boundary along the crack faces, is carved out of the 2D domain Ω such that a new

domain $\Omega^* = \Omega - \mathcal{C}$ now excludes the crack tip. Integration of Eq.(2.21) over Ω^* yields,

$$\begin{aligned} \int_{\Omega^*} \dot{\psi} dS &= \int_{\Omega^*} \mathbf{S} : \frac{d\mathbf{E}}{dt} dS \\ \frac{d}{dt} \int_{\Omega^*} \tilde{\psi} dS + \int_{\partial\mathcal{C}} \tilde{\psi} (\mathbf{V} \cdot \mathbf{n}) d\mathcal{L} &= \int_{\partial\Omega^*} \mathbf{t} \cdot \frac{du}{dt} d\mathcal{L} - \int_{\partial\mathcal{C}} \mathbf{t} \cdot \frac{du}{dt} d\mathcal{L} \\ \frac{d}{dt} \int_{\Omega^*} \tilde{\psi} dS &= \int_{\partial\Omega^*} \mathbf{t} \cdot \frac{du}{dt} d\mathcal{L} - \int_{\partial\mathcal{C}} (\tilde{\psi} \mathbf{V} \cdot \mathbf{n} + \mathbf{t} \cdot \frac{du}{dt}) d\mathcal{L} \\ \frac{d}{dc} \int_{\Omega^*} \tilde{\psi} dS &= \int_{\partial\Omega^*} \mathbf{t} \cdot \frac{du}{dc} d\mathcal{L} - \int_{\partial\mathcal{C}} (\tilde{\psi} \frac{\mathbf{V}}{V} \cdot \mathbf{n} + \mathbf{t} \cdot \frac{du}{dc}) d\mathcal{L} \end{aligned} \quad (2.23)$$

where \mathbf{V} is the crack velocity with $V = \|\mathbf{V}\| = dc/dt$ the crack speed and c the crack extension; \mathbf{n} is the outward unit normal to \mathcal{C} and \mathbf{t} is the traction vector on $\partial\Omega^*$. Note I have successively applied the Reynolds transport theorem together with the divergence theorem and divided by V to obtain the last equation. As pointed out by Gurtin in [50], comparing Griffith's definition of the energy release rate $G = -\frac{d}{dc} \int_{\Omega^*} \tilde{\psi} dS + \int_{\partial\Omega^*} \mathbf{t} \cdot \frac{du}{dc} d\mathcal{L}$ with Eq.(2.23) gives,

$$G = \lim_{l \rightarrow 0} \int_{\partial\mathcal{C}} (\tilde{\psi} \frac{\mathbf{V}}{V} \cdot \mathbf{n} + \mathbf{t} \cdot \frac{du}{dc}) d\mathcal{L} \quad (2.24)$$

The first term represents the elastic energy flow through the contour of the carved out region \mathcal{C} due to its motion upon crack propagation. The second term represents the power done by the body on \mathcal{C} . In his publications, Gurtin explains the necessary conditions over the fields ψ , \mathbf{S} and \mathbf{u} such that this limit exists, providing a justification of Griffith's criterion for elastic solids. Additionally, he notes that the integral on the right hand side of Eq.(2.24) reduces to the well known path-independent J-integral for the particular case of straight cracks.

2.2.3 Fracture of synthetic polymers

As explained previously, synthetic polymers feature a large non-linear elastic behavior prior to failure. Near a crack, such materials therefore typically exhibit non-linear behavior that cannot be described within the framework of LEFM. Additionally, dissipation mechanisms are physically different in these materials than in metals and glasses for which LEFM was proven successful. The nature of the bonds between polymer chains as well as the fillers heavily influence dissipation, and should therefore be expected to influence their fracture behavior.

As noted by Long *et al* [86], the fracture of synthetic polymers is a multi-scale problem. In their review, they highlight two physical length scales, useful in discussing the physics of the fracture of a broad range of synthetic polymers. The first one is the non-linear elastic length scale,

$$l_{NL} = \frac{\Gamma}{E}, \quad (2.25)$$

separating non-linear from linear elastic behavior. For materials with elasticity of entropic origin, such as vulcanized natural rubber, $l_{NL} \sim 1-10\text{mm}$ [86]. For metals and glass, this non-linear region would have a size $l_{NL} \sim 0.1-10\text{nm}$, so it cannot exist as plasticity takes over at $l \sim 1\text{nm}-0.1\text{mm}$.

The second length scale has the same definition as the size of the process zone in LEFM, so the same notation is used: l is the size of the region where dissipation occurs. Long *et al* estimate,

$$l \sim \Gamma/W_f \quad (2.26)$$

with W_f the critical energy per unit volume for material failure. This quantity is rather theoretical: it corresponds to the area under the force-displacement curve of a perfect sample under uniaxial tension. *Perfect* here refers to *without defects*, which may be difficult to achieve in practice. For brittle materials $l \sim d_0$ because dissipation only affects a layer of atomic bonds, for metals $l \sim c$ due to plasticity and for polymers it may be related to network parameters $l \sim \sqrt{Nb}$ or to larger structures they may form (*e.g.* strain induced crystal domains).

Depending on how these physical length scales compare to the defect dimension c and the sample size H , these soft materials may be brittle (like hydrogels) or ductile (like elastomers).

Another important difference is the fact that fracture toughness is no longer a material property for synthetic polymers. Part of the potential energy available for crack extension is lost to viscous dissipation and non-localized damage of the polymer network. Similarly to plasticity in metals, these alternative sources of dissipation increase the toughness. They also introduce a dependence of Γ on temperature, crack propagation velocity, loading rate and magnitude. We write the toughness as follows,

$$\Gamma = \Gamma_0 + \Gamma_D \quad (2.27)$$

where the intrinsic fracture toughness Γ_0 is the energy dissipated in the creation of a unit cracked area, while Γ_D is the energy dissipated by any other means. Note that Γ_0 is the energy dissipated in the process zone of size l , while Γ_D may be dissipated all over the sample.

For brittle polymers with $\Gamma \sim \Gamma_0$, the order of magnitude of the intrinsic toughness is $\Gamma_0 \sim 10 - 100 J/m^2$ while the surface energy is $\gamma \sim 1 J/m^2$. This paradox was resolved by Lake and Thomas [73]: they consider that ahead of a crack, polymer chains crossing the crack plane are extended past their contour length. When they break, it is not only the energy of a single bond that is released, but the energy of all the bonds between each Kuhn segment in the chain, and

$$\Gamma_0 = N U_b \Sigma \quad (2.28)$$

with N the number of Kuhn segments, U_b the interaction energy of the bond and Σ the areal density of chains. Lake and Thomas assumed only the layer of chains crossing the fracture plane was broken in the process, and therefore they wrote $\Sigma = n\sqrt{Nb}$, with n the density of chains per unit reference volume and \sqrt{Nb} the height of the reference volume. The assumption that a single layer of chains is stretched is bold, it can however be relaxed as noted by Akagi *et al* [2] by writing the areal density as $\Sigma = nl$. In case network heterogeneity or other larger structures are involved, this definition is more general.

For the dissipative part of the fracture toughness, it is relevant to separate the discussion as follows,

$$\Gamma_D = \Gamma_D^{vis} + \Gamma_D^{dam} \quad (2.29)$$

with Γ_D^{vis} the energy dissipated through viscous effects and Γ_D^{dam} the energy dissipated through non-localized damage.

The first contribution was first observed to depend on crack propagation speed V and temperature T , and to be proportional to Γ_0 , such that $\Gamma_D^{vis} = \Gamma_0 \phi(T, V)$, where $\phi(T, V) > 1$ is an amplification function. Additionally, Gent and others [34, 19, 132, 7] showed that data at different

temperatures, for simple hydrocarbon elastomers, could be collapsed on a single master curve by writing $\Gamma_D^{vis} = \Gamma_0 \phi(a_T V)$, with a_T the Williams-Landel-Ferry (WLF) shift factor. It is observed across a variety of synthetic polymers that $\phi(a_T V) \sim (a_T V)^n$, with $n \sim 0.1 - 1$, as showed by the data of Fig.(2.7b). This type of data encouraged Knauss, Christensen, Schapery, Persson, De Gennes and Hui [65, 17, 107, 20, 56] to propose models based on linear viscoelasticity to explain this dependence. To explain the general idea behind these works let us consider an edge crack in a pure shear strip (Fig.(2.6a)), under static loading (meaning the sample is maintained at a stretch λ).

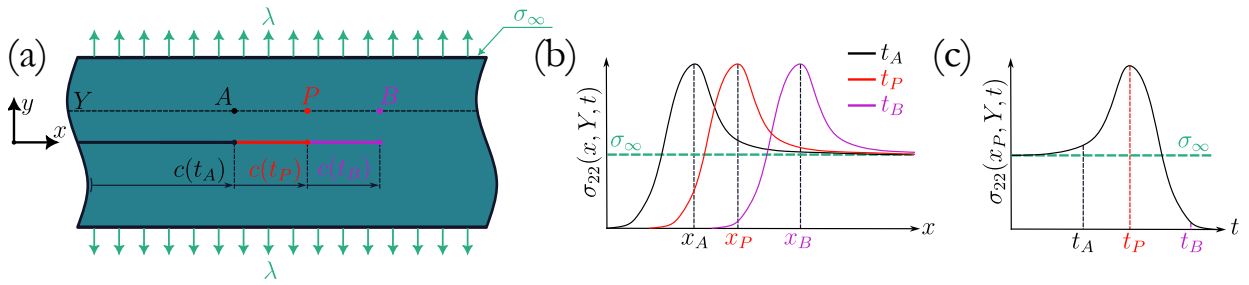


Figure 2.6: (a) Pure shear strip, points A, P, B are taken on a line $y = Y$ at different distances x . (b) Tensile component of stress at points A, P, B for three times t_A, t_P, t_B corresponding to when the crack tip was under each point. (c) Tensile stress at point P , over time.

As discussed above, stress is amplified near the crack, and we may plot the magnitude of the tensile component for all points located on the dotted line (Fig.(2.6a)) at two given times t_A and t_B corresponding to times at which the crack tip is under points A and B , this is provided as Fig.(2.6b). This is because, in the pure shear strip, it has been shown that the stress-strain fields are simply translated by the moving crack, at constant speed V . Therefore the stress across the dotted line has just been translated with the crack tip, between t_A and t_B . Another way to view this is by focusing on a material point P on the dotted line (Fig.(2.6c)), looking at the stress experienced through time, between t_A and t_B : initially the crack tip is far so the stress at P corresponds to the remote stress σ_∞ , then the stress rises as the crack passes underneath P , and

finally it drops to zero at t_B . Through time, a point P experiences a loading-unloading, due to crack propagation, at speed V . The key concept in viscoelastic fracture, is to recognize that the speed at which this loading-unloading happens at P dictates the amount of energy dissipated at this point through viscous effects. The authors of these works started with a simple viscoelastic model of the material, considering a single relaxation time τ . As in DMA, where comparing the rate $1/\tau$ to the loading frequency is key to predict dissipation, here the idea is to compare the crack speed V to the relaxation rate of the material. Indeed, the loading-unloading experienced at point P is happening proportionally to how fast the crack goes from under point A to point B .

As pointed out by Long *et al*, $V\tau$ is not dimensionless and it is necessary to introduce the dissipation length scale l to discuss the material's response to crack propagation [86]. For small propagation speeds, characterized by $V\tau/l \ll 1$, the material responds elastically with long term modulus E_∞ and $\Gamma_D^{visc} \sim 0$. For high propagation speeds, $V\tau/l \gg 1$, the material dissipates energy with $\Gamma_D^{visc} \sim E_0/E_\infty\Gamma_0$, with E_0 the instantaneous modulus.

There is also a spatial effect: the crack tip fields in linear viscoelasticity retain the singularity $\sim 1/\sqrt{r}$, so the points close to the crack tip will experience fast loading upon crack propagation while the ones far from it will experience slow loading. De Gennes showed that the material responds like a hard solid close to the tip $l < r < V\tau$, like a soft solid away from it $r > E_0/E_\infty V\tau$, and like a viscous fluid in between $V\tau < r < E_0/E_\infty V\tau$. By computing the resulting crack opening displacement, he showed the crack tip region looked like a trumpet [20].

2.2.4 Fatigue fracture of synthetic polymers

So far, I have discussed fracture under static loading, meaning the load is applied and maintained. However, in many applications, synthetic polymers experience cyclic loading. The origin of loading fluctuations may be thermal (sealants, pipes), biological (wound dressing, implants during breathing and walking) or functional (rotating tires). It has been observed that many materials, not only synthetic polymers, break under lower loads if they are repeated in a cyclic manner: this is fatigue fracture. As noted by Mars and Fatemi [93], there are two historical approaches to the study

of fatigue fracture in synthetic polymers: one is focused on the analysis of damage nucleation and the formation of cracks, while the other is concerned with the growth of an existing macroscopic crack. Here I focus on the second approach.

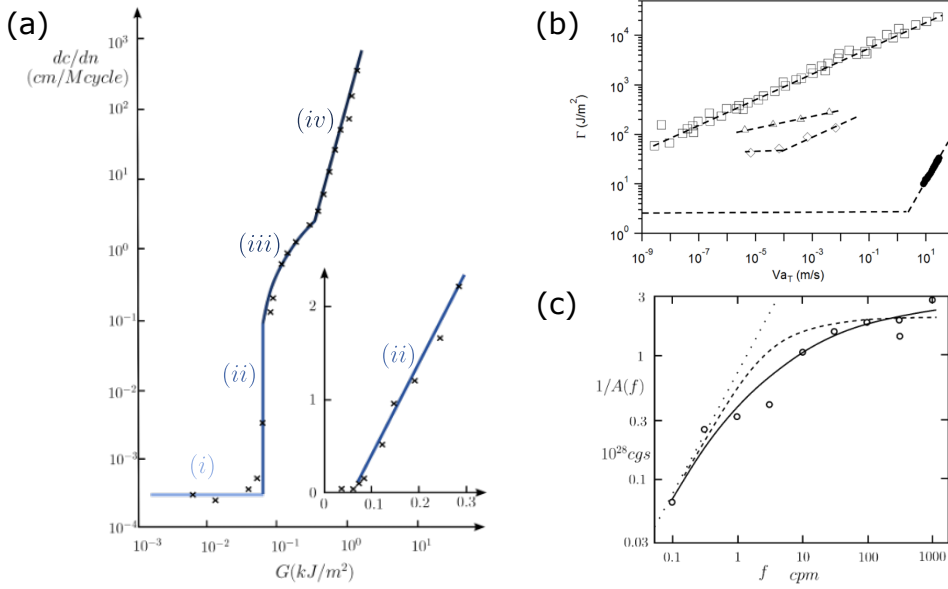


Figure 2.7: (a) Rate of crack propagation per cycle dc/dN at tearing energy G_{max} for SBR. Data gathered by Lake, reproduced from [69]. (b) Fracture energy at reduced propagation velocity for different materials. Reproduced from [18]. (□) SBR, data from Gent *et al* [33]. (◊) Polyurethane rubber, data from Cristiano *et al* [19]. (△) Double network hydrogel, data from Tanaka *et al* [132]. (●) Gelatin gel, data from Baumberger *et al* [7]. (c) Experimental evidence for the dynamic effect: $A(f)$ is the coefficient of Eq.(2.30). Frequency is given in *cpm*, meaning cycles/min and $1/A(f)$ in c.g.s units (centimeter-gram-second system). Reproduced from [71].

Lake, Lindley, Gent, Greensmith and co-authors provided the early works on fatigue fracture of elastomers, in the 1950s-60s [71, 72, 69, 36, 35, 45]. Their analysis was influenced by the parallel developments of the fracture mechanics in metals. Notably, they used the energy budget approach and borrowed the concept of the energy release rate. In their experiments, Lindley, Lake and Gent studied the propagation of macroscopic cracks in the pure shear strip, the tensile and trouser

test pieces under varied loading magnitudes and frequencies [72, 71, 36]. They characterized the crack extension per cycle dc/dN in styrene butadiene rubber (SBR) and natural rubber (NR) as a function of the maximum energy release rate achieved within a loading cycle G_{max} (called tearing energy in their papers). The first key result of their analysis, is the identification of four regimes of fatigue fracture, as depicted on Fig.(2.7a). In the sub-critical regime (i) with $G_{max} \leq \Gamma_0$, the crack barely propagates and the result strongly depends on the experimental detection threshold. As in static experiments, Γ_0 may be estimated from Lake and Thomas theory and is considered a material property. Follows a linear regime (ii), with $dc/dN \propto G_{max}$. Then the crack accelerates with further increase of G_{max} and enters the Paris regime (iii), characterized by a power law of the form,

$$\frac{dc}{dN} = A(f)G_{max}^m \quad (2.30)$$

where m is the Paris exponent ($m \simeq 2$ for unfilled NR and $m \simeq 4$ for unfilled SBR). Finally, they observe a critical regime (iv) with $G_{max} > G_c$, where the crack becomes unstable.

The second main result is called the *dynamic effect*: in the Paris regime, the rate of crack growth for cyclic loading at low frequency is similar to the rate under static loading with the same amplitude. However, for larger loading frequencies, the crack propagates faster, suggesting a dominant dynamic component [71]. Lake and Lindley observed the factor $A(f)$ in Eq.(2.30) depends on the loading frequency f , as depicted on Fig.(2.7c).

Besides the maximum energy release rate achieved within a loading cycle, the minimum has also been shown to be important. We can define the polarization ratio p as,

$$p = \frac{G_{min}}{G_{max}} \quad (2.31)$$

Note that polarization is sometimes defined in terms of minimum and maximum strain in some works. In their experiments [81], Lindley showed that, despite maintaining G_{max} , the rate of crack extension per cycle was reduced by orders of magnitude for higher values of p . This effect was attributed to strain crystallization in NR, but SBR/NR mixes that did not strain-crystallize exhibited qualitatively similar behavior [125, 30].

Lake and Lindley reported on the influence of fillers on the fatigue life of rubbers [72]: they show great improvement for carbon black filled versus unfilled elastomers. Additionally, they observed an increase in fatigue life up to an order of magnitude for finer versus coarser fillers. Recently, Mzabi *et al* refined the analysis by studying the effect of filler content together with crosslinking density [101]: they show the filler content improves fatigue life as long as the crosslinking density is not too high, which would prevent the rearrangement of damaged filler aggregates. With a simple model, they show how fillers help reducing the amount of elastic energy stored close to the crack for the same global energy release rate, thereby improving fatigue life.

Chapter 3

A theory of fatigue fracture in viscoelastic solids

The work presented in this chapter was a collaboration with my advisor Rong Long, Davide Colombo and Julien Caillard, our collaborators de la Manufacture Française des Pneumatiques Michelin. We published it in the Journal of the Mechanics and Physics of Solids [88].

3.1 Introduction

Fatigue is an important failure mode of elastomers in applications where prolonged cyclic loading is present, e.g., tires, sealants and dampeners. Development of elastomers with enhanced resistance to fatigue failure can increase their service life and thus reduce waste. For instance, the resistance of filled rubber to cyclic crack growth is known to play a central role in the fatigue induced separation of two-ply rubber-cord laminates [31, 70]. This property is also suspected to play a central role in fatigue wear of rubber where pre-existing defects grow under repeated loading until wear particles with diameters $\sim 1-10\mu\text{m}$ get dispersed into the environment [98, 54, 62]. Mitigation of this ecological impact requires improvement in the wear resistance of rubber. A fundamental mechanism that underlies fatigue failure or wear of elastomers is the intermittent propagation of sharp cracks under cyclic loading. This process, referred to as *fatigue fracture* hereafter, is the central problem considered in this work.

Numerous experimental studies have been devoted to the study of crack propagation in elastomers under cyclic loading [71, 35, 94]. In these experiments, a precut specimen prepared according to a certain fracture test geometry such as the pure shear or the single edge notch,

among others [18, 85], is subjected to cyclic loading with a fixed amplitude. The consequent crack propagation is measured in terms of the crack length c as a function of cycle number N . It is typically observed that the crack extension per cycle, dc/dN , starts from a relatively high value at the beginning of an experiment and gradually decreases to a steady value as N increases [35]. The steady value of dc/dN depends on the amplitude of cyclic loading which is quantified by the energy release rate G_{max} at the peak of each loading cycle (the minimum value G_{min} being often set to zero). The plot of dc/dN versus G_{max} is often reported to characterize an elastomer's resistance to crack propagation under cyclic loading. For most elastomers, the dc/dN versus G_{max} curve consists of several distinct stages. First, when G_{max} is below a value known as the fatigue threshold, dc/dN is undetectable experimentally and hence is taken as zero. Second, above the fatigue threshold, dc/dN first increases linearly with G_{max} , followed by the Paris regime featuring a power law relation $dc/dN \sim (G_{max})^m$ where m is a dimensionless constant. Finally, catastrophic growth is observed if G_{max} is beyond a critical value G_c [69]. Recent experiments on the fatigue fracture of hydrogels have revealed similar stages of the dc/dN versus G_{max} curve [6, 80, 79].

Despite extensive experimental data on the fatigue fracture of elastomers, mechanistic understandings on this intricate problem are relatively limited. Since fatigue experiments can be time-consuming due to the large number of loading cycles involved, theoretical insights relating the material properties of elastomers to the fatigue fracture process are highly valuable. Here we focus on elucidating the continuum mechanics of fatigue fracture in elastomers. While elastomers have the ability to undergo reversible large deformation, most technologically relevant elastomers do exhibit various inelastic behaviors. For example, natural rubbers, when highly stretched, can experience strain-induced crystallization [59, 32]. Filled rubbers are subjected to the Mullins softening during a loading cycle [24]. Unfilled synthetic rubbers with cross-linked networks (e.g., styrene-butadiene rubber) do not crystallize [24] and do not show significant Mullins effect either [24, 25]. The main inelastic behavior for this class of elastomers (i.e., unfilled and non-crystallizing) is viscoelasticity. All of these inelastic behaviors can affect crack propagation [148, 150, 110, 57]. In this work, we limit our scope to unfilled non-crystallizing rubbers and present a theory to explain how

viscoelasticity affects fatigue fracture.

To place this work into perspective, we briefly review the existing theories of viscoelastic fracture [65, 119, 56, 20, 46, 107]. These theories are motivated by the experimental observation that the fracture toughness Γ of viscoelastic elastomers is dependent on both the crack speed V and the temperature T . Interestingly, the functions $\Gamma(V)$ measured under different temperatures can be collapsed onto a master curve by applying the time-temperature shift factors for bulk viscoelasticity [34, 65]. To explain this phenomenon, theoretical models are established to determine the crack speed V of steady-state crack propagation in an infinitely large linear viscoelastic solid. In these models, material in the far field is assumed to be fully relaxed and thus behave as a linear elastic solid. Therefore, the far field loading can be represented by a given stress intensity factor K , or equivalently an energy release rate G (i.e., static loading). Near the crack tip, viscoelasticity prevails while the stress field follows the K -field solution in Linear Elastic Fracture Mechanics (LEFM) with the amplitude prescribed by K or G . There are two approaches to account for the effects of viscoelasticity near the crack tip. In the first approach [65, 119, 56, 46], a cohesive zone is introduced to model the local fracture process at the crack tip. Bridging the cohesive zone and the elastic far field (i.e., the K -field) is the viscoelastic material surrounding the crack tip. The crack speed V is determined by solving the crack opening displacement in the cohesive zone and letting it satisfy a local fracture criterion. In the second approach [20, 118, 107], the focus is on calculating the viscoelastic dissipation due to the loading and unloading process in material points as the crack tip passes by. For example, by proposing the *viscoelastic trumpet* picture, de Gennes qualitatively explains the spatially dependent strain rates experienced by material points upon the propagation of a crack in their vicinity. More detailed discussions of these two approaches and their comparison can be found in a recent work [57]. In short, these theories revealed the importance of two timescales, one related to the viscoelastic relaxation and the other set by the crack speed V . Interplay between these two time scales governs the rate dependence of steady-state crack propagation in viscoelastic materials.

Cyclic loading introduces an additional time scale to the theoretical picture described above.

Indeed, Lake and Lindley [71] observed that in unfilled styrene-butadiene rubber, the rate of crack growth under cyclic loading is faster than that under static loading with the same amplitude if the frequency of cyclic loading is high. This is known as the *dynamic effect*. More broadly, the history-dependent nature of viscoelasticity implies that not only the loading frequency, but the detailed wave form of the loading cycles may affect cyclic crack growth [82]. No theoretical models had been proposed to explain the dynamic effect of cyclic crack growth in viscoelastic materials until recently. Guo *et al.* [49] extended the scaling theory of de Gennes [20] from static crack growth to cyclic crack growth, and established a governing equation for the varying crack speed within a loading cycle. Numerical solutions based on the governing equation are qualitatively consistent with the experimentally observed dynamic effect in cyclic crack growth. However, this is still a scaling theory in nature since it neglects the multi-axial stress state around the crack tip and focuses on a specific fracture geometry, i.e., pure shear [18]. Additionally, numerical solutions can only be obtained under the assumption of slow crack propagation and slow loading. The predictive potential of this theory can therefore be extended by considering three points: i) multi-axial stress state, ii) more general fracture geometry, and iii) new numerical methods to solve for the crack speed.

In this work we address Point i) in Section 3.2 and 3.3 where we reformulate the energy release rate starting from the principles of thermodynamics. Regarding Point ii), we separate the generality of our formulation from the need to characterize the stress field for specific geometries. Indeed, in Section 3.4 we specify the detailed assumptions required to derive the governing equation of crack extension and discuss extension to fracture geometries other than pure shear. Regarding Point iii), we develop novel numerical methods to solve for crack speed as detailed in Section 3.5. Finally, we compare the results given by our theory to finite element simulations in Section 3.6 and demonstrate significant improvement in computational time. We explore the influence of material parameters and loading conditions on the relationship between dc/dN and G_{max} . We also demonstrate that linear viscoelasticity with a single relaxation time qualitatively explains the dynamic effect observed by Lake and Lindley [71], but it is not enough to exhibit the Paris regime.

3.2 Energy Balance and Fracture Criterion

Let us consider a continuum solid as shown in Fig.(3.1a). Initially this solid is not subjected to any external loading or any internal stresses. This state serves as the starting point of deformation, and will be called the reference configuration hereafter. In the reference configuration, the solid is represented by $\Omega \subset \mathbb{R}^3$ with volume \mathcal{V} . Its external boundary is denoted by $\partial\Omega \subset \mathbb{R}^2$ with surface area S and outward unit normal vector \mathbf{n} (see Fig.(3.1a)). Within Ω there is a crack consisting of two overlapping, traction-free surfaces that share a common boundary, i.e., the crack front. For generality, we assume that the crack surfaces can be either fully enclosed in Ω or have intersections with its external boundary $\partial\Omega$ (i.e., an edge crack). In the latter case, the intersection between the crack surfaces and $\partial\Omega$ should be excluded from the crack front.

Upon deformation, a material point located at \mathbf{X} in the solid is displaced to the current position at \mathbf{x} according to the mapping $\mathbf{x} = \chi(\mathbf{X}, t)$, where t denotes time. The displacement vector and the deformation gradient tensor are respectively defined as $\mathbf{u} = \mathbf{x} - \mathbf{X}$ and $\mathbf{F} = \partial\mathbf{x}/\partial\mathbf{X}$. Crack propagation results in expansion of the crack surfaces and motion of the crack front. However, deformation can also displace the crack front even in the absence of crack propagation. To decouple the effects of deformation and crack propagation, we map the deformed crack at time t back to the reference configuration, and define the corresponding crack surface area as A and the crack front as \mathcal{C} . Therefore, crack propagation is reflected by the time evolution of \mathcal{C} .

3.2.1 Thermodynamics

Here we discuss the thermodynamics of crack propagation to facilitate a formal definition of the fracture criterion for inelastic materials. We restrain ourselves to quasi-static processes in which thermodynamic equilibrium is satisfied at all times and inertial effects are negligible. Under cyclic loading, heat generated by mechanical dissipation may build up and cause an increase in temperature [48], which could further affect mechanical properties of the solid. For simplicity, we assume heat transfer occurs at a much faster timescale than deformation and crack propagation

such that the isothermal condition applies, i.e., the temperature is constant both spatially and temporally.

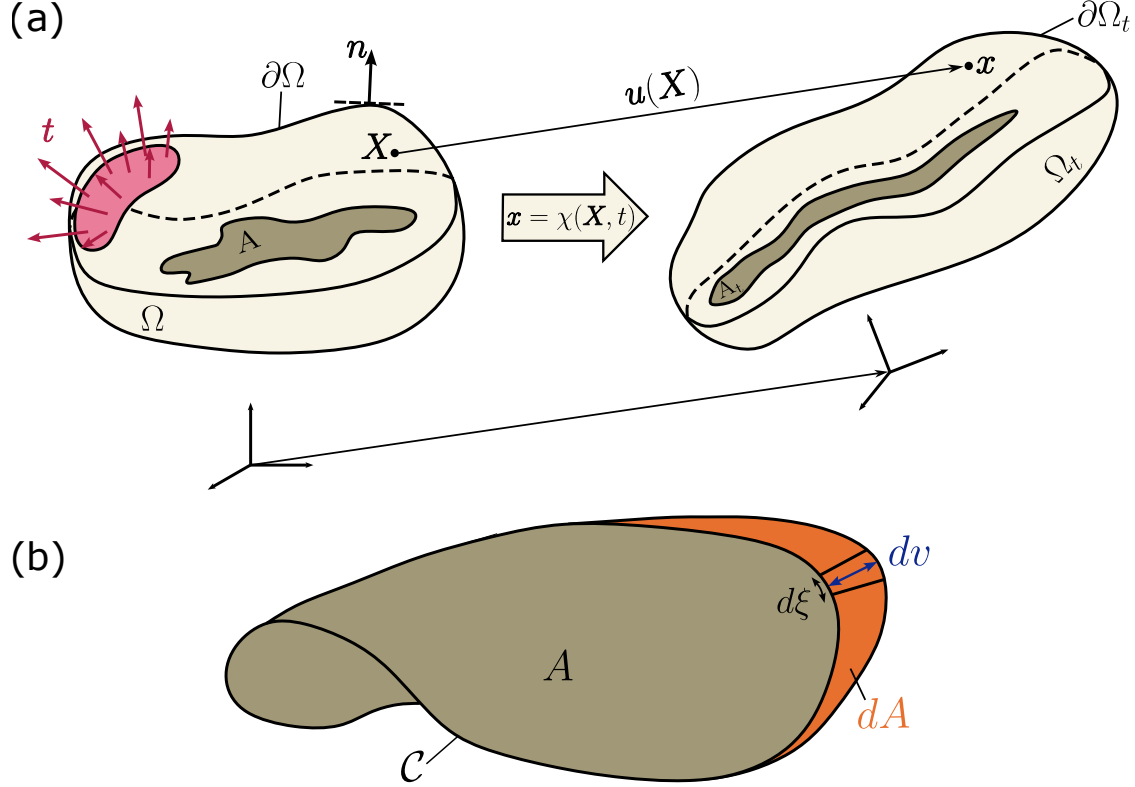


Figure 3.1: (a) Kinematics of a cracked continuum body. We denote Ω the continuum in the reference configuration and Ω_t at time t in the deformed configuration. The same logic is applied to the crack areas A and A_t . (b) Crack surface A delimited by crack front \mathcal{C} . The orange shaded area corresponds to the extension dA happening over the time interval dt .

In the continuum mechanics literature, the first and second laws of thermodynamics are usually combined to yield an equation in terms of the Helmholtz free energy, known as the free energy imbalance [52]. Under the isothermal condition, the local form of free energy imbalance at a material point is [55]:

$$\frac{d\psi}{dt} + D = \mathbf{S} : \frac{d\mathbf{E}}{dt}, \quad (3.1)$$

where ψ is the Helmholtz free energy per unit reference volume, D is the rate of energy dissipation

per unit reference volume, and \mathbf{S} is the second Piola-Kirchhoff stress conjugate to the Green-Lagrangian strain \mathbf{E} . Note that \mathbf{E} is related to the deformation gradient \mathbf{F} through $\mathbf{E} = (\mathbf{F}^T \mathbf{F} - \mathbf{I})/2$ where \mathbf{I} is the identity tensor. The dissipation rate D is equal to the temperature times the rate of entropy production per unit reference volume, and therefore must be non-negative [55]. The term $\mathbf{S} : d\mathbf{E}/dt$ represents the stress power per unit reference volume. Alternatively, it can be replaced by $\mathbf{P} : d\mathbf{F}/dt$ where \mathbf{P} is the first Piola-Kirchhoff stress tensor [55]. The global form of free energy imbalance can be obtained by integrating Eq.(3.1) throughout the solid [55, 52].

In case of crack propagation, additional free energy is consumed by fracture processes occurring at the crack front. To account for this effect, Qi *et al* [110] introduced Γ_0 as the Helmholtz free energy required to advance the crack by a unit area measured in the reference configuration, and included the rate of free energy consumption due to crack propagation as $\Gamma_0 dA/dt$ in the global free energy imbalance. However, this is based on an implicit assumption that Γ_0 is constant along the crack front. This assumption can be relaxed by allowing Γ_0 to vary along the crack front \mathcal{C} , i.e., Γ_0 can be a function of the curvilinear abscissa ξ of \mathcal{C} . Physically, this is motivated by the possibility that fracture processes may depend on local conditions at the crack front (e.g., mixed-mode condition or crack propagation speed). To define the incremental crack area associated with $\Gamma_0(\xi)$, we consider a segment $d\xi$ of the crack front at time t , and denote dv as the distance connecting the mid-point of $d\xi$ to the crack front at $t + dt$ along the normal direction of $d\xi$ (see Fig.(3.1b)). The increase in crack area locally at the segment $d\xi$ is therefore $dvd\xi$, and the corresponding free energy consumption due to crack propagation is given by the integral of $\Gamma_0(\xi)dv/d\xi$ throughout the crack front \mathcal{C} .

Following the same derivations as in Qi *et al* [110] and incorporating $\Gamma_0(\xi)$, we obtain the equation below for the global free energy imbalance:

$$\frac{d}{dt} \int_{\Omega} \psi d\mathcal{V} + \int_{\Omega} D d\mathcal{V} = \int_{\partial\Omega} \mathbf{t} \cdot \frac{d\mathbf{u}}{dt} dS - \int_{\mathcal{C}} \Gamma_0(\xi) \frac{dv}{dt} d\xi, \quad (3.2)$$

where \mathbf{t} is the surface traction vector and \mathbf{u} is the displacement vector. Note that we have assumed that the solid is not subjected to any body forces and that the crack surfaces are traction free.

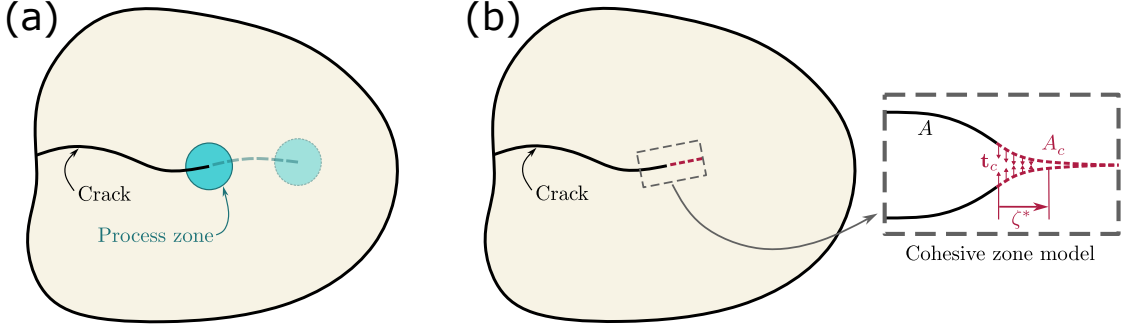


Figure 3.2: (a) Illustration of a process zone around the moving crack tip. (b) Mechanistic representation of the process zone by a cohesive zone model.

The crack front is assumed to be infinitely sharp and may be subjected to a singularity in the local stress field. Such singularity has been theoretically characterized for elastic materials, either linear [146] or nonlinear [84]. However, the singularity leads to a question on whether the volumetric integrals in Eq.(3.2) are well defined. This question has been addressed in Gurtin [51] by carving out a circular area centered at the tip of a two-dimensional (2D) crack from the integration domain (see Fig.(3.2a)) and letting its radius approach zero. This treatment allows one to circumvent the crack tip singularity when integrating the free energy density ψ , and can be readily extended to the geometry shown in Fig.(3.1) where the crack front is represented by a three-dimensional (3D) curve \mathcal{C} . Here one can carve out a tubular volume centered at \mathcal{C} from Ω and let the radius of this tubular volume approach zero.

We emphasize that Gurtin's thermodynamic framework [51] was based on the assumption of elasticity. In this case, $D = 0$ and ψ becomes the elastic strain energy density. As the circular area carved out from the crack tip is shrunk to zero, the total elastic strain energy (i.e., integral of ψ throughout the solid) does possess a finite limit [67]. Indeed, Gurtin [50] obtained an energy balance equation for crack propagation in elastic materials that is essentially the same as Eq.(3.2) (with $D = 0$). For a propagating crack, the circular area translates with the crack tip (Fig.(3.2a)). By examining the energy exchange through the circular area's moving boundary, Gurtin [50] recovered the J-integral for evaluating the energy release rate of a crack in elastic solids [112]. However, if the

material in Ω is inelastic (i.e., $D \neq 0$), the volumetric integrals in Eq.(3.2) are not guaranteed to possess finite limits when the circular area is shrunk to zero. Indeed, in the literature of viscoelastic fracture [57], it has long been recognized that the total dissipation $\int_{\Omega} D dV$ is unbounded unless a cut-off length is introduced to avoid the stress singularity at the crack tip.

Physically, the crack front singularity must be regularized by additional damage mechanisms beyond the bulk constitutive behavior, which results in a finite process zone surrounding the crack tip. This process zone is the physical manifestation of the area carved out around the crack tip in Gurin's thermodynamic framework [50] (Fig.(3.2a)). In elastic materials, there exists a set of universally structured stress and strain fields (e.g., the K -fields in LEFM [146]) bridging the process zone and the external loading. Consequently, the size of process zone does not affect the global energy equation and thus can be infinitely small. For inelastic materials, the process zone size (e.g., the cut-off length in [20, 107]) may affect the extent of bulk dissipation and should be specified in the global energy equation. This implies that for inelastic materials, the assumption of crack tip singularity is not necessarily compatible with Eq.(3.2); instead, it must be regularized by introducing a process zone to the crack tip.

To capture the process zone, we follow Knauss [65] and Schapery [119] and assume the crack front is subjected to a given cohesive zone model [58]. Specifically, the cohesive zone model neglects the volume of the process zone and simplifies it to two attracting surfaces along the fracture plane (Fig.(3.2b)). This allows us to formally separate the effects of bulk material behavior from the process zone. The cohesive zone removes the crack front singularity and makes the volumetric integrals in Eq.(3.2) finite. Given that Ω is a fixed domain in the reference configuration, we can switch the time derivative and the volumetric integral in $d(\int_{\Omega} \psi dV)/dt$ and then apply Eq.(3.1), which yields

$$\int_{\Omega} \mathbf{S} : \frac{d\mathbf{E}}{dt} dV = \int_{\partial\Omega} \mathbf{t} \cdot \frac{du}{dt} dS - \int_C \Gamma_0(\xi) \frac{dv}{dt} d\xi. \quad (3.3)$$

This equation is valid for any solid, elastic or inelastic, that contains an actively propagating crack, as long as the quasi-static condition is satisfied and the crack front singularity is regularized by a

cohesive zone.

3.2.2 Fracture criterion

In this section, we use Eq.(5.5) to derive a fracture criterion for crack growth. First, we introduce a simplification to Eq.(5.5) by assuming Γ_0 to be a material constant. This assumption is commonly adopted in the viscoelastic fracture theories for steady-state crack growth under static loading [57]. It implies that damage in the fracture process zone is an inherent material property. For example, Lake and Thomas [73] proposed that Γ_0 for rubbery networks is governed by the process to fully stretch and break polymer chains ahead of the crack, and established a relation between Γ_0 and the density and length of chains as well as the energy required for bond scission. This physical picture has been challenged in a recent experimental work where bond scission can be detected using mechanophores [123]. Theories treating bond scission as a thermally activated kinetic process have also been developed [14, 141, 137]. Such theories can lead to dependence of Γ_0 on the crack propagation velocity. Given that the focus of this work is on the effect of bulk viscoelasticity on cyclic crack growth, we have adopted the simplistic view that Γ_0 is a constant, which allows us to reduce Eq.(5.5) to:

$$\int_{\Omega} \mathbf{S} : \frac{d\mathbf{E}}{dt} dV = \int_{\partial\Omega} \mathbf{t} \cdot \frac{d\mathbf{u}}{dt} dS - \Gamma_0 \frac{dA}{dt}. \quad (3.4)$$

Second, we further assume that the crack surfaces are planar and the crack front \mathcal{C} advances in a self-similar manner. This assumption allows us to represent the effect of crack propagation solely through the crack area $A(t)$ without accounting for the detailed geometry of \mathcal{C} . Note that certain constraints on the external loading may be required to maintain self-similar growth of the crack front (e.g., axisymmetric loading for a penny-shaped crack). Nevertheless, based on this assumption we can write the displacement and strain of a material point as functions of its reference coordinates \mathbf{X} , the crack area $A(t)$, and the time t , i.e., $\mathbf{u}(\mathbf{X}, A, t)$ and $\mathbf{E}(\mathbf{X}, A, t)$. The additional dependence on time is included to reflect the changes not caused by crack propagation. The displacement field

and deformation gradient obey the following chain rule:

$$\frac{d\bullet}{dt} = \frac{\partial\bullet}{\partial t}\Big|_A + \frac{\partial\bullet}{\partial A}\dot{A}, \quad (3.5)$$

where we wrote $\dot{A} = dA/dt$ for conciseness.

We can now use the chain rule in Eq.(3.5) to rewrite Eq.(3.4) as

$$\begin{aligned} & \left(\int_{\Omega} \mathbf{S} : \frac{\partial \mathbf{E}}{\partial t} \Big|_A d\mathcal{V} - \int_{\partial\Omega} \mathbf{t} \cdot \frac{\partial \mathbf{u}}{\partial t} \Big|_A dS \right) \\ & + \left(\int_{\Omega} \mathbf{S} : \frac{\partial \mathbf{E}}{\partial A} d\mathcal{V} - \int_{\partial\Omega} \mathbf{t} \cdot \frac{\partial \mathbf{u}}{\partial A} dS + \Gamma_0 \right) \dot{A} = 0. \end{aligned} \quad (3.6)$$

The first term of this equation represents the difference between the powers of internal stress work and external work in the absence of crack propagation, which should vanish for quasi-static and isothermal deformation [55]. This implies that the second term in Eq.(3.6) should also be zero. For an actively propagating crack, $\dot{A} > 0$ and therefore:

$$\Gamma_0 = \int_{\partial\Omega} \mathbf{t} \cdot \frac{\partial \mathbf{u}}{\partial A} dS - \int_{\Omega} \mathbf{S} : \frac{\partial \mathbf{E}}{\partial A} d\mathcal{V}. \quad (3.7)$$

The right hand side of Eq.(3.7) represents the mechanical energy available to drive crack growth by a unit area and thus is defined as the intrinsic energy release rate G_0 . Note that Eq.(3.7), or $G_0 = \Gamma_0$, is satisfied only for a propagating crack ($\dot{A} > 0$). If $G_0 < \Gamma_0$, no crack propagation should occur. Therefore, we impose the following fracture criterion:

$$\begin{cases} \dot{A} = 0 & \text{if } G_0 < \Gamma_0 \\ \dot{A} > 0 & \text{if } G_0 = \Gamma_0 \end{cases} \quad \text{with } G_0 = \int_{\partial\Omega} \mathbf{t} \cdot \frac{\partial \mathbf{u}}{\partial A} dS - \int_{\Omega} \mathbf{S} : \frac{\partial \mathbf{E}}{\partial A} d\mathcal{V}. \quad (3.8)$$

As discussed in the previous section, damage in the fracture process zone is mechanistically represented by a cohesive zone model. The cohesive zone model prescribes a given distribution of cohesive traction across the fracture plane [65, 119] or a relation between the cohesive traction and the corresponding separation [58]. In Appendix A, we show that Γ_0 is given by the integral of the cohesive traction with respect to the separation.

3.2.3 Energy release rates

In elastic fracture mechanics, the energy release rate G is defined as the change in potential energy per unit area of crack growth:

$$G = \int_{\partial\Omega} \mathbf{t} \cdot \frac{\partial \mathbf{u}}{\partial A} dS - \frac{\partial}{\partial A} \int_{\Omega} \psi dV, \quad (3.9)$$

where ψ is the elastic strain energy density. This definition can be extended to inelastic material by interpreting ψ as the Helmholtz free energy density [110]. This definition of G does not match that of G_0 in Eq.(4.9). To illustrate their difference, we follow the assumption in the previous section and write the field of ψ as a function of crack area A and time t , i.e., $\psi(\mathbf{X}, A, t)$. The difference $G - G_0$ can therefore be written as

$$G - G_0 = -\frac{\partial}{\partial A} \int_{\Omega} \psi dV + \int_{\Omega} \mathbf{S} : \frac{\partial \mathbf{E}}{\partial A} dV = \int_{\Omega} \left(\mathbf{S} : \frac{\partial \mathbf{E}}{\partial A} - \frac{\partial \psi}{\partial A} \right) dV. \quad (3.10)$$

Note that we switched the partial derive $\partial/\partial A$ and the volumetric integral in $\partial(\int_{\Omega} \psi dV)/\partial A$ because Ω is a fixed domain in the reference configuration and ψ is finite throughout Ω . Eq.(3.10) implies that the difference between G and G_0 is attributed to the energy dissipation associated with crack propagation. To illustrate this point, we rewrite Eq.(3.1) in the following form:

$$\left(\mathbf{S} : \frac{\partial \mathbf{E}}{\partial t} \Big|_A - \frac{\partial \psi}{\partial t} \Big|_A \right) + \left(\mathbf{S} : \frac{\partial \mathbf{E}}{\partial A} - \frac{\partial \psi}{\partial A} \right) \dot{A} = D. \quad (3.11)$$

This equation shows that the dissipation power density D can be decomposed into two parts, one of which is caused by crack propagation and the other accounts for any additional dissipation (e.g., variation in the external loading). The difference $G - G_0$ is only associated with the part caused by crack propagation and will be referred to as G_d^s hereafter.

For steady-state crack growth under static loading [57], material points far from the crack front are under a constant stress and strain state and thus do not entail any dissipation. Only the propagating crack causes the material to dissipate energy. Specifically, it is the concentration of stress at the crack tip together with a moving crack tip that causes the material points on its way to experience a loading-unloading process and dissipate energy in this process. As a result, the

first term on the left hand side of Eq.(3.11) vanishes and hence $G_d^s \dot{A} = \int_{\Omega} D dV$, implying that the differential $G_d^s = G - G_0$ is directly associated with dissipation power density D . This feature has been leveraged as the starting point in several viscoelastic fracture theories for steady-state crack growth under static loading [20, 107, 118].

Under cyclic loading, however, even if the crack is not propagating, dissipation can still occur in a viscoelastic material. In this case, $G_d^s = G - G_0$ does not account for all the dissipation, but only a part of it. Delineating the part of dissipation solely due to crack propagation from D can be difficult. Instead, as demonstrated in Guo et al. [49], we can utilize Eq.(4.9) to solve for the rate of crack propagation under cyclic loading, but this requires us to determine the fields of stress \mathbf{S} and strain \mathbf{E} , which will be discussed in the next section.

3.3 Material Behavior

In order to proceed with our theory, we now impose the assumption of linear viscoelasticity for the constitutive behavior. As mentioned in the introduction, viscoelasticity is the dominant inelastic behavior for unfilled non-crystallizing rubbers. A key advantage of assuming *linear* viscoelasticity is the ability to utilize the stress fields obtained in linear elastic fracture mechanics (LEFM). Indeed an extensive collection of stress field solutions is available in LEFM [129]. These stress field solutions can be transferred to linear viscoelastic solids by leveraging the correspondence principle. Specifically, Graham [41] proposed an extension of the correspondence principle to problems with time-dependent boundaries. This extension allows the application of stress fields in LEFM to crack propagation problems in linear viscoelastic solids [119, 57].

We emphasize that linear viscoelasticity may not be adequate for describing the material behavior in the region adjacent to the crack front where nonlinear effects associated with large deformation may prevail, which is highlighted by Knauss [65] as the major limitation of the current viscoelastic fracture theories. In this chapter we adopt linear viscoelasticity to demonstrate the utility of our theory with the LEFM stress fields. Our theory can be extended to more sophisticated material behaviors provided that solutions for the stress and strain fields become available.

3.3.1 Linear viscoelasticity

Under the assumption of linear viscoelasticity, the strain \mathbf{E} at a material point with coordinates \mathbf{X} is related to the stress \mathbf{S} through the following hereditary integral for any time $t \geq 0$ [16]:

$$\mathbf{E}(\mathbf{X}, t) = \int_0^t \mathbb{J}(t-t') \frac{\partial \mathbf{S}(\mathbf{X}, t')}{\partial t'} dt', \quad (3.12)$$

where the fourth-order tensor \mathbb{J} is the tensorial creep function. Here we have assumed that the stress history starts at zero time, i.e., $\mathbf{S}(\mathbf{X}, t')$ vanishes for $t' < 0$, without loss of generality. We further assume material isotropy so that \mathbb{J} can be written as

$$\mathbb{J}(t) = \frac{J_k(t) - J_s(t)}{3} \mathbf{I} \otimes \mathbf{I} + \frac{J_s(t)}{2} (\mathbb{I} + \tilde{\mathbb{I}}), \quad (3.13)$$

where \mathbf{I} is the identity tensor, \otimes is the dyad operator, \mathbb{I} and $\tilde{\mathbb{I}}$ are fourth-order identity tensors. For a Cartesian coordinate system with basis vectors \mathbf{e}_i ($i = 1, 2$ or 3), these two fourth-order identity tensors are [55]

$$\mathbb{I} = \sum_{j=1}^3 \sum_{i=1}^3 \mathbf{e}_i \otimes \mathbf{e}_j \otimes \mathbf{e}_i \otimes \mathbf{e}_j, \quad (3.14)$$

$$\tilde{\mathbb{I}} = \sum_{j=1}^3 \sum_{i=1}^3 \mathbf{e}_i \otimes \mathbf{e}_j \otimes \mathbf{e}_j \otimes \mathbf{e}_i. \quad (3.15)$$

The Cartesian components of these two fourth-order tensors can be written using the Kronecker delta symbol δ_{ij} as $(\mathbb{I})_{ijmn} = \delta_{im}\delta_{jn}$ and $(\tilde{\mathbb{I}})_{ijmn} = \delta_{in}\delta_{jm}$. In addition, $J_k(t)$ and $J_s(t)$ represent the bulk and shear compliance functions, respectively. It is worth mentioning that Laplace transform of Eq.(3.12) recovers the stress-strain relation of linear elasticity [16]. This feature leads to the correspondence principle connecting the solutions for linear elasticity to those for linear viscoelasticity, which will be elaborated in the next section.

For elastomers, the bulk compliance is typically much smaller than the shear compliance so that they can be assumed to be incompressible. Following this assumption, we set $J_k(t)$ to be identically zero. This means the viscoelastic solid has a constant Poisson's ratio of $\nu = 1/2$. Substituting Eq.(3.13) into Eq.(3.12), we obtain

$$\text{tr}(\mathbf{E}(\mathbf{X}, t)) = 0, \quad (3.16)$$

$$\mathbf{E}^{dev}(\mathbf{X}, t) = \int_0^t J_s(t-t') \frac{\partial \mathbf{S}^{dev}(\mathbf{X}, t')}{\partial t'} dt', \quad (3.17)$$

where $\mathbf{E}^{dev} = \mathbf{E} - \text{tr}(\mathbf{E})\mathbf{I}/3$ and $\mathbf{S}^{dev} = \mathbf{S} - \text{tr}(\mathbf{S})\mathbf{I}/3$ are the deviatoric strain and stress tensors, respectively. Since $\text{tr}(\mathbf{E}) = 0$, we have $\mathbf{E}^{dev} = \mathbf{E}$.

3.3.2 Correspondence principle and stress field

The correspondence principle refers to a method of solving boundary value problems in linear viscoelastic solids. Consider a generic mixed boundary value problem where displacement and traction boundary conditions are prescribed on different regions of the boundary. The field equations and boundary conditions for linear viscoelasticity can be converted into the same form as those for linear elasticity through integral transform such as the Laplace transform [16]. Therefore, the solution of the viscoelastic problem in the transformed domain can be obtained from the corresponding elastic problem. Inverting the solution in the transformed domain yields the actual solution for the boundary value problem. However, this method is valid only if regions of displacement and traction boundary conditions do not vary with time [16]. In case of fracture problems, this means the correspondence principle is only applicable for stationary cracks.

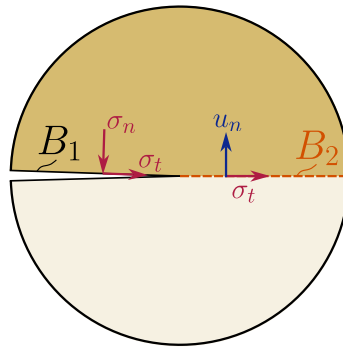


Figure 3.3: Extended correspondence principle for a 2D Mode-I semi-infinite crack in an infinite solid. The boundary regions B_1 and B_2 represent the crack surface and the surface directly ahead of the crack tip. Crack propagation causes both B_1 and B_2 to vary with time.

Graham [41] derived that, under specific circumstances, the correspondence principle can be

extended to problems with boundary regions that vary with time, e.g., crack propagation [42]. To illustrate this, let us consider a 2D Mode-I semi-infinite crack in an infinite solid (see Fig.(3.3)). Symmetry allows us to consider only the top half of the solid, which forms a half-space and possesses two boundary regions: B_1 for the crack surface and B_2 for the surface ahead of the crack. The boundary conditions are listed below:

- On $B_1 + B_2$, the shear traction σ_t is zero;
- On B_1 , the normal traction σ_n is zero;
- On B_2 , the normal displacement u_n is zero.

Crack propagation implies that both regions of B_1 and B_2 are not fixed with time. However, if the following conditions are satisfied for the elastic solution, the correspondence principle is applicable [119]:

- (i) The area of B_1 is monotonically increasing, meaning that the crack can propagate (i.e., $dA/dt \geq 0$) but cannot close.
- (ii) On B_2 , the normal traction σ_n is independent of material properties.
- (iii) On B_1 , the normal displacement u_n can be written as a function of material properties multiplied by a distribution that is independent of material properties.

The elastic solution for this problem is the Mode-I K -field in LEFM [146]. It is straightforward to verify that Conditions (ii) and (iii) are both satisfied. Therefore, as long as the crack is propagating (i.e., $dA/dt \geq 0$), one can obtain the viscoelastic solution from the elastic solution using the correspondence principle. This argument can be extended to Mode-II and Mode-III cracks as well, thereby establishing the correspondence principle for crack propagation under any fracture modes or their combinations.

A key implication of the correspondence principle is the stress field for propagating cracks in linear viscoelastic solids: since the stress field from the elastic solution is governed only by the stress intensity factor K and is independent of material properties, the same stress field is valid for the

viscoelastic solution. As a result, the stress field around a propagating crack in linear viscoelastic solids also follows the LEFM K -field. If a cohesive zone is introduced ahead of the crack tip, it can cause the crack tip stress field to deviate from the K -field by regularizing the singularity. As long as the cohesive stress is independent of the elastic constants, the correspondence principle still holds and the viscoelastic stress field is still the same as the elastic one [57, 65, 119].

The above discussion is for a semi-infinite crack in an infinite body. For a finite body consisting of linear viscoelastic solid (e.g., Ω in Fig.(3.1)), we have assumed the crack is planar and propagates in a self-similar manner. It follows that the local stress field near the crack front is given by the K -field regularized by the cohesive zone. The stress intensity factor K , however, depends on the boundary condition far away from the crack front, i.e., the far-field boundary (e.g., $\partial\Omega$ in Fig.(3.1)). For the extended correspondence principle to be valid, K should be independent of material properties, otherwise Conditions (ii) and (iii) discussed above are not satisfied. This requires the far field to be subjected to traction boundary conditions. If displacement boundary conditions are applied in the far field, Schapery [119] argued that the displacement boundary conditions can be equivalently replaced by traction boundary conditions with certain distributions of traction that can reproduce the prescribed boundary displacements. This argument requires the viscoelastic solid in the far field to be in the fully relaxed state, which is the assumption to be adopted in Section 3.4. Under these conditions, we can leverage the numerous LEFM solutions connecting the stress intensity factor K to the far-field boundary conditions [129], and hence establish the local stress field near a propagating crack in linear viscoelastic solids.

Finally, we emphasize that in this work, the crack is assumed to only undergo propagation ($\dot{A} > 0$) without any closure. If crack closure occurs, which is often encountered in contact problems, another version of the extended correspondence principle should be considered [120, 43].

3.3.3 Creep compliance

To further evaluate the local strain field near the crack front, we need to specify the shear creep compliance function $J_s(t)$ in Eq.(3.17). It is more convenient to use the uniaxial creep

compliance function $J(t)$. These two functions are related through (see Appendix B)

$$J_s(t) = (1 + \nu)J(t) = \frac{3}{2}J(t). \quad (3.18)$$

Recall that the Poisson's ratio $\nu = 1/2$ due to the incompressibility assumption.

While there are many models for the creep compliance $J(t)$, for simplicity we adopt the standard linear solid model. As shown in Appendix B, $J(t)$ for the standard linear solid model is

$$J(t) = \frac{1}{E_\infty} - \frac{E_0 - E_\infty}{E_0 E_\infty} \exp\left(-\frac{t}{\tau_c}\right) \quad (3.19)$$

where $E_0 = E_1 + E_2$, $E_\infty = E_2$ and $\tau_c = (E_0/E_\infty)\tau$. The parameters E_1 and τ represent the spring modulus and the dashpot relaxation time of a branch in the standard linear solid model, while E_2 is the spring modulus of the other parallel branch. Substituting Eq.(3.18) into Eq.(3.17) and applying integration by parts, we can write Eq.(3.17) as

$$\mathbf{E}(\mathbf{X}, t) = \mathbf{E}^{dev}(\mathbf{X}, t) = \frac{3}{2}J_0\mathbf{S}^{dev}(\mathbf{X}, t) + \int_0^t \frac{3}{2}\dot{J}(t-t')\mathbf{S}^{dev}(\mathbf{X}, t')dt', \quad (3.20)$$

where $\dot{J}(t) = dJ(t)/dt$, $J_0 = J(t=0)$ and we have implemented the incompressibility condition $tr(\mathbf{E}) = 0$.

3.3.4 Free energy density

For arbitrary isotropic incompressible linear viscoelastic solids with prescribed creep compliance $J(t)$ (or relaxation function), there is no unique thermodynamic definition for the Helmholtz free energy density ψ . While such a definition is unnecessary to derive an expression of the intrinsic energy release rate G_0 , evaluation of G and G_d^s requires the definition of ψ . For the standard linear solid model featuring a single dissipative element, the free energy depends on the stress and a single internal variable \mathbf{Q} . In Appendix B, we show that the following expression is a relevant choice for Poisson's ratio $\nu = 1/2$:

$$\psi(\mathbf{S}, \mathbf{Q}) = \frac{3}{4} \left(\frac{(\mathbf{S}^{dev} - \mathbf{Q}^{dev}) : (\mathbf{S}^{dev} - \mathbf{Q}^{dev})}{E_\infty} + \frac{\mathbf{Q}^{dev} : \mathbf{Q}^{dev}}{E_0 - E_\infty} \right), \quad (3.21)$$

where \mathbf{Q}^{dev} is the deviatoric part of the non-equilibrium stress \mathbf{Q} defined as [55]:

$$\mathbf{Q}(t) = \mathcal{R}_0 \mathbf{S}(t) + \int_0^t \dot{\mathcal{R}}(t-t') \mathbf{S}(t') dt'. \quad (3.22)$$

The function \mathcal{R} is the *creep ratio* as defined below and $\mathcal{R}_0 = \mathcal{R}(t=0)$. It controls the additional stress due to viscous effects: if the material is kept at constant strain for enough time, this stress will eventually relax.

$$\mathcal{R}(t) = (1 - \frac{E_\infty}{E_0}) \exp(-\frac{t}{\tau_c}). \quad (3.23)$$

For example, if a constant stress \mathbf{S} is applied since $t=0$,

$$\psi(t \rightarrow 0) \rightarrow \frac{3}{4} \frac{\mathbf{S}^{dev} : \mathbf{S}^{dev}}{E_0}, \quad \psi(t \gg \tau_c) \rightarrow \frac{3}{4} \frac{\mathbf{S}^{dev} : \mathbf{S}^{dev}}{E_\infty}. \quad (3.24)$$

As noted in the literature [9, 53, 38], the harmonic potentials of Eq.(5.4) are choices. This is because rheological models, like the standard linear solid model, prescribe the stress-strain relationship rather than the free energy.

3.4 The Pure Shear Problem

In this section, we use the fracture criterion (Section 3.2) and linear viscoelasticity (Section 3.3) to study cyclic crack growth. This requires us to specify the geometry and boundary conditions of the solid Ω . Fig.(3.4) illustrates several experimental configurations for characterizing crack growth in rubbers. Among them, we choose the pure shear configuration (Fig.(3.4a)) to demonstrate the theory for cyclic crack growth, since it allows the fracture criterion to be cast into a form for which numerical solution of crack extension per cycle is tractable. Extension to the other configurations (Figs.(3.4b-d)) will be discussed in Section 3.4.5

3.4.1 Simplifying assumptions

The pure shear configuration (Fig.(3.4a)) consists of a thin sheet geometry. The width L_s is much larger than the height H , i.e., $L_s \gg H$, and thus can be taken to be infinity for theoretical analysis [110]. The top and bottom boundaries of the sample are clamped by rigid grips and are

separated by a vertical displacement $U(t)$. This displacement loading drives the Mode-I growth of a crack at the sample's left edge. Since the applied displacement is independent of the crack area A and the rest of the boundary $\partial\Omega$ is traction free, we conclude that $\int_{\partial\Omega} \mathbf{t} \cdot (\partial\mathbf{u}/\partial A) dS = 0$. Therefore, the intrinsic energy release rate G_0 in Eq.(4.9) becomes:

$$G_0 = - \int_{\Omega} \mathbf{S} : \frac{\partial \mathbf{E}}{\partial A} dV. \quad (3.25)$$

Three assumptions are made to further simplify the expression of G_0 .

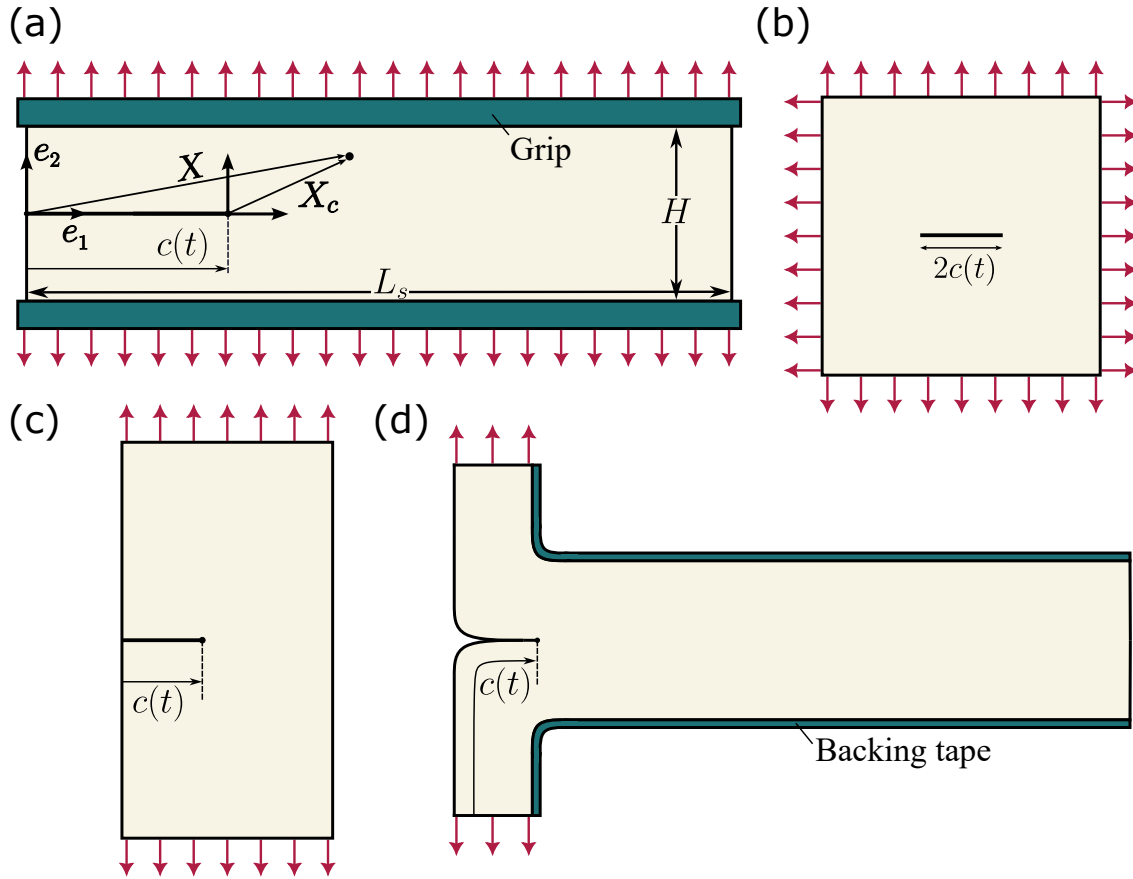


Figure 3.4: (a) Pure shear strip with $H \ll L_s$, initial crack length $c_0 \ll L_s$ and thickness $w \ll L_s$. The material point located at \mathbf{X} in the fixed reference frame $(\mathbf{e}_1, \mathbf{e}_2)$ is denoted \mathbf{X}_c in the translating reference frame centered at the moving crack tip. (b) Biaxially loaded center-cracked plate. (c) Single edge notch configuration. (d) Simple extension configuration.

First, we assume the *plane stress* condition due to the thin-sheet geometry and the traction free

lateral surface. With respect to the Cartesian basis vector \mathbf{e}_1 , \mathbf{e}_2 and \mathbf{e}_3 (see Fig.(3.4a)), the matrix of stress tensor \mathbf{S} is

$$[\mathbf{S}] = \begin{bmatrix} S_{11} & S_{12} & 0 \\ S_{12} & S_{22} & 0 \\ 0 & 0 & 0 \end{bmatrix}. \quad (3.26)$$

In addition, the stress and strain fields are uniform along the thickness direction \mathbf{e}_3 , thereby reducing the volumetric integral in Eq.(3.25) to a surface integral:

$$G_0 = - \int_{\partial\Omega_l} \mathbf{S} : \frac{\partial \mathbf{E}}{\partial c} dS_l, \quad (3.27)$$

where c is the crack length measured in the reference configuration and dS_l denotes surface element on sample's lateral surface $\partial\Omega_l$. Note that we have used the identities that $c = A/w$ and $dS_l = dV/w$ where w is the out-of-plane thickness. Accordingly, the crack speed is

$$V(t) = \frac{\dot{A}}{w} = \frac{dc}{dt}. \quad (3.28)$$

Second, we assume the extended correspondence principle is valid, which requires two conditions according to the discussion in Section 3.3.2: (i) only crack growth is allowed (i.e., $V \geq 0$), and (ii) material points far away from the crack tip are fully relaxed. The latter condition effectively constrains viscoelastic effects to a local region around the crack tip, which is known as *small scale creep* [57]. It is needed to equivalently replace the prescribed displacement $U(t)$ on the boundary by a distribution of traction, otherwise the extended correspondence principle may not apply [119]. Under these two assumptions, the stress field $\mathbf{S}(\mathbf{X}, c, t)$ for a linear viscoelastic solid is the same as the solution for a linear elastic solid. In case of a linear elastic solid, the stress field $\mathbf{S}(\mathbf{X}, c, t)$ for the pure shear configuration is *translationally invariant* relative to the moving crack tip. To leverage this feature, we define a translating frame centered at the crack tip. The coordinate \mathbf{X}_c of a material point in the translating frame is related to its coordinate \mathbf{X} in the fixed frame through (see Fig.(3.4a)):

$$\mathbf{X}_c = \mathbf{X} - c(t)\mathbf{e}_1. \quad (3.29)$$

Translational invariance implies the stress field follows the same distribution in terms of \mathbf{X}_c . Moreover, linearity dictates that the applied displacement $U(t)$ varies the stress field proportionally without changing its distribution. Therefore, we can write the stress field in terms of a time-dependent amplitude $K(t)$ multiplied by a fixed distribution $\mathbf{d}(\mathbf{X}_c)$:

$$\mathbf{S}(\mathbf{X}, c, t) = K(t)\mathbf{d}(\mathbf{X}_c). \quad (3.30)$$

Near the crack tip, the stress field is governed by the Mode-I K -field. As a result, $K(t)$ is recognized as the Mode-I stress intensity factor. The extended correspondence principle dictates that Eq.(3.30) is also valid for our viscoelastic solid as long as the crack speed $V \geq 0$ and the far field is fully relaxed. The relaxed far field also allows us to relate $K(t)$ to the applied displacement $U(t)$ through the following equation (for pure shear configuration under plane stress and $\nu = 1/2$) [65, 113]:

$$K(t) = E_\infty \epsilon_\infty \sqrt{\frac{2H}{3}} = \frac{E_\infty}{H} \sqrt{\frac{2H}{3}} U(t), \quad (3.31)$$

where $\epsilon_\infty = U(t)/H$ is the tensile strain far ahead of the crack tip.

Third, we assume the *quasi-steady-state* condition [49] to further simplify the strain field $\mathbf{E}(\mathbf{X}, c, t)$. This condition is analogous to the steady-state condition for crack growth under static loading [57]. It states that the crack growth per cycle dc/dN has reached a constant and each cycle induces the same changes to the strain field around the crack tip. Under this assumption, the strain at a material point only depends on its relative position to the crack tip \mathbf{X}_c and the time (or equivalently, the applied displacement $U(t)$), i.e., $\mathbf{E}(\mathbf{X}, c, t) = \mathbf{E}(\mathbf{X}_c, t)$. Note that this relation is not readily concluded from the stress field in Eq.(3.30), since the stress-strain relation in Eq.(3.20) involves a convolutional integral. With the quasi-steady-state condition, we have $\partial\mathbf{E}/\partial c = -\partial\mathbf{E}/\partial X_c$ where $X_c = \mathbf{X}_c \cdot \mathbf{e}_1$ and $Y_c = \mathbf{X}_c \cdot \mathbf{e}_2$ are the in-plane Cartesian coordinates of \mathbf{X}_c . Therefore, Eq.(3.27) becomes

$$G_0 = \int_{\partial\Omega_l} \mathbf{S} : \frac{\partial\mathbf{E}}{\partial X_c} dS_l. \quad (3.32)$$

Substituting Eq.(3.20) into Eq.(3.32), we can rewrite G_0 in Eq.(4.9) into the following form

(see Appendix C for detailed derivation):

$$G_0 = J_0 K^2(t) \mathcal{I}_{cc} + K(t) \int_0^t \dot{J}(t-t') K(t') \mathcal{I}_{cc'} dt', \quad (3.33)$$

where the spatial integrals \mathcal{I}_{cc} and $\mathcal{I}_{cc'}$ are obtained as,

$$\mathcal{I}_{cc} = \frac{3}{2} \int_{\mathbf{X}_c} \mathbf{d}(\mathbf{X}_c) : \frac{\partial \mathbf{d}^{dev}}{\partial X_c}(\mathbf{X}_c) d\mathbf{X}_c, \quad (3.34)$$

$$\mathcal{I}_{cc'} = \frac{3}{2} \int_{\mathbf{X}_c} \mathbf{d}(\mathbf{X}_c) : \frac{\partial \mathbf{d}^{dev}}{\partial X_c}(\mathbf{X}_{c'}) d\mathbf{X}_c. \quad (3.35)$$

We have used the notations $\mathbf{d}^{dev} = \mathbf{d} - \text{tr}(\mathbf{d})\mathbf{I}/3$, $\mathbf{X}_{c'} = \mathbf{X}_c + \Delta c(t, t')\mathbf{e}_1$ and $\Delta c(t, t') = c(t) - c(t')$.

3.4.2 Importance of the far field

Evaluation of G_0 in Eq.(3.33) requires us to know the spatial distribution of stress $\mathbf{d}(\mathbf{X}_c)$ in Eqs.(3.34,3.35). Near the crack tip, $\mathbf{d}(\mathbf{X}_c)$ is given by the Mode-I K -field in LEFM, which is denoted as \mathbf{f} . Specifically, the matrix of \mathbf{f} with respect to the Cartesian basis \mathbf{e}_1 , \mathbf{e}_2 and \mathbf{e}_3 is [146]:

$$\mathbf{f}(r, \theta) = \frac{1}{\sqrt{2\pi r}} \cos \frac{\theta}{2} \begin{bmatrix} 1 - \sin \frac{\theta}{2} \sin \frac{3\theta}{2} & \sin \frac{\theta}{2} \cos \frac{3\theta}{2} & 0 \\ \sin \frac{\theta}{2} \cos \frac{3\theta}{2} & 1 + \sin \frac{\theta}{2} \sin \frac{3\theta}{2} & 0 \\ 0 & 0 & 0 \end{bmatrix}, \quad (3.36)$$

where $r = \|\mathbf{X}_c\|$ and $\theta = \arccos(\mathbf{e}_1 \cdot \mathbf{X}_c / \|\mathbf{X}_c\|)$ are the polar coordinates measured from the crack tip. Note that \mathbf{f} is singular as the crack tip is approached ($r \rightarrow 0$) and vanishes far away from the crack tip ($r \rightarrow \infty$). Neither limit is physically realistic for the pure shear configuration. In particular, recall the discussion in Section 3.2 that the crack tip singularity must be regularized. Therefore, \mathbf{f} is only valid in an annular region $l \leq r \leq R$ surrounding the crack tip.

As $r \rightarrow 0$, the stress field is governed by the cohesive zone describing the crack tip fracture process. The lower limit l is interpreted as the cutoff length below which the K -field in Eq.(3.36) deviates from the actual stress field. Since the actual stress field is finite at the crack tip, we assume the contribution for $r < l$ to \mathcal{I}_{cc} and $\mathcal{I}_{cc'}$ is negligible if l is sufficiently small. Therefore, we simply remove the area of $r < l$ from the spatial integrals \mathcal{I}_{cc} and $\mathcal{I}_{cc'}$. This approach has been adopted in previous viscoelastic fracture theories under static loading [20, 107]. Although it is possible to

obtain solutions for the stress field that include the cohesive zone [65, 119], such solutions depend on the detailed cohesive zone model (e.g., the Dugdale-Barenblatt model [57]). Also, recently it was shown the two approaches to regularize crack tip singularity (e.g., cut-off length or cohesive zone) generate similar results for viscoelastic fracture under static loading [57]. For simplicity, we adopt the cut-off length approach and follow de Gennes [20] to impose a constant l .

The upper limit R is needed because the \mathbf{f} cannot capture the stress distribution in the far field. Previous viscoelastic fracture theories [20, 107] focus on calculating the dissipative component of energy release rate G_d^s under static loading. Because the far field is fully relaxed, it does not contribute to G_d^s and therefore the K -field approximation is sufficient. In contrast, our formulation targets the intrinsic energy release rate G_0 , which requires us to evaluate the spatial gradient of stress field, i.e., $\partial \mathbf{d}^{dev}/\partial X_c$ in Eqs.(3.34,3.35). This gradient does not vanish in the far field. As a result, in principle we need to know \mathbf{d} in the far field. Although analytical solution for the stress field in the pure shear configuration is available [66], it is difficult to apply such solution in our formulation due to the mathematical complexity. In the next section, we show that this difficulty can be circumvented by introducing the concept of the *phantom state*.

3.4.3 The phantom state

At every instant t we may define an imaginary state, called the *phantom state* [49], in which the crack is at position $c(t)$ and is not subjected to any history of crack propagation. This means that for all $t' \leq t$, $c(t') = c(t)$. The phantom state is subjected to the same cyclic loading $U(t)$ as the actual state, and the far field is also fully relaxed. Therefore, the extended correspondence principle dictates that the stress field in Eq.(3.30) is also valid for the phantom state except that c is now a constant. However, the strain field $\hat{\mathbf{E}}(\mathbf{X}_c, t)$ is different from $\mathbf{E}(\mathbf{X}_c, t)$ for the actual state (hereafter we will denote variables in the phantom state using hats). As opposed to the actual state, \mathbf{X}_c for a given material point is independent of time in the phantom state. Specifically,

substituting Eq.(3.30) with a constant c into Eq.(3.20), we obtain

$$\hat{\mathbf{E}}(\mathbf{X}_c, t) = \left(\frac{3}{2} J_0 K(t) + \int_0^t \frac{3}{2} \dot{J}(t-t') K(t') dt' \right) \mathbf{d}^{dev}(\mathbf{X}_c). \quad (3.37)$$

This means at a given t the strain field $\hat{\mathbf{E}}(\mathbf{X}_c, t)$ in the phantom state follows the same distribution as the deviatoric stress field, i.e., $\mathbf{d}(\mathbf{X}_c)$. Physically this is because all material points in the phantom state follows the same frequency of cyclic loading. Although there is no crack growth in the phantom state, we can still define a nominal intrinsic energy release rate \hat{G}_0 for the phantom state using Eq.(3.32). As derived in Appendix D, \hat{G}_0 is the same as the global energy release rate G in the actual state:

$$\hat{G}_0 = G = \frac{2H}{3} E_\infty \epsilon_\infty^2, \quad (3.38)$$

where $\epsilon_\infty = U(t)/H$ is the tensile strain far ahead of the crack tip. By comparing Eq.(3.31) and Eq.(3.38), we conclude that $G = K^2/E_\infty$ as expected from the assumption of relaxed far field.

The phantom state enables the following equation (see Appendix D):

$$G_d^s = G - G_0 = \hat{G}_0 - G_0 = K(t) \int_0^t \dot{J}(t-t') K(t') (\mathcal{I}_{cc} - \mathcal{I}_{cc'}) dt'. \quad (3.39)$$

Evaluation of $\mathcal{D}_{cc'} \equiv \mathcal{I}_{cc} - \mathcal{I}_{cc'}$ does not require the solution of \mathbf{d} in the far field ($r \rightarrow R$). This is because the spatial distributions in the phantom and actual states are identical in the far field, and thus contributions of the far field \mathbf{d} to \mathcal{I}_{cc} and $\mathcal{I}_{cc'}$ are canceled. This allows us to utilize the K -field solution of \mathbf{d} for $l \leq r \leq R$ to evaluate $\mathcal{D}_{cc'}$.

3.4.4 Limitations

Solutions for cyclic crack growth in linear viscoelastic solids presented in Guo *et al* [49] are subjected to two limitations: *slow loading* and *slow crack propagation*. The first limitation, *slow loading*, originates from the necessity to assume a relaxed far field, otherwise the extended correspondence principle may not be valid and hence a solution for the stress field would be lacking. This limitation is retained in this work given our assumption of a relaxed far field, which requires the period of cyclic loading, denoted as T , is much larger than the viscoelastic relaxation time τ ,

i.e., $T \gg \tau$. Efforts to extend our theory in the regime of $T \sim \tau$ or $T < \tau$ should therefore focus on searching for solutions of the stress field. For example, problems with traction boundary conditions are not subjected to this limitation, as the extended correspondence principle is still applicable even if the far field is not fully relaxed.

The limitation of *slow crack propagation* was employed in Guo *et al* [49] merely for mathematical convenience (to further simplify Eq.(3.39)). Therefore, it should be resolved through the development of an numerical scheme for Eq.(3.39). However, the K -field approximation \mathbf{f} for the stress distribution \mathbf{d} also imposes a limit on how fast the crack can propagate. To illustrate this point, we define $(\mathcal{D}_{cc'})_a$ as the value of $\mathcal{D}_{cc'}$ where \mathbf{d} is replaced by the K -field approximation \mathbf{f} in Eq.(3.36):

$$(\mathcal{D}_{cc'})_a = \frac{3}{2} \int_{\mathbf{X}_c} \mathbf{f}(\mathbf{X}_c) : \frac{\partial}{\partial \mathbf{X}_c} [\mathbf{f}^{dev}(\mathbf{X}_c) - \mathbf{f}^{dev}(\mathbf{X}_{c'})] d\mathbf{X}_c, \quad (3.40)$$

where $\mathbf{f}^{dev} = \mathbf{f} - \text{tr}(\mathbf{f})\mathbf{I}/3$. The fact that \mathbf{f} only accurately represents the actual distribution \mathbf{d} for $\|\mathbf{X}_c\| \leq R$ has no impact and $\mathcal{D}_{cc'} \simeq (\mathcal{D}_{cc'})_a$ if the following condition is met

$$\mathbf{f}^{dev}(\mathbf{X}_c) - \mathbf{f}^{dev}(\mathbf{X}_{c'}) \rightarrow \mathbf{0} \text{ for } \|\mathbf{X}_c\| \rightarrow R. \quad (3.41)$$

A less restrictive condition can be formulated by noticing that, for $t' < t - \tau_c$, the term $\dot{J}(t-t') \rightarrow 0$ in Eq.(3.39). Therefore, one can afford to have inaccurate values $(\mathcal{D}_{cc'})_a \neq \mathcal{D}_{cc'}$ for $c(t' < t - \tau_c)$ since it will not affect the overall value of the integral in Eq.(3.39). This means we can relax our criteria to:

$$\mathbf{f}^{dev}(\mathbf{X}_c) - \mathbf{f}^{dev}(\mathbf{X}_c + \Delta c(t, t' \geq t - \tau_c)) \mathbf{e}_1 \rightarrow \mathbf{0} \text{ for } \|\mathbf{X}_c\| \rightarrow R. \quad (3.42)$$

We may compute the limiting crack propagation speed V_{lim} such that Eq.(3.42) is satisfied $\forall V < V_{lim}$. In particular we can show

$$V_{lim} = \alpha \frac{R}{\tau_c}, \quad (3.43)$$

where $\alpha = 0.04$. The method for computing α is detailed in Section 3.5.4. In Guo *et al* [49], the condition of $V \ll l/\tau_c$ is required to simplify Eq.(3.39). Although here we also need to impose an upper limit on the crack speed in order to use the approximation \mathbf{f} , we expect $V_{lim} \gg l/\tau_c$ since

the region of validity R of \mathbf{f} is expected to be much larger than $25l$. Solving Eq.(3.39) numerically therefore allows us to explore a much larger solution space in terms of crack speed as compared to the analytical simplification in [49].

3.4.5 Beyond pure shear fracture

Extension of the formulation for pure shear configuration to other configurations is possible. For example, three additional configurations are shown in Figs.(3.4b-d): a central crack under biaxial tension, single edge notch and simple extension (or T-peel). In particular, the simple extension configuration (Fig.(3.4d)) is similar to the pure shear configuration in terms of geometry, but the external loading is applied through a pair of peel forces on the inextensible backing layer. As a result, the stress field is expected to be non-zero only in the region surrounding the crack tip and is translationally variant relative to the crack tip. Therefore, the phantom state is no longer needed for the simple extension configuration. The global energy release rate G comes from the work of peel forces, while the dissipative energy release rate G_d^s is contributed by material points around the crack tip and is governed by the coupling between cyclic loading and crack speed.

The configurations of central crack and single edge notch (Figs.(3.4b-c)), however, are significantly different from pure shear in that the stress field is no longer translationally invariant relative to the crack tip. Specifically, an increase in the crack length $c(t)$ not only changes the position of a material point relative to the crack tip, but also affects the stress intensity factor $K(t)$ (e.g., as shown by the Westergaard's solution for a central crack subjected to biaxial tension [4]). As a result, the *quasi-steady-state* assumption may not hold exactly. However, because fatigue fracture typically features low values of dc/dN , the increase in crack length over several cycles may be small enough so that its effect on the stress intensity factor $K(t)$ can be neglected and the *quasi-steady-state* assumption is approximately valid.

For more general fatigue fracture configurations, solutions for the stress field may not be readily available due to the complex geometry or loading condition. In this case, one may need to resort to finite element simulations or experimental measurements [111] to determine the stress or strain

fields, which can then be used in our framework to study fatigue fracture at lower computational cost.

3.5 Numerical Methods

In this section, we present numerical methods to solve for the cyclic crack extension for the pure shear configuration from Eq.(3.39). The assumption of relaxed far field allows us to replace the displacement loading $U(t)$ by a prescribed history of stress intensity factor $K(t)$ which is further related to the global energy release rate through $G(t) = K^2(t)/E_\infty$.

3.5.1 Implicit scheme

To numerically solve for the crack extension in Eq.(3.39), we first introduce the following discretization for the time t :

$$t_0 = 0, t_1 = \delta t, \dots, t_k = k\delta t, \dots \quad (3.44)$$

Since Eq.(3.39) also involves the time variable t' , we discretize it using the same time increment δt :

$$t'_0 = 0, t'_1 = \delta t, \dots, t'_s = s\delta t, \dots \quad (3.45)$$

Therefore, the discretized form of Eq.(3.39) at $t = t_k$ is

$$G_d^s(t_k) = K(t_k) \sum_{s=0}^k J(t_k - t'_s) K(t'_s) \mathcal{D}_{cc'}(t_k, t'_s) \delta t. \quad (3.46)$$

Our goal is to solve for the history of crack extension $c(t)$. Following the discretization in Eq.(3.44), we denote c_k as the crack length at t_k . We adopt an implicit scheme in which the increment in crack length is $\delta c_k = c_k - c_{k-1}$ where c_{k-1} is the crack length at t_{k-1} . Note that the unknown crack extension $c(t)$ is hidden in the spatial integral $\mathcal{D}_{cc'}(t_k, t'_s)$ (see Eq.(3.40)):

$$\mathcal{D}_{cc'} = \frac{3}{2} \iint \mathbf{f}(\mathbf{X}_c) : \left[\frac{\partial \mathbf{f}^{dev}}{\partial X_c}(\mathbf{X}_c) - \frac{\partial \mathbf{f}^{dev}}{\partial X_{c'}}(\mathbf{X}_{c'}) \right] dX_c dY_c, \quad (3.47)$$

$$\mathbf{X}_{c'} = \mathbf{X}_c + \Delta c(t_k, t'_s) \mathbf{e}_1 = \mathbf{X}_c + [\delta c_k + \Delta c(t_{k-1}, t'_s)] \mathbf{e}_1. \quad (3.48)$$

Recall that $\Delta c(t_k, t'_s) = c(t_k) - c(t'_s)$.

Using the fracture criterion given in Eq.(4.9) and the assumption of relaxed far field such that $G = K^2/E_\infty$, we have,

$$\begin{cases} G_d^s(t_k) = 0 & \text{if } K^2(t_k)/E_\infty < \Gamma_0 \\ G_d^s(t_k) = K^2(t_k)/E_\infty - \Gamma_0 & \text{if } K^2(t_k)/E_\infty \geq \Gamma_0 \end{cases}. \quad (3.49)$$

Provided that we can evaluate $\mathcal{D}_{cc'}$, Eq.(3.46) and Eq.(3.49) allow us to solve for the crack length increments δc_k and crack speeds $V_k = \delta c_k/\delta t$ at all time steps t_k . Specifically, we seek $\delta c_k = c_k - c_{k-1}$ as the value that minimizes the function:

$$\delta c_k = \arg \min_{\delta c} |G_d^s(t_k) - K(t_k) \sum_{s=0}^k \dot{J}(t_k - t'_s) K(t'_s) \mathcal{D}_{cc'}(t_k, t'_s) \delta t|, \quad (3.50)$$

where $\delta c = [0, 2000l]$ is the discretized solution space and l is the cut-off length at the crack tip. We use the golden section search method to solve for δc_k in this interval.

3.5.2 Numerical spatial integration

In order to evaluate increments in crack length according to Eq.(3.50), it is necessary to evaluate $\mathcal{D}_{cc'}$ for any $\Delta c(t_k, t'_s) = c(t_k) - c(t'_s)$. In the following we will omit the argument in Δc for abbreviation.

Since the integrand in Eq.(3.47) vanishes for large $\|\mathbf{X}_c\|$, we restrain the domain of integration to a square of size L . We select the size L as a compromise between accuracy and computational cost. Given that the integrand is symmetric about the horizontal line through the crack tip, we may restrain the integration domain to a rectangle of size L by $L/2$ and double the result (Fig.(3.5a)). Note that the domain size L has to satisfy $L > 2\Delta c$ to capture the features of the integrand.

Both $\mathbf{f}(\mathbf{X}_c)$ and its derivative $\frac{\partial \mathbf{f}^{dev}}{\partial \mathbf{X}_c}(\mathbf{X}_c)$ diverge as $\mathbf{X}_c \rightarrow \mathbf{0}$ (see Eq.(3.36)). In Eq.(3.47), the derivative $\frac{\partial \mathbf{f}^{dev}}{\partial \mathbf{X}_c}(\mathbf{X}_{c'})$ diverges when $\mathbf{X}_c \rightarrow -(\Delta c)\mathbf{e}_1$. Therefore, we excluded two circular regions of radius l from the domain of integration, centered on $\mathbf{X}_c = \mathbf{0}$ and $\mathbf{X}_c = -(\Delta c)\mathbf{e}_1$ (Fig.3.5b). Note the cutoff length l is treated, similarly to viscoelastic fracture theories under static loading, as a given parameter [20, 118]. The value of the spatial integral is specific to the choice of l and the final results will be normalized with respect to this cutoff length.

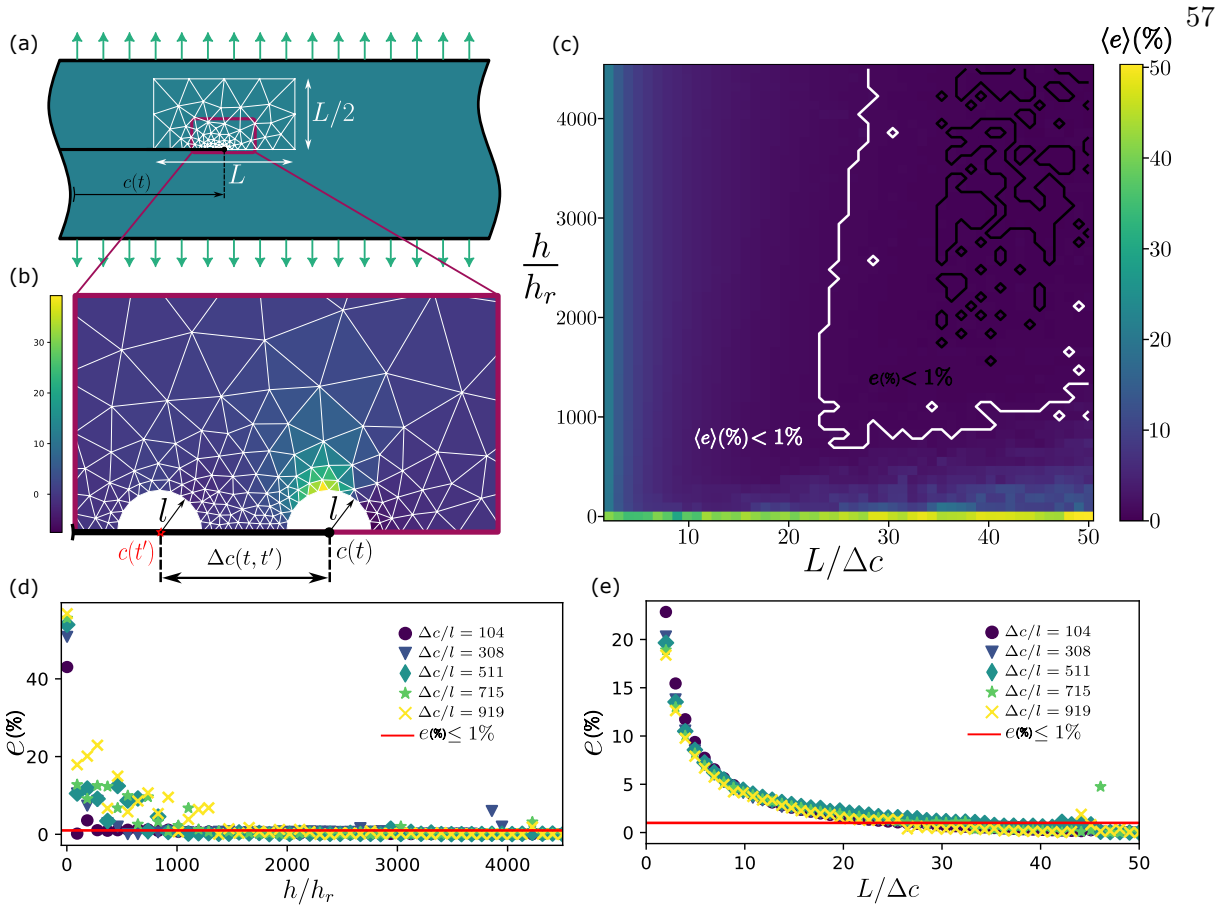


Figure 3.5: (a) The meshed region centered on the crack tip with size L by $L/2$. (b) A zoomed-in view on the mesh reveals two excluded regions located at $\mathbf{X} = c(t)\mathbf{e}_1$ and $\mathbf{X} = c(t')\mathbf{e}_1$ in the global coordinate system (respectively $\mathbf{X}_c = \mathbf{0}$ and $\mathbf{X}_c = -\Delta c(t, t')\mathbf{e}_1$ in the translating coordinate system moving with the crack tip). Element are colored according to the value of $\mathbf{f}(\mathbf{X}_c) : [\frac{\partial \mathbf{f}^{dev}}{\partial \mathbf{X}_c}(\mathbf{X}_c) - \frac{\partial \mathbf{f}^{dev}}{\partial \mathbf{X}_{c'}}(\mathbf{X}_{c'})]$. Note the mesh size is enlarged for visualization. (c) Average value of the numerical integration error $\langle e \rangle$ where e is defined per Eq.(3.51). We report here the average over 50 evenly spaced values of $\Delta c \in [2l, 1000l]$. The white contour delimits the region where $\langle e \rangle \leq 1\%$ while the black contour indicates $e(\Delta c) < 1\% \forall \Delta c \in [2l, 1000l]$. (d) Values of e for increasing ratio h/h_r and constant $L/\Delta c = 50$. The result is qualitatively similar for a wide range of $\Delta c/l$. The red line indicates acceptable precision with $e \leq 1\%$. (e) Values of e for increasing ratio $L/\Delta c$ and constant $h/h_r = 4500$. While $e \rightarrow 0\%$ at different rates when plotted against L , considering $L/\Delta c$ provides the same convergence rate for a wide range of $\Delta c/l$.

We used the generator *Gmsh* [37] to mesh our domain of integration with triangular elements. In *Gmsh*, the desired size of the elements are set at the geometrical points of the model: we set element size h for the points defining the outer boundary of the domain and h_r for the points defining the two excluded circular regions. There is a need for better accuracy when $\mathbf{X}_c \rightarrow \mathbf{0}$ and $\mathbf{X}_c \rightarrow -(\Delta c)\mathbf{e}_1$ because the functions we seek to integrate are $\sim ||\mathbf{X}_c||^{-2}$ (see Appendix E). We therefore refined the mesh in these regions with $h_r < h$. The element size in the interior of the domain is set by *Gmsh*'s default interpolation method `MeshSizeExtendFromBoundary`. We then used Gaussian quadrature with three Gaussian points per element to approximate the integral.

The value of the spatial integral $\mathcal{D}_{cc'}$ should converge for increasing domain size L and decreasing mesh sizes. We found that keeping the ratio $L/h = 10$ constant was necessary to avoid highly elongated triangular elements. We studied the convergence of the integral value as a function of the ratio h/h_r . For increasing domain size, the integral value converges toward a fixed value, with faster convergence at lower Δc . When plotted against $L/\Delta c$, however, the value of the integral converges at the same rate. Since an analytical result for the integral is lacking, we assessed convergence for a given Δc using the relative error definition:

$$e = \left| \frac{\mathcal{D}_{cc'}^*(\Delta c) - \mathcal{D}_{cc'}(\Delta c; h/h_r, L/\Delta c)}{\mathcal{D}_{cc'}^*(\Delta c)} \right|, \quad (3.51)$$

where $\mathcal{D}_{cc'}^*(\Delta c)$ was evaluated using the largest domain ($L/\Delta c = 50$) and the finest mesh ($h/h_r = 4500$) in our calculation. Fig.(3.5d) shows the convergence of e to be below the acceptance threshold (i.e., $e \leq 1\%$) under increasing h/h_r for a wide range of $\Delta c/l$. We find that it takes slightly larger h/h_r to reach the desired accuracy for larger values of $\Delta c/l$. This is because of the requirements that $L > \Delta c$ and $L/h = 10$. To maintain the ratio $L/\Delta c = 50$ at larger Δc , the domain has to be larger and therefore h has to be larger. However, for $h/h_r > 1500$ the error remains below $e < 5\%$ for any value of $\Delta c/l$ and is always acceptable for $h/h_r = 4500$, which is the value we retained to set our mesh size.

Fig.(3.5e) shows convergence of the error below 1% with increasing $L/\Delta c$. These curves overlap for a wide range of $\Delta c/l$ and we observe convergence for most values of $\Delta c/l$ after $L/\Delta c >$

33. We selected $L/\Delta c = 35$ to set our domain size in the following. Note that for larger values of $\Delta c/l > 500$, $L/\Delta c > 35$ produces large domains. Due to the condition $L/h = 10$, elements can be large close to the crack tip even at $h/h_r = 4500$: increasing the domain size further can lead to larger errors depending on the element shape close to the crack tip (e.g., see outlier points on Fig.3.5e). Further refinement of the mesh with $h/h_r > 4500$ would solve this problem, but it would be at the cost of increased computational time.

Fig.(3.5c) shows the average value $\langle e \rangle$ over 50 evenly spaced values of $\Delta c \in [2l, 1000l]$ for values of h/h_r and $L/\Delta c$. The contour corresponding to $\langle e \rangle \leq 1\%$ occupies the top right corner of the plot: it shows how the method converges overall for larger domain and finer meshes. The black contour indicates that $e < 1\%$ for all 50 values of $\Delta c \in [2l, 1000l]$.

3.5.3 The spatial integral $\mathcal{D}_{cc'}$ as a function of crack extension

Fig.(3.6) shows the value of $\mathcal{D}_{cc'}$ for $\Delta c/l \in [1.1, 1000]$ using the integration domain size of $L/\Delta c = 35$ and mesh size $h/h_r = 4500$ with $h = L/10$. This numerical result can be well fitted by the following empirical function:

$$\mathcal{D}_{cc'} = \beta \ln\left(\frac{\Delta c}{l}\right) + \beta^* \text{ for } \Delta c/l \in [1.1, 1000], \quad (3.52)$$

with $\beta = 0.373$ and $\beta^* = 0.794$. The values of coefficients β and β^* have been obtained through non-linear least squares regression, the resulting determination coefficient being 0.999.

Note the range $\Delta c/l \in [1.1, 1000]$ is limited to guarantee the accuracy of our numerical calculation of the spatial integral. We may add the point $(\Delta c = 0, \mathcal{D}_{cc'} = 0)$ since the integrand of $\mathcal{D}_{cc'}$ vanishes when $\Delta c = 0$. However, for values $0 < \mathcal{D}_{cc'} < 0.83$, the only available information is $0 < \Delta c/l < 1.1$, but we cannot determine its value from Eq.(3.52). To address this limitation, we interpolated the values of $\mathcal{D}_{cc'}$ for $0 < \Delta c/l < 1.1$ in between the two known values. We picked a quadratic interpolation to match the curvature at $\mathcal{D}_{cc'} = 0.83$. For larger values $\mathcal{D}_{cc'} > 3.38$, Eq.(3.52) indicates it may only be obtained using $\Delta c/l > 1000$. In this case, we assume the model of Eq.(3.52) would still give a reasonable estimate of the crack extension $\Delta c/l$. The spatial integral

$\mathcal{D}_{cc'}$ is thus related to the crack extension through the following relationship with $\kappa = -0.377$ and $\kappa^* = 1.169$:

$$\mathcal{D}_{cc'} = \begin{cases} \kappa(\frac{\Delta c}{l})^2 + \kappa^* \frac{\Delta c}{l} & \text{if } \Delta c/l < 1.1 \\ \beta \ln(\frac{\Delta c}{l}) + \beta^* & \text{if } \Delta c/l \geq 1.1 \end{cases}. \quad (3.53)$$

In the implicit scheme, at time t_k , we guess a value for the crack extension increment δc_k such that $\Delta c(t_k, t'_s) = \delta c_k + \Delta c(t_{k-1}, t'_s)$. Note that the value of $\Delta c(t_{k-1}, t'_s)$ is known from previous time steps. As illustrated on Fig.(3.6), we use Eq.(3.53) to determine the values of $\mathcal{D}_{cc'}$ for all guesses in the solution space $\delta c_k \in \delta \mathbf{c}$. The solution δc_k is obtained based on Eq.(3.50).

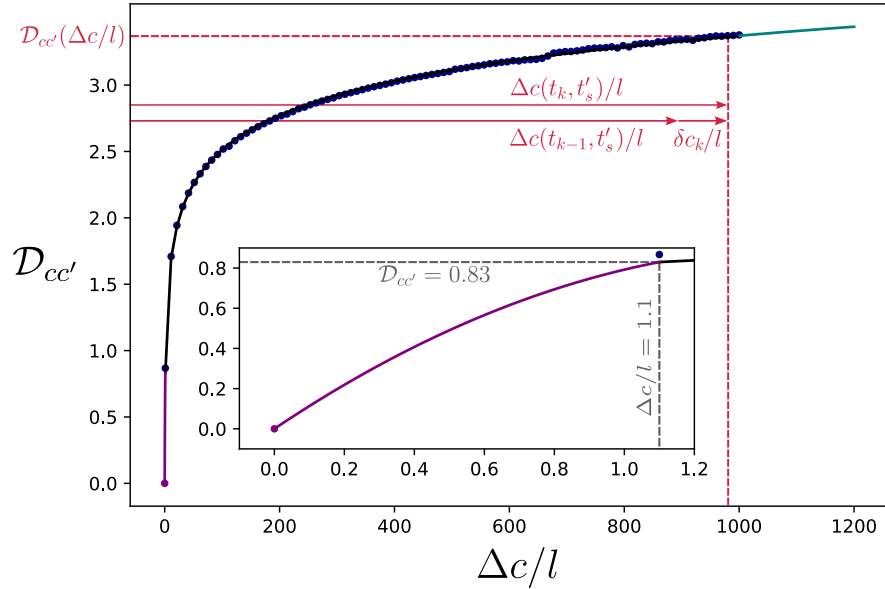


Figure 3.6: The dark blue scatter plot is $\mathcal{D}_{cc'}$ computed numerically according to the procedure described in Section 3.5.2 for $\Delta c/l \in [1.1, 1000]$. The point $(\Delta c = 0, \mathcal{D}_{cc'} = 0)$ has been added manually. The black line corresponds to the fit given as Eq.(3.52). The purple line (see inset) is the quadratic interpolation of Eq.(3.53) for $\Delta c/l < 1.1$. The cyan line shows the extension of the fitted function for $\Delta c/l > 1000$. In red we provided a visualization of the decomposition $\Delta c(t_k, t'_s) = \delta c_k + \Delta c(t_{k-1}, t'_s)$ where δc_k is the increment of crack extension guessed at time t_k in the implicit scheme.

3.5.4 Limiting crack speed

Verifying the condition stated in Eq.(3.42) is similar to finding the smallest L such that the value of the spatial integral converges. Indeed, the reason why there is convergence with increasing domain size is due to the fact that $\mathbf{f}^{dev}(\mathbf{X}_c) - \mathbf{f}^{dev}(\mathbf{X}_{c'}) \rightarrow \mathbf{0}$ for $\|\mathbf{X}_c\| \rightarrow L$. For a given value of Δc , our convergence analysis revealed that the spatial integral converges for $L > 35\Delta c$. Therefore, we conclude that the condition in Eq.(3.42) is satisfied for a given Δc as long as the integration domain with size $L_{conv} = 35\Delta c$ fits in a circular region of size R centered on the crack tip, which is the case if $L_{conv} \leq \sqrt{2}R$. The largest value of crack extension Δc_{lim} within τ_c is then $35\Delta c_{lim} = \sqrt{2}R$. We may therefore write

$$V_{lim} = \frac{\sqrt{2}}{35} \frac{R}{\tau_c}. \quad (3.54)$$

In Section 3.4.4, we named $\alpha = \sqrt{2}/35 \simeq 0.04$.

3.6 Results and Discussion

3.6.1 Comparison to finite element simulations

In this section, we compare the prediction given by our theory for the crack propagation speed under cyclic loading to the results of Finite Element Analysis (FEA). The FEA simulation was performed in the commercial software package ABAQUS (version 2020, Simulia, Providence, RI, USA) according to the model described in the supplementary information of Guo *et al* [49]. Here we briefly describe the main features of the FEA model.

3.6.1.1 Finite element simulation

The model consists of two rectangles meshed with mainly plane stress quadrilateral elements with reduced integration (CPS4R) separated by a layer of cohesive elements (COH2D4) along the projected crack path. For the bulk elements, we implemented a quasi-linear viscoelastic material behavior in order to match the behavior of the standard linear solid model described in Section 3.3. Specifically, the elastic component is modeled as an incompressible neo-Hookean solid and the

viscous component is captured by prescribing a relaxation function as a Prony series with a single relaxation time. The cohesive elements follow a bilinear traction-separation law as represented in Fig.(3.7b). This traction-separation law features the maximum cohesive stress σ_m , the maximum separation δ_m and the fracture toughness $\Gamma_0 = \sigma_m \delta_m / 2$.

The cyclic loading is applied through a prescribed vertical displacement $U(t)$ separating the upper and lower boundaries of the pure shear geometry. We denote the period of the cyclic loading as T hereafter. The crack extension $c_{FEA}(t)$ in the simulation is post-processed by counting the number of cohesive elements for which the cohesive stress dropped to zero and multiplying by their width: this is reported in Fig.(3.7c) and normalized by the maximum separation δ_m of the cohesive elements. The crack speed is obtained as $V_{FEA} = dc_{FEA}/dt$ and normalized by δ_m/τ_c , as displayed in Fig.(3.7d).

3.6.1.2 Numerical solution

As explained in Section 3.5, we impose a cyclic stress intensity factor $K(t)$ and obtain the corresponding dissipative energy release rate $(G_d^s)_{im}$ from Eq.(3.49). Fig(3.7a) shows the history of G , G_0 and $(G_d^s)_{im}$ obtained from $K(t)$ and normalized by the fracture toughness Γ_0 over three loading cycles.

The crack extension $c(t)$ is obtained using the implicit scheme algorithm described in Section 3.5. The result is reported on Fig.3.7c and normalized by the cutoff length l . The crack speed is obtained as $V = dc/dt$ and normalized by l/τ_c , as shown in Fig.(3.7d). Note the quantity G_d^s plotted in Fig.(3.7a) is defined in Eq.(3.46): if it matches the imposed value $(G_d^s)_{im}$, it means the solution $c(t)$ is indeed correct.

3.6.1.3 Comparison

We emphasize that the FEA simulation is carried out independently from the numerical solution described in Section 3.5. Differences between them are reflected in two aspects. First, the FEA simulation incorporates a cohesive zone model to regularize the crack tip singularity, as

opposed to the cutoff length l assumed in the numerical solution.

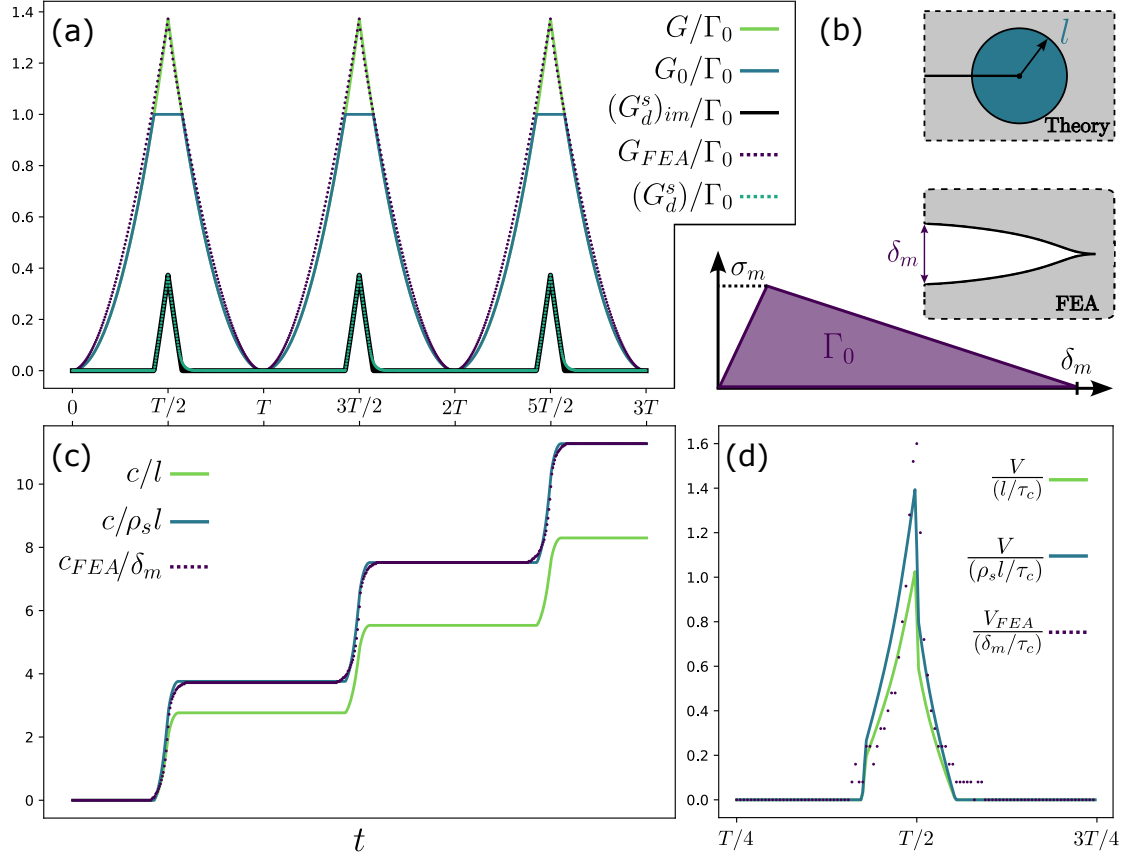


Figure 3.7: (a) History of various energy release rates over three loading cycles. The maximum value of the energy release rate G_{FEA} in the FEA simulation is set to match the maximum value of G imposed in the theory. The dissipative energy release rate G_d^s is computed numerically according to Section 3.5. The match with imposed $(G_d^s)_{im}$ is proof for the validity of the numerical solution. Note the mismatch at the end of each cycle during unloading: see comments in Section 3.6.1.4. (b) Illustration of the cut-off length l assumed in theory and the cohesive zone with bilinear traction-separation law implemented in the FEA simulation. (c) Crack length over time: comparison between FEA simulation and theory solutions. $\rho_s = 0.735$ is obtained such that $c(3T)/c_{FEA}(3T) = \rho_s l/\delta_m$. (d) Crack speed within the first cycle: comparison of FEA and theory results.

Second, the FEA simulation does not rely on certain assumptions made in our theory (e.g., *quasi-steady-state* crack growth). Comparison between these two results can illustrate whether the assumptions made in our theory are reasonable. To this end, we set $U(t)$ in the FEA simulation such that $G_{FEA}(t)$, calculated using the strain from elements in the far field, matches the prescribed $G(t) = K^2(t)/E_\infty$ (see Fig.(3.7a)). From Fig.(3.7c), we notice the curves $c_{FEA}(t)$ and $c(t)$ are qualitatively similar but differ by a multiplicative factor $\rho_s = 0.735$ in magnitude: when re-scaled by ρ_s , they agree well. Similarly, once re-scaled, results for the crack speed from the numerical solution and the FEA simulation also match.

The factor ρ_s can be interpreted as the ratio between the maximum cohesive separation δ_m in the FEA simulation and the cut-off length l in our theory. We attribute its physical origin to the difference between the FEA simulation and our theory on treating the stress field adjacent to the crack tip. Specifically, the FEA simulation incorporates a cohesive zone and thus can capture the finite crack-tip stress field regularized by the cohesive zone. In contrast, our theory neglects such finite crack-tip stress field by introducing a cutoff length l (see Fig.(3.5a)) and focuses only on the K -field. Therefore, the quantitative discrepancy between the numerical solution and the FEA result is expected. Indeed, the fact that they only differ by a re-scale factor ρ_s shows that the qualitative behavior of crack extension $c(t)$ and crack speed $V(t)$ is not sensitive to the detailed cohesive zone model. In principle, the cutoff length l should scale with the characteristic length scale of the cohesive zone model, e.g., the maximum separation δ_m , but there is no established analytical relationship between them. Therefore, a factor $\rho_s = \delta_m/l$ of order 1 is acceptable.

3.6.1.4 Mismatch during unloading

On Fig.(3.7a), we notice a mismatch between the imposed dissipative energy release rate $(G_d^s)_{im}$ (black plot) as prescribed by Eq.(3.49) and the G_d^s (teal plot) given by Eq.(3.46). For larger values of T/τ , the mismatch may happen earlier, but it only happens during unloading and the

crack speed is always zero when it occurs. Expressed in mathematical terms, the mismatch implies:

$$\frac{K^2(t)}{E_\infty} - \Gamma_0 \neq K(t) \int_0^t j(t-t') K(t') \mathcal{D}_{cc'} dt' \text{ for } dc/dt = 0. \quad (3.55)$$

This result does not contradict Eq.(3.39), since the spatial integral $\mathcal{D}_{cc'}$ has been obtained based on the assumption of active crack propagation. When the crack length is no longer increasing ($dc/dt = 0$), quantities such as $\frac{\partial \mathbf{f}}{\partial X_c}$ no longer represent a translation of the field upon crack extension. The integral on the right hand side of Eq.(3.39) may be computed even if $dc/dt = 0$ (teal plot), but is no longer expected to match the imposed dissipation term $(G_d^s)_{im}$ because it is no longer valid for describing the dissipated energy release rate.

3.6.1.5 Number of loading cycles

The results presented in Fig.3.7 are limited to three loading cycles. Looking back at Eq.(3.46), it is clear that more cycles leads to more terms in the sum representing the temporal integral for t'_s ranging from 0 to t_k . One could argue that this is a limitation of the numerical method since the number of terms to compute increases quadratically with the number of time steps. However, the term $j(t_k - t'_s)$ inside the sum decreases exponentially as $t_k - t'_s \rightarrow \infty$ (see Eq.(3.19)). Therefore, it is possible to compute the sum with reasonable accuracy without considering all the terms. This is why our numerical method will always outperform a finite element simulation for any number of cycles. In Appendix F, we provide a comparison of the computational time required to solve Eq.(3.39) with our numerical method versus the finite element simulation in ABAQUS.

3.6.2 Fatigue fracture behavior

In the literature, fatigue fracture is characterized by the dependence of crack extension loading cycle dc/dN on the maximum energy release rate G_{max} in a loading cycle. Here we use our theory to predict the $dc/dN-G_{max}$ behavior and the effects of material parameters and loading conditions on this relationship. It should be emphasized that we have adopted a simplistic linear viscoelastic model in our theory, whereas in practice elastomers exhibit more complex constitutive behaviors

such as reinforcement by fillers [69], strain induced crystallisation [81, 117, 21, 44] or large strains near the crack tip [101], all of which may be relevant to fully explain the experimental results of fatigue fracture. Therefore, comparison with experimental data should be limited to materials that can be well represented by viscoelasticity. A class of materials suitable for this purpose is the unfilled and non-crystallizing elastomers, e.g., unfilled styrene-butadiene rubber (SBR). In addition, realistic viscoelastic materials often exhibit a spectrum of relaxation times rather than a single one as assumed in our theory, which needs to be characterized experimentally and then accounted for through the creep function $J(t)$. Although there are experimental works reporting the fatigue data of unfilled SBR [71, 82, 101, 64], they lack sufficient information for determining the viscoelastic behavior or Γ_0 , thus making quantitative comparison difficult. Due to simplistic nature of our material model, we focus on the qualitative trends when making connections with experimental data.

3.6.2.1 Regimes

To study the fatigue behavior, we imposed a cyclic stress intensity factor $K(t)$ such that $G(t) = K^2(t)/E_\infty$ varies in the interval $[0, G_{max}]$ for 40 cycles, and solved for the crack length $c(t)$ using the numerical procedure described in Section 3.5. We repeated this procedure for increasing G_{max} and recorded the corresponding dc/dN , as shown in Fig.(3.8a). Note that we used the normalization G_{max}/Γ_0 and $\bar{c} = c/l$ and plotted the data on a logarithmic scale.

In Fig.(3.8a), we reported results for $d\bar{c}/dN$ based on different definitions according to how it is averaged from multiple loading cycles:

$$\frac{d\bar{c}}{dN} = \bar{c}(T) - \bar{c}(0) \text{ (FC)}, \quad (3.56)$$

$$\frac{d\bar{c}}{dN} = \frac{\bar{c}(5T) - \bar{c}(0)}{5} \text{ (F5C)}, \quad (3.57)$$

$$\frac{d\bar{c}}{dN} = \frac{\bar{c}(40T) - \bar{c}(0)}{40} \text{ (AC)}, \quad (3.58)$$

$$\frac{d\bar{c}}{dN} = \frac{\bar{c}(40T) - \bar{c}(T)}{39} \text{ (ABFC)}, \quad (3.59)$$

$$\frac{d\bar{c}}{dN} = \bar{c}(nT) - \bar{c}((n-1)T), \forall n \in [2, 39] \text{ (SC)}, \quad (3.60)$$

where “FC”, “F5C”, “AC”, “ABFC”, and “SC” stand for first cycle, first 5 cycles, all cycles, all but the first cycles, and subsequent cycles, respectively. All definitions converge for lower values of G_{max}/Γ_0 . Notably, for $G_{max}/\Gamma_0 \rightarrow 1$ the crack extension per cycle quickly goes to zero and we observe an asymptotic branch to the left. As G_{max}/Γ_0 is increased, these definitions start to deviate from each other. Based on this observation, we divide the range of G_{max}/Γ_0 into two regimes: regime (i) where the various definitions of $d\bar{c}/dN$ agree, and regime (ii) where they give different results.

The discrepancy in regime (ii) is due to the first cycle. If we were to consider more and more cycles, all curves would converge to the SC curve (see difference between the F5C and AC curves). This can be seen from Figs.(3.8c-d) where we consider two values $G_{max}/\Gamma_0 = 10^{1.5}$ and $G_{max}/\Gamma_0 = 10^2$ in regime (ii). We observe a clear transition in the behavior of $\bar{c}(t)$. The extension within the first cycle dramatically increases while subsequent cycles (SC) remain similar. For this reason, the FC curve in Fig.(3.8a) features an inflection (see the slope on Fig.(3.8b)), while the SC curve does not.

We defined the boundary between regimes (i) and (ii) as the point of departure between the FC and SC curves. As G_{max} increases, dissipation occurs earlier within a cycle, so the crack starts to propagate earlier in the cycle. Eventually, for sufficiently large G_{max} , the crack starts to propagate almost at the beginning of a cycle at which the strain history is provided by the previous cycle. In the case of the first cycle, however, there is no prior history and therefore dissipation can only come from crack propagation. This is why the crack has to propagate more in the first cycle to reach the imposed dissipation. We name regime (ii) the *critical regime* because further increase in G_{max} mainly contributes to increasing crack propagation within the first cycle. Note that our theory considers an infinitely wide pure shear strip, but in practice it must be finite in width, which would lead to complete fracture of the sample within the first cycle. The exact value of G_{max} beyond which a strip with width L_s breaks within the first cycle certainly depends on L_s , but it will always happen in regime (ii).

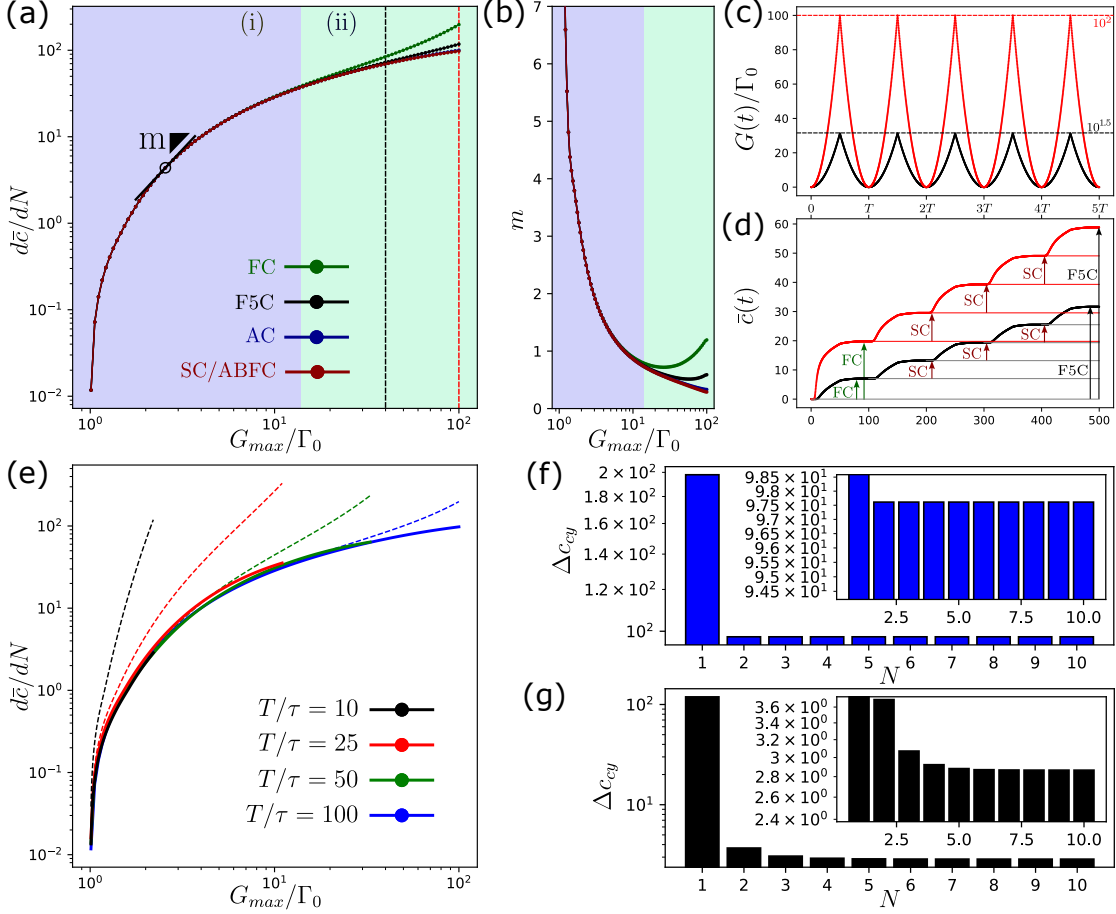


Figure 3.8: (a) Increase in crack size per cycle as a function of the maximum global energy release rate. $\bar{c} = c/l$ is the normalized crack size, N is the number of cycles and $G_{max} = G(t = T/2)$ is the maximum value of G achieved during a cycle. The plots are provided on a base 10 logarithm scale. The green plot shows crack length increase for the first cycle (FC), the black plot for the first 5 cycles (F5C), the blue plot for all 40 cycles (AC), and the red plot for all but the first cycle (ABFC) or any of the subsequent cycles (SC). (b) The slope m of the curves in (a). The departure of the FC from the SC curve defines the initial regime (i) and the critical regime (ii). (c) For two given values $G_{max}/\Gamma_0 = 10^{1.5}$ and $G_{max}/\Gamma_0 = 10^2$ in regime (ii), the value of $G(t)/\Gamma_0$ is provided. (d) The resulting $\bar{c}(t) = c(t)/l$ is plotted and we highlighted the increase per cycle for FC, F5C and SC. (e) The dotted lines correspond to the FC curves while the plain lines are the SC curves, for each value of T/τ . (f) $\Delta c_{xy} = \bar{c}(NT) - \bar{c}((N-1)T)$ is the increase in normalized crack length per cycle N . The data is provided for $T/\tau = 100$ and $G_{max}/\Gamma_0 = 10^2$, corresponding to the last point of the blue plot on (e). (g) Similar to (f), but for $T/\tau = 10$ and $G_{max}/\Gamma_0 = 2.2$ (last point of the black plot on (e)).

In the initial regime (i), we find that the slope m of the $dc/dN - G_{max}$ curve on the log-log plot decreases steadily. Therefore, our result does not feature a distinct Paris regime with a constant m as observed experimentally [71, 69], suggesting that linear viscoelasticity with a single relaxation time is insufficient to capture the Paris regime. However, analyses based on the solutions for steady-state crack growth under static loading imply a Paris regime with an exponent set by the viscoelastic properties [107, 15]. This difference may be attributed to the dynamic effect discussed in Section 3.6.3.

The data in Fig.(3.8a) were obtained for $T/\tau = 100$, such that in the far field, the material behaves elastically with modulus E_∞ . Fig.(3.8e) highlights the transition from regime (i) to (ii) for decreasing values of T/τ . When the frequency of cyclic loading is increased, the critical regime starts at lower G_{max} and the difference between the FC and SC curves is amplified. In addition, we observe the amount of propagation within each cycle takes a few more cycles to settle (see Fig.(3.8f)) for $T/\tau = 100$ compared to Fig.(3.8g) for $T/\tau = 10$. It is worth mentioning that our theory was developed based on the *quasi-steady-state* condition, i.e., the crack extension for each cycle is the same. Although a few cycles are needed for our numerical solution to settle at a constant value, this value should be interpreted as the steady dc/dN reported in the experimental literature, which may take a large number of loading cycles to achieve.

3.6.2.2 Influence of material parameters on the $dc/dN - G_{max}$ behavior

We studied the influence of material properties, namely E_0/E_∞ and T/τ , on the fatigue behavior. Fig.(3.9a) shows that increasing E_0/E_∞ promotes fatigue life. In a linear viscoelastic pure shear strip under static loading, the viscoelastic trumpet model [20, 118] establishes that a viscous region, where most of the energy dissipation occurs, occupies a region $V\tau < ||\mathbf{X}_c|| < V\tau_c$. At constant V and τ , increasing $\tau_c = \tau E_0/E_\infty$ increases the size of the viscous region at the expense of the soft elastic behavior. Under static loading, a material with higher ratio E_0/E_∞ needs to be stretched more to propagate a crack at V , since it is more dissipative. Under cyclic loading, the speed is not constant. However, Fig.(3.9a) shows, if E_0/E_∞ is increased, it also requires a larger

energy input G_{max}/Γ_0 to obtain the same crack extension per cycle $d\bar{c}/dN$, which is qualitatively similar to static loading. Fig(3.9b) shows that the relationship between $d\bar{c}/dN$ and G_{max}/Γ_0 is insensitive to the ratio T/τ within the range of T/τ considered in our numerical solutions. In Appendix G, we provide this result for three additional values of the ratio E_0/E_∞ and confirm that this observation holds.

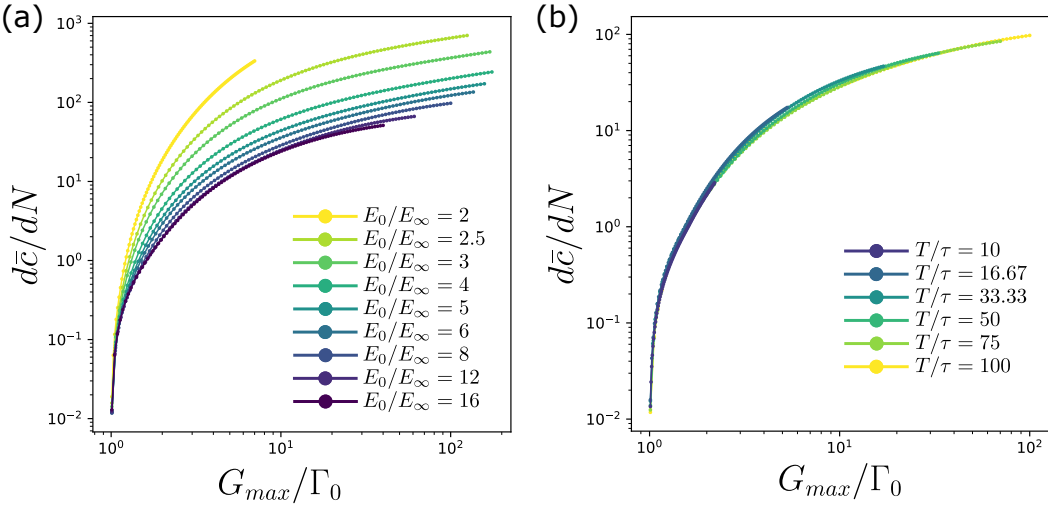


Figure 3.9: (a) Increase in normalized crack length $\bar{c} = c/l$ per cycle N with normalized maximum global energy release rate G_{max}/Γ_0 , for varying E_0/E_∞ and fixed $T/\tau = 100$. (b) Same data for varying T/τ and fixed $E_0/E_\infty = 8$.

3.6.3 Dynamic effect

Lake and Lindley [71] experimentally compared the crack extension obtained under cyclic loading to the crack extension resulting from *equivalent static loading*. They showed cracks propagate faster under cyclic loading at high frequency, which is known as the “dynamic” effect. Here “dynamic” refers to cyclic loading as opposed to static loading, and does not imply any inertial effects. In this section, we show that our theory is qualitatively consistent with their observation.

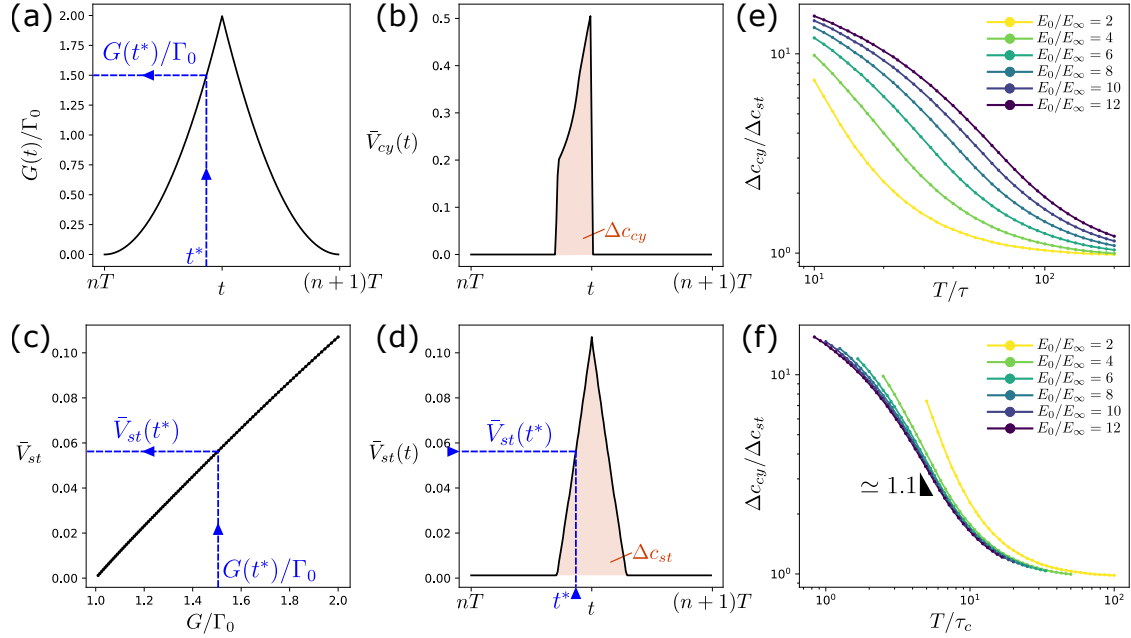


Figure 3.10: (a) History of $G(t)/\Gamma_0$ within a loading cycle. For a given time, the value $G(t^*)$ is recorded and reported on plot (c). (b) Corresponding crack speed within the cycle, solved using the numerical method in Section 3.5. The area under the curve is the crack extension per cycle under cyclic loading Δc_{cy} . (c) For static loading with energy release rate G/Γ_0 , the constant crack speed \bar{V}_{st} is predicted (Section 3.5). This result is used to predict the crack speed $\bar{V}_{st}(t^*)$ at a given time t^* corresponding to the value $G(t^*)$. It allows one to obtain (d) from (a). (d) At all times within a cycle, the static loading equivalent for the crack speed \bar{V}_{st} is obtained by considering the operating $G(t)$ and using (c). The area under the curve is the crack extension per cycle under equivalent static loading Δc_{st} . (e) The ratio $\Delta c_{cy}/\Delta c_{st}$ is a measure of the dynamic effect due to cyclic loading at period T . It is plotted for 200 values of T/τ , with τ being constant (i.e., the same material). Results are provided for increasing values of E_0/E_∞ . (f) The curves on (d) can be partially collapsed by plotting against T/τ_c , with $\tau_c = E_0/E_\infty \tau$.

For a loading cycle where dc/dN has settled to a steady value, the crack extension in this cycle may be obtained from the crack speed as

$$\Delta c_{cy} = \int_{nT}^{(n+1)T} V(t) dt, \quad (3.61)$$

with n being an integer. To get the extension under *equivalent static loading*, Lake and Lindley [71] first measured the crack speed under static loading with a range of global energy release rates. The numerical method developed in Section 3.5 allows us to obtain such a relationship. We simply set a constant $G(t)$ for a period of time and use our method to solve for $V(t)$, which yields a constant speed as expected for static loading. We repeated this for values of G corresponding to the range under cyclic loading and recorded the $V - G$ relationship, as shown in Fig.(3.10b).

Similarly to Lake and Lindley [71], we considered the operating energy release rate $G(t^*)$ at a given time t^* (see Fig.(3.10a)). Under static loading at $G(t^*)$, the result in Fig.(3.10c) yields a constant crack speed \bar{V}_{st} . At time t^* , the equivalent static crack speed is therefore $\bar{V}_{st}(t^*)$, as reported in Fig.(3.10d). We repeated this for all time steps within a loading cycle to obtain the full equivalent static crack speed (Fig.(3.10d)), which is then compared to the cyclic crack speed obtained from the procedure described in Section 3.5 (Fig.(3.10b)).

The areas under the curves of Fig.(3.10b) and Fig.(3.10d) correspond to the crack extension per cycle under cyclic loading Δc_{cy} and equivalent static loading Δc_{st} , respectively. We calculated the ratio $\Delta c_{cy}/\Delta c_{st}$ for a given material (characterized by τ and E_0/E_∞), under increasing cycle period T . Results for selected materials with varying E_0/E_∞ are provided as Fig.(3.10e). Clearly, a decrease in the cycle period T relative to the relaxation time τ , results in an amplification of the ratio $\Delta c_{cy}/\Delta c_{st}$: the larger the loading frequency, the higher the ratio. At low loading frequencies ($T/\tau > 10^2$), the ratio goes to $\Delta c_{cy}/\Delta c_{st} \rightarrow 1$, indicating that cyclic loading is no more detrimental than static loading and the crack extension Δc_{cy} can indeed be estimated from the *equivalent static loading*. However, for $T/\tau \sim 10$, we find an amplification ratio of crack extension ~ 10 -fold under cyclic loading. This is in qualitative agreement with the results of Lake and Lindley [71], which showed that Δc_{st} is approximately equal to Δc_{cy} at low loading frequencies (i.e., 0.1 to 1 cycle per minute) but can be less than 3% of Δc_{cy} at high loading frequencies (i.e., up to 10^3 cycle per minute).

Additionally, we notice that decreasing the ratio E_0/E_∞ makes this amplification happen at higher loading frequency (Fig.(3.10e)). By plotting the data according to T/τ_c instead, with

$\tau_c = \tau E_0 / E_\infty$, we show that we can collapse the data (Fig.(3.10f)). This highlights the relevance of the comparison between the timescale for material relaxation τ_c and the cycle period T to characterize the dynamic effect.

3.6.4 Influence of the polarization

Polarization in the cyclic loading, often measured by the loading ratio, has been shown to affect fatigue fracture in elastomers. The loading ratio can be defined as:

$$p = \frac{G_{min}}{G_{max}} \quad (3.62)$$

Fig.(3.11a) shows its influence on the fatigue behavior. For lower values of G_{max} , increasing p results in shorter fatigue life. On the contrary, at larger G_{max} , fatigue life is improved upon increasing p . Note that results in Fig.(3.11a) is for $T/\tau = 100$. Numerical solutions for $T/\tau \in [50, 60, 75]$ exhibit similar trends. While strain-induced crystallization has been experimentally shown to be a major contributor to the improvement of fatigue life under polarized loading, studies have also shown that non-crystallizing elastomers exhibit the same behavior [82, 125, 121], though with different magnitude (and physical origin) as elaborated below.

Lindley [82] reported a nearly 20-fold reduction in the crack extension per cycle, dc/dN , for unfilled SBR when p is increased from 0 to 1. Similar effect was also found by Stadlbauer *et al* [125] and Schieppati *et al* [121] for filled SBR or other non-crystallizing rubbers. Note in both studies [125, 121] the authors define the loading ratio as $\tilde{p} = \epsilon_{min}/\epsilon_{max}$ according to the tensile strain in the far field. Based on Eq.(3.38), we set $p = \tilde{p}^2$ to enable comparison between our result and these experimental studies. Upon increasing p from 0 to 0.25 at $G_{max} \sim 10^3 J/m^2$, Stadlbauer *et al* [125] reported a relative decrease in dc/dN that is $\sim 50\%$ for a SBR and $\sim 70\%$ for a 50/50 mix of butadiene rubber (BR) and SBR (both rubbers were filled with 50phr carbon black, where phr stands for parts per hundred parts rubber). At the same value of G_{max} , Schieppati *et al* [121] studied a non-crystallizing acrylonitrile butadiene rubber (NBR) with 42phr carbon black filler and reported a relative decrease in dc/dN that is $\sim 50\%$ when p is increased from 0 to 0.25. The range

of relative decrease in $d\bar{c}/dN$ (i.e., $\sim 50\%$ to $\sim 70\%$ when p is increased from 0 to 0.25) is consistent with the data in Lindley [82] for unfilled SBR.

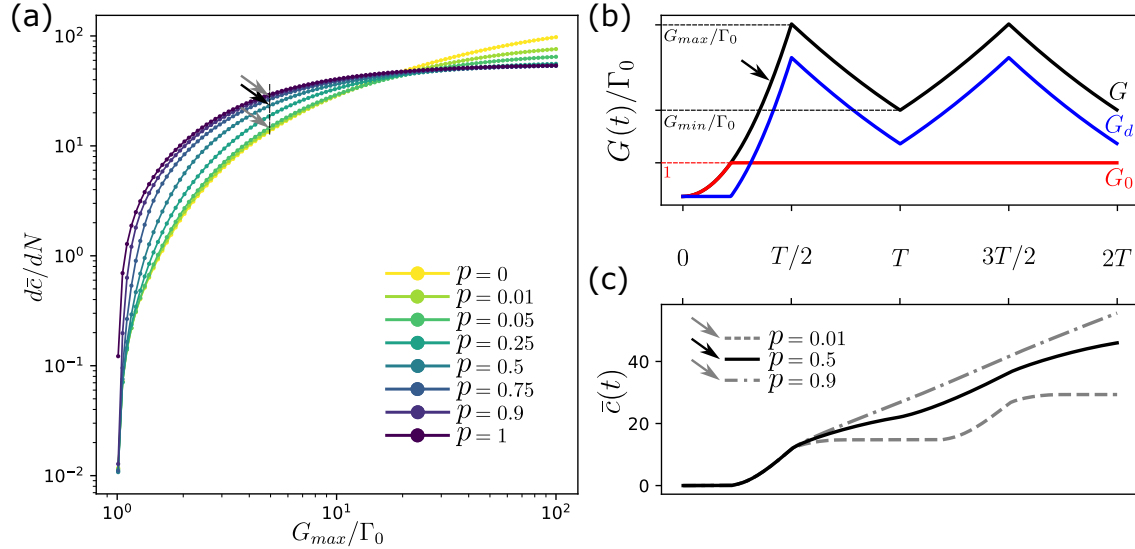


Figure 3.11: (a) Crack extension per cycle versus the maximum global energy release rate for different polarization values p (with $T/\tau = 100$ and $E_0/E_\infty = 8$ kept constant). (b) History of the energy release rates in two loading cycles for $p = 0.5$ (black arrow on (a)). The first cycle starts with $G(0) = 0$ but is unloaded only up to $G_{min} = pG_{max}$. The subsequent cycles start from and end at G_{min} . (c) The resulting normalized crack extension \bar{c} . Data is given for the points on (a) indicated by the arrows. Note only the extension in the second cycle is accounted for to define $d\bar{c}/dN$ on (a).

To compare our theory with these experimental findings, we need to know the value of Γ_0 which was not reported. However, Lake and Thomas [73] suggested that Γ_0 is on the order of $10-100 J/m^2$ for typical rubbers. Therefore, the observation of Stadlbauer *et al* [125] and Schieppati *et al* [121] corresponds to $G_{max}/\Gamma_0 \sim 10 - 100$ from $p = 0$ to $p = 0.25$. On our Fig.(3.11a), this range of G_{max}/Γ_0 covers both regions where increasing p may either increase or reduce $d\bar{c}/dN$. As a result, it is not conclusive whether our theory can capture experimental trends of the polarization effect. Note that it has been hypothesized the improvement of fatigue life under polarized loading

should be attributed to the polymer-fillers interaction [125, 28], which is not accounted for in our theory.

3.7 Conclusion

In summary, this chapter presents a theory to predict crack extension in linear viscoelastic solids under cyclic loading. Our theory is built upon a general thermodynamic framework for crack propagation in homogeneous solids, which is applicable to arbitrary crack geometry, external loading conditions and material behaviors (i.e., elastic or inelastic). Based on this framework, we derive a fracture criterion which allows us to solve for the rate of crack propagation based on the stress and strain fields. To demonstrate our theory, we choose the pure shear configuration, for which our theory results in an integral equation relating the energy release rate to the crack extension during cyclic loading. In comparison to the scaling theory of Guo *et al.*[49], our theory rigorously accounts for the multi-axial nature of the stress field around the crack. Additionally, we develop numerical methods to solve for the crack extension per loading cycle. The theory has been validated through a comparison with finite element simulations. We show that our framework allows for the study of material parameters and polarization influence on the fatigue fracture behavior. It also qualitatively captures the dynamic effect observed by Lake and Lindley [71].

A series of assumptions have been made in our theory, as summarized below.

- We have assumed that the quasi-static and isothermal conditions are satisfied to obtain Eq.(5.5) (Section 3.2.1).
- For the fracture criterion in Eq.(4.9) to be valid, we have assumed a planar crack undergoing self-similar propagation and a constant toughness Γ_0 (Section 3.2.2).
- To implement Eq.(4.9), we need to know the stress and strain fields for crack propagation in viscoelastic solids. One way of obtaining these fields is to use the extended correspondence principle to leverage existing elastic solutions, which requires the following three assumptions (Section 3.3).

- ◊ The material is linearly viscoelastic. Specifically, we adopted the standard linear solid model for demonstration purpose.
- ◊ The crack can only propagate (i.e., no crack closure).
- ◊ The stress intensity factor K is independent of material properties, which is satisfied by either imposing traction boundary conditions or imposing displacement boundary conditions with a fully relaxed far field.
- When specifying our theory to the pure shear configuration, we have assumed the following conditions to arrive at Eq.(3.39) (Section 3.4.1).
 - ◊ The plane stress condition applies.
 - ◊ The extended correspondence principle is valid. Given the displacement boundary condition for the pure shear configuration, the far field needs to be fully relaxed, which requires the cyclic loading to be slow relative to the viscoelastic relaxation time (i.e., *slow loading*).
 - ◊ The *quasi-steady-state* condition is satisfied, i.e., the crack extension per cycle has reached a constant and each loading cycle induces the same changes to the strain field.
- Lastly, when solving Eq.(3.39), a cutoff length l is assumed to avoid singularity of the K -field at the crack tip.

Several assumptions listed above can be relaxed to expand the range of applicability of our theory. First, while we have limited the numerical results to the standard linear solid model with a single relaxation time, extension to other viscoelastic models with broad relaxation spectrum is possible. This can be achieved by replacing the creep compliance function $J(t)$ with a more realistic one. Second, the assumption of relaxed far field for the pure shear configuration requires the *slow loading* condition. Fast loading where cycle period T is comparable to or less than τ will lead to an unrelaxed far field, which may invalidate the extended correspondence principle unless traction boundary conditions are imposed in the far field. Therefore, extension to fast loading should target configurations with traction boundary conditions. Third, as discussed in Section

3.4.5, for certain configurations (e.g., single edge notch), the stress intensity factor K depends on crack length and hence the *quasi-steady-state* assumption may not be strictly satisfied. In this case, one can neglect the change in K over a few loading cycles and approximately impose the *quasi-steady-state* assumption. Finally, we have argued that the stress singularity at the crack tip must be regularized by a cohesive zone, but have neglected the contribution due to the stress field immediately surrounding the cohesive zone by introducing a constant cutoff length l to the K -field. Extension is possible by leveraging the stress field solutions that bridge the cohesive zone (e.g., the Dugdale-Barenblatt model) and the K -field [57].

More broadly, crack propagation under cyclic loading is a fundamental problem underlying the fatigue fracture. While viscoelasticity captures the dominant behavior of unfilled and non-crystallizing elastomers, consideration of more complex behaviors (e.g., the Mullins effect [24] and the strain-induced crystallization [32]) is valuable for obtaining a complete theoretical picture on the fatigue fracture of filled elastomers. Here the challenge lies in the lack of sufficient understanding on the stress and strain fields during cyclic crack growth, thereby calling for computational and experimental efforts in the future. Additional damage mechanisms near the crack tip such as cavitation [149] may also need to be considered for filled elastomers.

Chapter 4

Fracture toughness of soft solids with Mullins effect

The work presented in this chapter was a collaboration with my advisor Rong Long and will be published as a research paper soon.

4.1 Introduction

Soft polymeric materials are widely utilized in applications where reversible large deformation is desired. Examples include tires [92], adhesives [18, 142], soft robotics [140], actuators [77], stretchable electronics [60, 61], and biomedical implants [144]. The ability of a soft material to sustain deformation and resist failure is a key material property for many of these applications. Mechanical failure often occurs through the growth of small cracks that amplify the local stress in their vicinity. Therefore, fracture tests that measure the critical loads needed to grow a pre-existing sharp crack have been adopted to characterize the toughness of solids. The interpretation of the fracture tests is built upon fundamental concepts established in fracture mechanics [147]. For example, the criterion for crack growth can be posed either using the amplitude of the crack-tip stress field (i.e., the stress intensity factor) or following an energetic analysis [147]. For soft materials, the nonlinearity due to large deformation renders the stress field solution based on linear elasticity invalid and hence prevents the application of stress intensity factors [84]. However, the energetic analysis is still applicable and has been adopted for interpreting the fracture tests of soft rubbers and gels [114, 85]. Specifically, during crack propagation, the decrease in the potential energy if the crack grows by a unit area is defined as the energy release rate G . The critical value

of G required to drive crack growth in a material is the fracture toughness Γ .

Several experimental configurations have been developed to measure Γ for soft materials [114, 85]. Ideally, Γ should be independent of the conditions of fracture tests, otherwise it may not be regarded as a material property. While this requirement can be satisfied for materials that are pre-dominantly elastic [114, 116], the interpretation of Γ is more complicated for inelastic materials [85]. In this case, although G can still be formally defined as the potential energy released per unit area of crack propagation, the released energy is not only consumed by the fracture processes at the crack tip, but also dissipated in the bulk material surrounding the crack tip [18, 85]. The dissipative component of G may depend on the conditions of fracture tests such as loading history and sample dimensions. In addition, the formation of a damage zone around the crack tip can affect the stability of crack growth and further complicates the data interpretation of fracture tests. For example, the measurement of Γ using the pure-shear configuration [114, 85] requires one to identify the critical global stretch λ_c for crack growth. If the underlying material is perfectly elastic, crack growth in the pure-shear configuration becomes unstable immediately after the onset, leading to a sudden drop in the applied force. This feature allows one to identify λ_c directly from the force-displacement curve. However, if the material is inelastic, crack growth in the pure-shear configuration can remain stable after the onset [85, 150], making it less obvious to detect the onset of crack growth. In some soft materials with strong dissipation such as filled rubber [3] or tough hydrogel with sacrificial network [150], no sudden drop in force may be observed from the force-displacement curve, which may result in ambiguities in how to determine λ_c .

Although energy dissipation poses complications to the interpretation of fracture tests, it has been utilized as a highly effective strategy to enhance the fracture toughness of soft polymeric materials [40, 39, 127, 128, 27, 153]. Mechanistic understandings on how energy dissipation affects crack growth are important for establishing reliable experimental methods to characterize the enhanced toughness, which is the motivation of this work. In particular, we focus on a class of inelastic soft materials that exhibit strain-induced softening known as the Mullins effect [99]. This phenomenon has been widely observed in filled rubber [99, 24] and is also found in multi-network hydrogels

[139] or elastomers [27, 97]. The Mullins softening induces hysteresis in a loading-unloading cycle, and therefore enables energy dissipation around a propagating crack [85]. Theoretical analyses on how Mullins dissipation can enhance fracture toughness have been developed in the literature [150, 10, 131, 110]. These works are based on the assumption of steady state crack growth where the stress and strain fields are translationally invariant relative to the moving crack tip [85, 110]. However, in a fracture test, the crack starts from being stationary and needs to undergo a transition stage before the steady state can be attained. There is still a lack of understanding on the transition stage of crack growth in soft materials with Mullins dissipation.

Here we present a computational study to elucidate the mechanics of crack growth in soft materials with Mullins effect. Specifically, we adopt the pure shear configuration and use the finite element method to simulate crack growth. The fracture processes occurring at the crack tip are represented by a cohesive zone model [58], whereas the Mullins effect is captured by a phenomenological model [103]. The simulation results allow us to examine different stages of crack growth, i.e., initiation, transition and steady state; and the role of sample dimensions. This chapter is organized as follows. We first summarize the main components of our model in Section 4.2 and the settings for finite element simulations in Section 4.3. Simulation results and the associated discussions are presented in Section 4.4, followed by conclusions in Section 4.5.

4.2 Model

4.2.1 Material model

The softening behavior associated with the Mullins effect is captured using a modified version of the Ogden-Roxburgh model [103]. Specifically, the Helmholtz free energy density ψ can be written as:

$$\psi = \eta W(\mathbf{F}), \quad (4.1)$$

where $W(\mathbf{F})$ is the nominal strain energy density for initial loading, \mathbf{F} is the deformation gradient tensor, and η ($0 \leq \eta \leq 1$) is the damage variable quantifying the extent of softening. We assume

the soft material to follow the incompressible neo-Hookean model upon initial loading, which yields the following form of $W(\mathbf{F})$:

$$W(\mathbf{F}) = \frac{\mu}{2}(\lambda_i \lambda_i - 3), \quad (4.2)$$

where λ_i ($i = 1, 2, 3$) are the principal stretch ratios (i.e., λ_i^2 are the eigenvalues of $\mathbf{F}^T \mathbf{F}$) and μ is the shear modulus at infinitesimal strain during initial loading.

The damage variable η can be considered as an internal variable that evolves with the deformation \mathbf{F} . Specifically, the evolution of η is prescribed as a function of $W(\mathbf{F})$ [150, 110]:

$$\eta = 1 - \frac{1}{1+r} \operatorname{erf}\left(\frac{W_{max} - W}{m + \beta W_{max}}\right), \quad (4.3)$$

where $\operatorname{erf}(x)$ is the error function, and r, m, β are material parameters controlling the softening behavior and the loading-unloading hysteresis. The value of W_{max} is given by the maximum value of $W(\mathbf{F})$ experienced by a material point throughout its deformation history. Therefore, η is equal to 1 during the initial loading and decreases towards 0 upon unloading. Note that the original Ogden-Roxburgh model [103] is a pseudo-elastic one where an additional damage function is included in the free energy density ψ to ensure $\partial\psi/\partial\eta = 0$ [150, 103]. This treatment is not adopted in Eq.(4.1) so that we can formally define the dissipation power density [55], as shown below.

The first Piola-Kirchhoff stress tensor \mathbf{P} is given by [110]

$$\mathbf{P} = \eta \frac{\partial W}{\partial \mathbf{F}} - p \mathbf{F}^{-T}, \quad (4.4)$$

where p is a Lagrange multiplier due to the incompressibility constraint that $\det(\mathbf{F}) = 1$. It is derived in Qi *et al* [110] that the dissipation power density D (i.e., the rate of energy dissipation per unit reference volume) under the isothermal condition is given by

$$D = \mathbf{P} : \frac{d\mathbf{F}}{dt} - \frac{d\psi}{dt} = -\frac{\partial\psi}{\partial\eta} \frac{d\eta}{dt} = -W \frac{d\eta}{dt}, \quad (4.5)$$

where we have applied the identity $\mathbf{F}^{-T} : d\mathbf{F}/dt = 0$ due to the constraint that $\det(\mathbf{F}) = 1$. The Clausius-Duhem inequality under the isothermal condition dictates that $D \geq 0$, which is satisfied only if $d\eta/dt \leq 0$ according to Eq.(4.5). This implies that the damage evolution law in Eq.(4.3) is

consistent with the second law of thermodynamics only for a single loading-unloading cycle [110]. Reloading (i.e., $dW/dt > 0$ while $W \leq W_{max}$) would result in $d\eta/dt > 0$ and hence a negative D . Despite this limitation, we still adopt Eq.(4.3) due to two reasons. First, we only consider the case of crack growth under monotonic loading so that all material points in the pure-shear configuration undergo only one loading-unloading cycle. Second, the material model with Eq.(4.3) is already built in the finite element software ABAQUS (version 2020, Simulia, Providence, RI, USA). For more complex loading histories (e.g., cyclic loading), alternative damage evolution models [138, 152, 76] should be used to ensure $D \geq 0$.

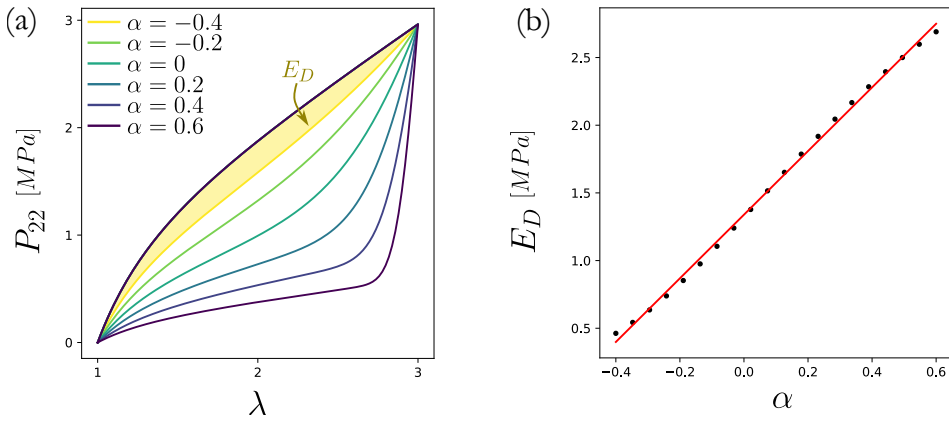


Figure 4.1: (a) Tensile stress P_{22} for different values of α . (b) Energy density dissipated within a cycle of loading-unloading for different values of α . The red line is the linear fit with determination coefficient 0.997.

There are four material parameters in the constitutive relation: μ , r , m and β . Among them, μ does not affect the crack growth process, but simply sets the scale of the applied force. In this work we are not interested in studying the individual effect of each Mullins parameter independently. Instead we wish to find a single parameter α that can be varied to produce more dissipation. Using a particular choice of Mullins parameters $\mathcal{M}_0 = [r_0, m_0, \beta_0]$ as a reference, we write $\mathcal{M} = 10^{-\alpha}\mathcal{M}_0$. From Eq.(4.3), it is clear that increasing α increases dissipation upon unloading. Let us consider a volume dV under pure shear extension with stretch ratios $\lambda_1 = 1$, $\lambda_2 = \lambda$ and $\lambda_3 = 1/\lambda$. On

Fig.(4.1), we plotted the tensile component of the stress $P_{22} = \eta\partial W/\partial\lambda - \mu/\lambda^2$ for $\alpha \in [-0.4, 0.6]$ with $\mathbf{M}_0 = [1, 0.5, 0.1]$ and $\lambda_{max} = 3$. By integrating the area between the loading and unloading curves, corresponding to the dissipated energy density E_D , we find that E_D increases linearly with coefficient α over the range of values considered. In the following, we use this unique parameter to control the amount of dissipation from damage, instead of the $[r, m, \beta]$ parameters independently.

4.2.2 Pure shear fracture test

Thin sheet samples with a strip geometry are used in a pure shear fracture test, as illustrated in Fig.(4.2). The sample width L is much larger than its height $2H$ (i.e., $L \gg 2H$). The out-of-plane thickness w is much smaller than the in-plane dimensions (i.e., $w \ll H$). An initial crack with length c_0 is introduced at the mid-height of the ledge edge of the sample. The sample is then mounted between two rigid grips, which are both separated by a prescribed displacement $\Delta(t)$. The displacement loading can also be expressed in terms of the nominal global stretch $\lambda(t) = \Delta(t)/H$. We consider monotonous loading with a constant stretch rate $\dot{\Delta}$ or $\dot{\lambda} = \dot{\Delta}/H$. After the crack starts to grow, the crack length c becomes a function of time with the initial condition that $c(t=0) = c_0$. We denote \mathbf{X} as the position of a material point in the reference configuration with respect to a fixed Cartesian coordinate system e_X, e_Y as depicted in Fig.(4.2). We also define a moving coordinate system attached to the crack tip and denote \mathbf{X}_c the position of this same material point in this moving frame.

4.2.3 Power budget

In chapter 3, we proposed a general thermodynamic framework for crack propagation in homogeneous solids, which is applicable to the problem at hand. In particular, we showed that, under quasi-static crack propagation and the assumption of constant Γ_0 along the crack front, the global free energy imbalance may be written as,

$$\int \mathbf{P} : \frac{d\mathbf{F}}{dt} dS = \int \mathbf{t} \cdot \frac{d\mathbf{u}}{dt} dl - \Gamma_0 \frac{dc}{dt}, \quad (4.6)$$

where \mathbf{t} and \mathbf{u} are the traction and displacement vectors in the reference configuration.

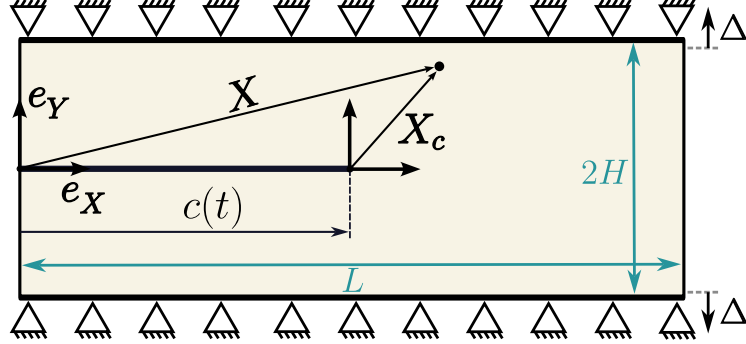


Figure 4.2: Pure shear fracture test with a thin-sheet strip sample geometry (i.e., $L \gg 2H$).

The top and bottom boundaries of the sample are fixed to two rigid grips that are separated by a displacement loading.

In Eq.(4.6), the volumetric integral throughout the solid has been replaced by an integral over the area dS due to the plane stress assumption for the pure shear configuration. Correspondingly, the power of external forces is therefore expressed as an integral over the boundary contour with line element dl . In chapter 3, assuming that the crack advances in a self-similar manner, we wrote the displacement and strain fields as functions of material point coordinates, crack area and time alone. Here, because we are considering rate-independent damage and monotonous loading (constant $\dot{\lambda}$), we may additionally notice that the effect of time is fully captured by the evolution of λ : we have $\mathbf{u}(\mathbf{X}, c, \lambda)$ and $\mathbf{F}(\mathbf{X}, c, \lambda)$ and the following chain rule applies,

$$\frac{d\bullet}{dt} = \frac{\partial\bullet}{\partial\lambda}\Big|_c \dot{\lambda} + \frac{\partial\bullet}{\partial c}\Big|_\lambda \dot{c}. \quad (4.7)$$

We may rewrite Eq.(4.6) as,

$$\left(\int \mathbf{P} : \frac{\partial \mathbf{F}}{\partial \lambda} \Big|_c dS - \int \mathbf{t} \cdot \frac{d\mathbf{u}}{d\lambda} \Big|_c dl \right) \dot{\lambda} + \left(\int \mathbf{P} : \frac{\partial \mathbf{F}}{\partial c} \Big|_\lambda dS + \Gamma_0 \right) \dot{c} = 0 \quad (4.8)$$

Note the term involving $(\partial\mathbf{u}/\partial c)|_\lambda = 0$ was dropped because the problem involves displacement boundary conditions. The first term of this equation represents the difference between internal

and external power in the absence of crack propagation, which vanishes for quasi-static deformation. Therefore, for an actively propagating crack $\dot{c} > 0$, the second term in Eq.(4.8) also vanishes and we obtain the following fracture criterion:

$$\begin{cases} \dot{c} = 0 & \text{if } G_0 < \Gamma_0 \\ \dot{c} > 0 & \text{if } G_0 = \Gamma_0 \end{cases} \quad \text{with } G_0 = - \int \mathbf{P} : \frac{\partial \mathbf{F}}{\partial c} \Big|_{\lambda} dS. \quad (4.9)$$

We refer to G_0 as the intrinsic energy release rate and we define the global energy release rate,

$$G = - \int \frac{\partial \psi}{\partial c} \Big|_{\lambda} dS. \quad (4.10)$$

Note that, multiplying dS and c by the thickness w , and interpreting ψ as the elastic strain energy density in Eq.(4.10); we recover the classic definition of the energy release rate in linear elastic fracture mechanics, i.e. the drop in potential energy per unit area of crack growth. Additionally, we define the dissipated energy release rate,

$$G_D = - \int W \frac{\partial \eta}{\partial c} \Big|_{\lambda} dS. \quad (4.11)$$

These definitions lead to the decomposition

$$G = G_0 + G_D, \quad (4.12)$$

which, for a propagating crack $\dot{c} > 0$, is written $G = \Gamma_0 + G_D$ per Eq.(4.9). We assume that no material point experiences unloading unless the crack actively propagates. This is relevant under monotonic loading because only the concentration of stress at the crack tip together with a moving crack tip causes the material points on its way to experience a loading-unloading process. Therefore, we have $d\eta/dt = (\partial\eta/\partial c)|_{\lambda}\dot{c}$ and,

$$G_D \dot{A} = -w \int W \frac{d\eta}{dt} dS = w \int \left(\mathbf{P} : \frac{d\mathbf{F}}{dt} - \frac{d\psi}{dt} \right) = \int D dV \quad (4.13)$$

where $\dot{A} = w\dot{c}$ is the increase in crack area, with \dot{c} the crack extension speed. From Eq.(4.13), the interpretation of G_D is clear: it is the rate of energy dissipation per unit crack area.

4.2.4 Energy release rate for steady state crack propagation

As pointed out by Long and Hui [85], under steady state crack propagation at fixed stretch, the stress and strain fields are invariant in the coordinate system attached to the moving crack tip (as long as $L, c \gg H$). We may then write $\partial \bullet / \partial c = -\partial \bullet / \partial X_c$ and the steady state energy release rate \mathcal{G} becomes,

$$\begin{aligned} \mathcal{G} &= \int_{-H}^H \int_{-\infty}^{+\infty} \frac{\partial \psi}{\partial X_c} dX_c dY_c \\ &= \int_{-H}^H (\psi(X_c \rightarrow +\infty) - \psi(X_c \rightarrow -\infty)) dY_c. \end{aligned} \quad (4.14)$$

From Eq.(4.1) and the pure-shear configuration, it is clear that $\psi(X_c \rightarrow -\infty) = 0$. As noted by Rivlin and Thomas [114], for a sample where $L \gg c$, the material in the region ahead of the crack and far enough from the sample boundaries (referred to as the far field) is under a uniform *pure shear* state of deformation with principle stretches $\lambda_1 = 1$, $\lambda_2 = \lambda$ and $\lambda_3 = 1/\lambda$. We then have $\psi(X_c \rightarrow +\infty) = W_{ff}$ where,

$$W_{ff} = \frac{\mu}{2}(\lambda^2 + \lambda^{-2} - 2) \quad (4.15)$$

Note we have $\eta = 1$ in the far field as a consequence of selecting the Ogden-Roxburgh model in which damage is recorded upon unloading. The steady state energy release rate therefore becomes,

$$\mathcal{G} = 2HW_{ff}(\lambda). \quad (4.16)$$

Under monotonic loading, the stretch is not fixed and instead increases at a fixed rate. However, experimental studies typically report \mathcal{G} as an operational measure of G because, as function of the stretch λ only, it is readily accessible experimentally [3]. In the following, we discuss the relationship between the energy release rate (ERR) G defined per equation Eq.(4.10) and the operational ERR \mathcal{G} of Eq.(4.16).

4.3 Finite elements simulations

4.3.1 ABAQUS model

Our model consists of two rectangular regions of size L by H separated by a layer of cohesive elements on the projected crack path. The bulk elements are mainly of the CPS4R type with a couple CPS3 elements to accommodate mesh refinement. The largest element size is $\sim H/10$ close to the domain boundary while the smallest is $\sim H/100$ close to the crack. The cohesive elements (COH2D4 type) are introduced between the two rectangular regions over a length $L - c_0$ where c_0 represents the initial crack length. The material model for bulk elements described in Section 4.2.1 is readily available in the finite element software ABAQUS. Cohesive elements are subjected to a triangular traction-separation law, where we enforced the values of the peak stress σ and the area under the curve Γ_0 . As a consequence, the separation for which the traction drops to zero is $\delta = 2\Gamma_0/\sigma$. We kept the ratio $H/\delta > 10$ throughout the simulations. Note that the area under the traction-separation curve indeed corresponds to the intrinsic fracture toughness Γ_0 introduced in Section 4.2.3: a rigorous proof is provided by Qi *et al* in [110] (see Appendix B therein). A displacement boundary condition $\Delta = H\dot{\lambda}t$ is applied to the top and bottom nodes of the mesh to enforce a constant stretch rate. All simulations are then performed using the ABAQUS/Explicit solver.

4.3.2 Post-processing

The crack tip position $c(\lambda)$ at a given stretch is defined as the X coordinate of the centroid of the first cohesive element for which the Cauchy stress is non-zero, starting from $X = c_0$. To obtain the value of $W(\lambda)$ at the nodes of our mesh, we rewrite $W(\lambda) = \mu/2(Tr(\mathbf{C}) - 3)$: the right Cauchy-Green tensor $\mathbf{C}(\lambda)$ may be obtained from ABAQUS' logarithmic strain output defined as $\mathbf{LE} = 1/2\ln(\mathbf{C})$. The values of $\psi(\lambda)$ and $\phi(\lambda)$ at nodes are obtained from $W(\lambda)$.

For the purpose of the discussion in Section 4.4, we are interested in defining the size of a *damage zone* to measure the spread of damage in the material as the crack propagates. At stretch

λ , the energy dissipated through damage is $\Phi_S(\lambda) = \int \phi(\mathbf{X}, \lambda) dS$. The greater part of this energy is dissipated in the vicinity of the crack tip where stresses are high and material points undergo subsequent loading and unloading upon crack propagation, referred as the damage zone. To track the size of this region as the crack propagates, we first define the set of contours of $\phi(\mathbf{X}, \lambda)$ as $\mathcal{C}(\lambda) = \{\mathbf{X} \in \mathbb{R}^2 | \exists \phi_0 \in \mathbb{R}, \phi(\mathbf{X}, \lambda) = \phi_0\}$. Then, we define the damage zone \mathcal{Z} as the contour where the integral of $\phi(\mathbf{X}, \lambda)$ over the area enclosed is a portion $0 < \nu < 1$ of the total energy dissipated Φ_S , mathematically:

$$\mathcal{Z}(\lambda, \nu) = \{C \in \mathcal{C}(\lambda) | \int_C \phi(\mathbf{X}, \lambda) dS = \nu \Phi_S(\lambda)\} \quad (4.17)$$

For example, $\mathcal{Z}(\lambda, \nu = 0.5)$ encloses the area where 50% of the energy is being dissipated through damage (illustrated on Fig.(4.3a)). The size of $\mathcal{Z}(\lambda, \nu)$ is defined as,

$$S_{\mathcal{Z}}(\lambda, \nu) = \sqrt{\int_{\mathcal{Z}(\lambda, \nu)} dS} \quad (4.18)$$

To obtain \mathcal{Z} and $S_{\mathcal{Z}}$ numerically, we first define a uniform triangular mesh with element size $\sim H/100$ and interpolate the value of $\phi(\mathbf{X}, \lambda)$ over this new mesh. We then use Gauss quadrature to approximate $\Phi_e(\lambda) = \int_e \phi(\mathbf{X}, t) dS_e$ for all elements e in this mesh. At a given stretch λ , the approximations of $\Phi_e(\lambda)$ for all elements are sorted from the largest to the smallest into an array $\tilde{\Phi}_e$. We then look for the smallest index E so that,

$$\sum_{e=1}^E \tilde{\Phi}_e(\lambda) \geq \nu \Phi_S(\lambda) \quad (4.19)$$

The size of the damage zone is therefore approximated as follows, with A_e the area of all elements of the uniform mesh,

$$\tilde{S}_{\mathcal{Z}}(\lambda, \nu) = \sqrt{EA_e} \quad (4.20)$$

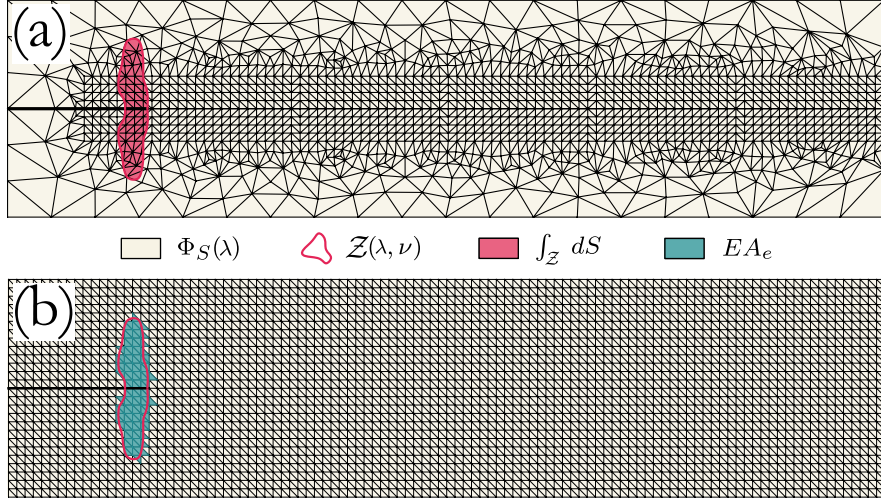


Figure 4.3: (a) Original mesh of the pure shear sample (for clarity we show a coarser mesh than that used for simulations). The damage zone defined by the contour given as Eq.4.17 is represented: it does not follow the mesh since the field ϕ is interpolated inside elements. The true area of the damage zone is colored in red. (b) A finer, uniform mesh is created and Φ_e is calculated for all its elements. Elements $\{1..E\}$ as defined per Eq.(4.19) are colored in blue. The area of the blue elements provides a numerical approximation of the area of the damage zone.

The area of the damage zone obtained numerically is illustrated on Fig.(4.3b). Note that we do not use the original mesh to compute $\tilde{S}_{\mathcal{Z}}(\lambda, \nu)$ because as the damage zone grows, the contour \mathcal{Z} overlaps with large elements: as per Eq.(4.19), the resulting value of E would include or exclude such large elements in a binary manner, thereby resulting in artificial jumps in the resulting $\tilde{S}_{\mathcal{Z}}(\lambda, \nu)$.

Finally, we report the reaction force at nodes \mathbf{df}_n for the set of top nodes at $Y = H$ in ABAQUS, from which we may define the total reaction force as $F_{eY} = \sum_n \mathbf{df}_n$.

For students interested in doing similar post-processing of ABAQUS outputs, I have created a Github tutorial [87] to save you some time.

4.4 Results

4.4.1 Shape of the resistance curve

To analyze the effect of sample geometry and material properties on the fracture behavior of our materials, we propose to pay special attention to the crack growth resistance curve, defined as $\mathcal{G}(c)$ (Fig.(4.4a)) and the force-stretch curve (Fig.(4.4b)). Note that, for metallic materials, the resistance curve is typically given in terms of the stress intensity factor (ASTM E561) or the energy release rate G (ASTM E1820) [155]. For soft solids, we use the operational ERR \mathcal{G} as defined per Eq.(4.16).

For an ideally elastic material, the resistance curve is flat, as represented in gray on Fig.(4.4a): the elastic energy stored during stretching prior to crack initiation is instantaneously released at the crack tip, propagating the crack at infinite speed throughout the sample. The crack initiation occurs at $G = \mathcal{G} = \Gamma_0$ and the force-stretch curve shows a sharp drop (Fig.(4.4b)) at the stretch λ_{init} corresponding to $\mathcal{G}(\lambda_{init}) = \Gamma_0$.

In contrast, Fig.(4.4a) shows the crack in a soft solid with Mullins effect initiates at \mathcal{G} slightly above Γ_0 and the operational ERR keeps increasing as the crack propagates. This is of course due to the dissipation occurring in the material that consumes part of the energy available to drive the crack. This effect is reflected on the force-stretch curve: because the crack no longer grows unstably, the sample continues stretching and the force keeps increasing passed the initiation point until a peak is reached, following which the force drops.

The point corresponding to the force peak has been reported on the resistance curve and we can notice that \mathcal{G} continues to increase after this point. In fact, across all the simulations we performed, we do not observe a clear steady-state where \mathcal{G} would reach a plateau value. This is because under monotonic loading, \mathcal{G} keeps increasing as long as λ is increasing (Eq.(4.15)), and therefore can only reach a plateau in the limit $\dot{c} \rightarrow \infty$. In practice, even for elastic materials, crack speeds are always finite: the instantaneous release of elastic energy is a conceptual picture which must be abandoned at speeds $\dot{c} \sim \sqrt{\mu/\rho}$ corresponding to the speed of elastic waves (a regime

where inertial terms must be accounted for).

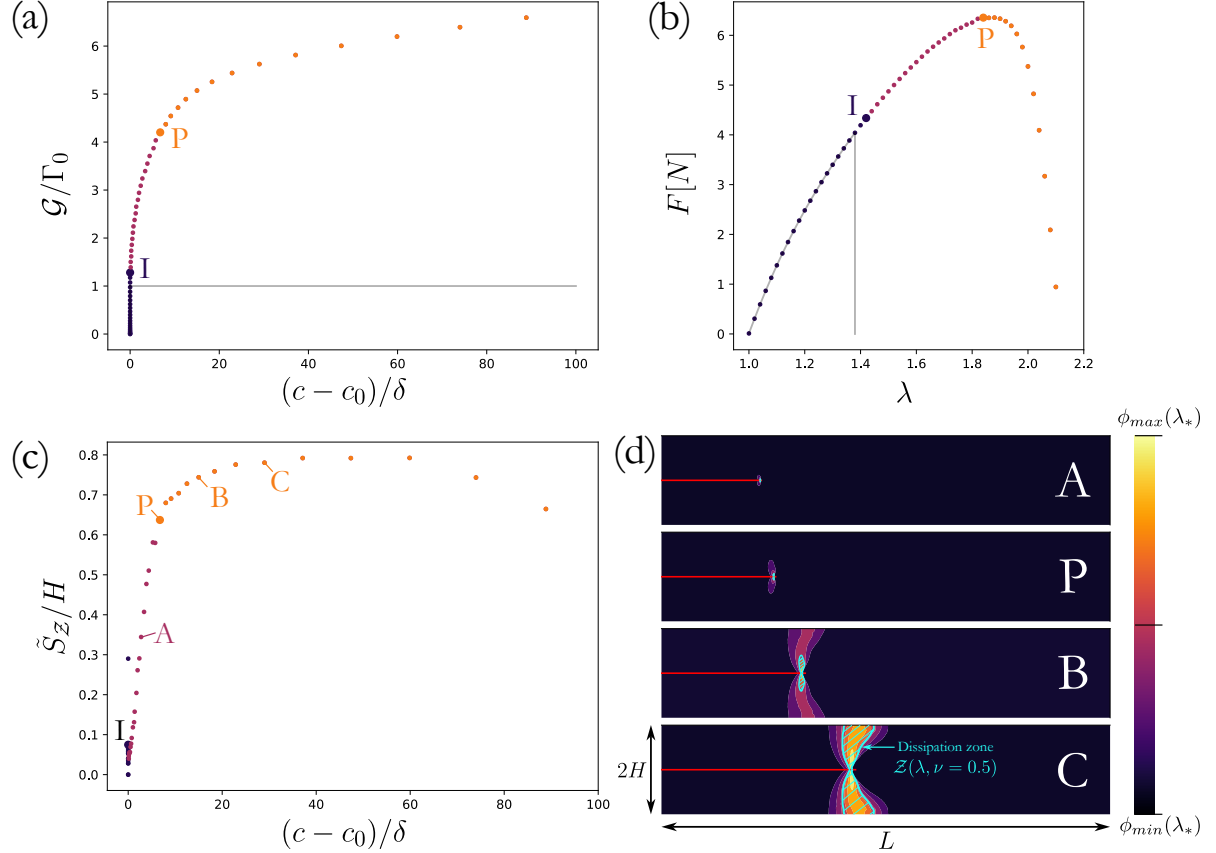


Figure 4.4: (a) Resistance curve. The operational ERR \mathcal{G} is normalized by the fracture toughness imposed through the cohesive zone model (CZM) and the increase in crack length $c - c_0$ is normalized by the maximum separation δ enforced in the CZM. The points labeled I (for initiation) and P (for peak) correspond to $c > c_0$ and $F(P) = \max(F)$ respectively. The parameters used in the simulation are listed in Table H.1 (SIM-A). The gray plot corresponds to the resistance curve of an ideally elastic material. (b) Corresponding force-stretch curves. (a) Evolution of the size of the damage zone \tilde{S}_Z (normalized by the half height of the sample) with crack extension. (d) Snapshots of the field $\phi(\mathbf{X}, \lambda)$ over the undeformed domain, for the points A, P, B and C labeled on Fig.(4.4c). For each plot, the colorbar is rescaled to the extrema of $\phi(\lambda_*)$ where λ_* is the value of stretch at that specific point. The red line represents the crack. In blue, we show the damage zone $\mathcal{Z}(\lambda, \nu = 0.5)$, growing between points A and C.

For the soft solids considered here, there is an additional effect limiting the crack speed: crack propagation is accompanied by dissipation. Because we neglected viscous effects and assumed rate independent dissipation, the crack speed is not limited by any relaxation time. However, the crack speed $\dot{c} = \lambda dc/d\lambda$ is limited by dissipation through the term $dc/d\lambda$. Indeed, a small increase $d\lambda$ can only increase the energy stored in the material by a small amount, and therefore there isn't enough energy available to be dissipated to produce a large dc . In elastic materials, a small $d\lambda$ can produce an arbitrarily large dc because increasing dc does not consume more energy than what is already available to drive crack growth.

Fig.(4.4c) shows the evolution of the size, given by Eq.(4.20), of the damage zone defined in Section 4.3.2 with crack extension. Prior to initiation $\tilde{S}_{\mathcal{Z}}$ remains small compared to H , indicating the large majority of the dissipation can indeed be associated to crack propagation (as assumed in Section 4.2.3). Prior to the force peak, we observe a linear increase of $\tilde{S}_{\mathcal{Z}}$ with crack extension, followed by a plateau after this peak. We attribute the observed decrease for $c \rightarrow L$ to the interaction of the field ϕ with the right edge of the sample (this conclusion was drawn by comparison with simulations for samples with varied lengths, the data is omitted). For the points A, B, P and C labeled on this curve, we provided snapshots (Fig.(4.4d)) of the corresponding damage density $\phi(\mathbf{X}, \lambda)$. As explained in Section 4.3.2, this field is used to define the damage zone, labeled in blue, and its size $\tilde{S}_{\mathcal{Z}}$.

4.4.2 Toughness: definition and interpretation

For elastic materials, the toughness is a material property independent of the sample geometry or loading conditions and may be extracted from experimental data similar to Fig.(4.4) (gray plot). However, for soft solids, it is unclear how one should process the experimental data to measure toughness or under what conditions this type of measurement reflects an intrinsic material property. In the following, we discuss the physical interpretation of toughness through the analysis of the resistance and force-extension curves.

4.4.2.1 Review of existing experimental protocols

In the primarily elastic elastomers of Rivlin and Thomas [114], rupture occurs at a distinct value of the applied stretch λ_b . At this stretch, they observe an immediate drop in force. The force-stretch curve they report has a similar shape to the ideally-elastic gray plot of Fig.(4.4b). The measurement protocol they proposed to obtain the toughness consists of two subsequent tests. First, a pure shear fracture test is done to measure λ_b . Then, a similar uncracked sample is stretched up to λ_b and the toughness is obtained as,

$$\Gamma = \tilde{H} \int_1^{\lambda_b} \sigma_N d\lambda \quad (4.21)$$

where \tilde{H} is the height of the uncracked sample and $\sigma_N = F/\tilde{A}$ is the nominal stress (with \tilde{A} the cross sectional area).

As noted by Zhao [153], this protocol to measure toughness has been extended to hydrogels. It has also been used to measure toughness in filled elastomers with Mullins effect [115, 3]. However, this protocol is used with modifications that have important consequences on the toughness recorded. This is because the force-stretch curves obtained experimentally for dissipative materials resemble Fig.(4.4b): the stretch at crack initiation, peak force and rupture are distinct values. Which one is relevant to use in Eq.(4.21)? In double-network hydrogels, Zheng *et al* [154] used the stretch at initiation to define toughness. In elastomers, Roucou *et al* [115] used the stretch at *catastrophic break* that they locate somewhere between the stretch corresponding to peak force and rupture ($F = 0$). For the filled rubbers of Alzugaibi *et al* [3], no clear drop in force was observed and they selected the value of stretch corresponding to $dc/d\lambda \gg H$ to define toughness. The argument for this criterion is that, despite not achieving a steady state under monotonic loading, there is a point after which the crack propagates much faster than the stretch can increase.

4.4.2.2 Interpretation of the peak force

For elastic materials, the peak force corresponds to crack initiation. In contrast, for soft solids there can be a significant increase in force after crack initiation because the crack propagates

slower and allows for further stretching. We hypothesize that the peak in the force-stretch curve is controlled by a competition between the increased stretch in the uncracked part of the sample and the reduction of the size of this uncracked region. If this vision is correct, we expect the force peak to significantly vary with the length of the sample. On Fig.(4.5c) we reported the force-stretch curves for three samples of different lengths while keeping other parameters constant and indeed, we observed that while the crack initiation occurred at the same stretch, there was a significant variation in the stretch corresponding to the force peak. The resistance curves for these samples (Fig.(4.5b)) overlapped well: only a small difference in the value of $\mathcal{G}(c \rightarrow L)$ was observed, which we attribute to the crack tip interacting with the edge of the sample. Clearly the difference in the value of \mathcal{G} corresponding to the force peak does not reflect a significant change in the resistance of the material to cracking. To further confirm our hypothesis, we adopt the simplistic model described by Fig.(4.5a), where we divided the pure shear sample in two regions: a cracked region that does not bear any load, and an uncracked region that we assimilate to a tensile strip with uniform strain energy density $W_{ff}(\lambda)$. The traction vector, uniform over top boundary, can therefore be obtained from the uniform stress in the tensile strip as $\tilde{\mathbf{t}} = \mathbf{P}(Y = H) \cdot \mathbf{e}_Y$ and the force approximated as,

$$F_{approx} = w(L - c)\mu(\lambda - \lambda^{-3}) \quad (4.22)$$

This approximation has been reported on Fig.(4.5c) and overlaps well with the simulation data. Therefore, the peak force indeed reflects the point when further gain in force through stretching cannot be compensated by the loss of stiffness resulting from a reduction in the size of the uncracked region. The value of stretch at the peak force does not reflect a particular change in the resistance to cracking of the material as illustrated by Fig.(4.5b), and does not appear relevant to be the basis for an operational definition of the toughness in soft solids.

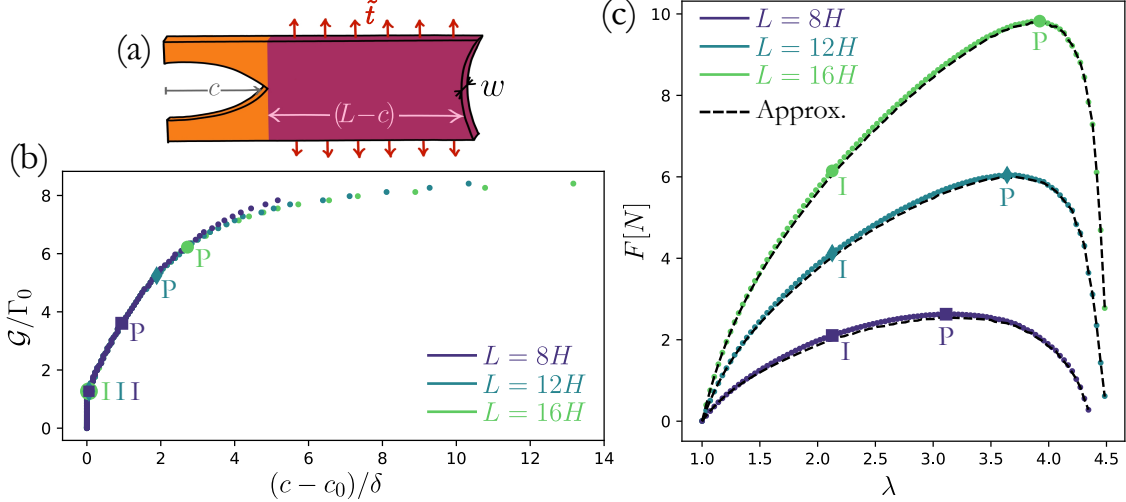


Figure 4.5: (a) Schematic describing the approximation: the orange part cannot bear load and the purple part is a tensile strip with uniform strain energy density W_{ff} . The traction vector, uniform over the surface $w(L - c)$, is used to define F_{approx} in Eq.(4.22). (b) Resistance curves for samples with increasing length L . Other parameters are listed in Table H.1 (SIM-B). (c) Force-extension curves, the approximation defined per Eq.(4.22) is reported for each sample.

4.4.2.3 Energy release rate at crack initiation

From Eq.(4.10), it is clear that G is only meaningful during crack propagation. As pointed out by Long *et al* [85], for elastic materials a more appropriate crack initiation criterion is often derived from the field approach, based on the J-integral. It may be written $J_{init} = J_{crit}$ where,

$$J = \int_{\tilde{C}} \left((\mathbf{n} \cdot \mathbf{e}_X) \frac{\partial W}{\partial X} - t_i \frac{\partial u_i}{\partial X} \right) dl \quad (4.23)$$

with \tilde{C} a smooth non-intersecting contour that encloses the crack tip and \mathbf{n} the normal to this contour. For elastic materials, this criterion is equivalent to $G = \Gamma_0$ because, at initiation, we may show $J_{init} = G$ and $J_{crit} = \Gamma_0$. In general, for inelastic materials, this result does not hold. However, because dissipation is rate-independent, all material points experience the same loading. Since we assumed no material point experiences unloading unless the crack propagates, the material is indistinguishable from a non-linear elastic solid prior to crack initiation and the criterion $G = \Gamma_0$ is expected to remain relevant.

Despite these considerations, the result of Fig.(4.4a) clearly shows $\mathcal{G}_{init} > \Gamma_0$. To understand what sets the value of \mathcal{G} at crack initiation, we ran three sets of simulations. In the first set, referred to as SIM-C, we varied the amount of dissipation through the parameter α while keeping other parameters constant (Table H.1). In the second set (SIM-D), we varied the size of the refined part of the mesh in the zone surrounding the crack tip. Finally, the set SIM-E refers to simulations with varying σ at constant Γ_0 .

On Fig.(4.6a) we notice that \mathcal{G}_{init} decreases for less dissipative materials and approaches Γ_0 for lower values of α . This result suggests that some amount of unloading must occur even in the absence of crack propagation and lead to some energy dissipation prior to initiation. We confirm this hypothesis by plotting the corresponding energy dissipated up to initiation (Fig.(4.6b)), which follows the same trend. On Fig.(4.6c), we plotted the tensile component of the stress P_{22} on a line near the crack tip, at the global stretch λ_{init} and $\lambda_{init} - \Delta\lambda$: it shows that, upon a small increment of stretch $\Delta\lambda$ leading to initiation, there are indeed material points located just behind the crack tip that experience unloading. We also plotted the value of $1 - \eta$ at initiation over this line on Fig.(4.6c) (right axis): this is a measure of the local damage resulting from the unloading right behind the crack tip. We therefore attribute the fact that $\mathcal{G}_{init} > \Gamma_0$ to the unloading occurring in a region right behind the crack tip, which is associated to a small amount of energy dissipation prior to crack initiation.

As a consequence of this interpretation of the reading \mathcal{G}_{init} , we also expect \mathcal{G}_{init} to depend on the size of the mesh near the crack tip h , since initiation is detected numerically as $c = c_0 + h > c_0$. On Fig.(4.6d), we show that \mathcal{G}_{init} indeed increases when the local mesh size h is increased. If we compare the amount of damage captured with two distinct mesh sizes (Fig.(4.6e)), we notice that a coarser mesh artificially increases the extent of the region where unloading occurs (by associating initiation to a higher value of the global stretch), leading to more energy dissipation and ultimately larger \mathcal{G}_{init} . Experimentally, if crack initiation is detected using a camera, there is also a detection threshold: it is expected to play a similar role to the mesh size in numerical simulations and affect

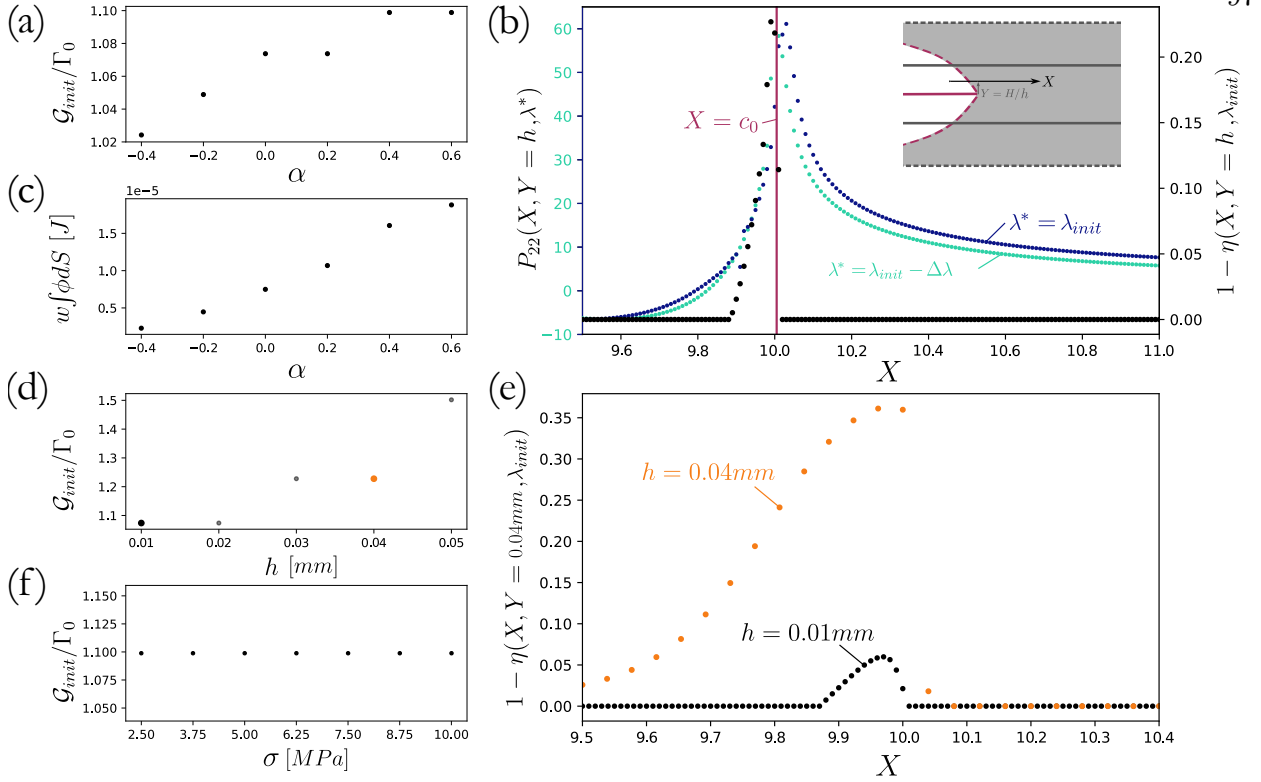


Figure 4.6: (a) \mathcal{G} at crack initiation for increasingly dissipative materials. Parameters are listed in Table H.1 (SIM-C). (b) The left y-axis gives the tensile component of the first Piola-Kirchhoff stress P_{22} near the crack tip (for points on the line $X \in [9.6mm, 11.0mm]$, $Y = h$ where the coordinates (X, Y) are measured in the reference configuration) at stretch $\lambda^* = \lambda_{init}$ and $\lambda^* = \lambda_{init} - \Delta\lambda$. The inset is a schematic representing the position of the line over which stress is measured, the reference/deformed configuration is represented in solid/dotted lines. The right y-axis represents gives the local value of the field $1 - \eta$ for the same line at λ_{init} . Parameters are listed in Table H.1 (SIM-C). (c) Energy dissipated up to crack initiation for increasing α . Parameters are listed in Table H.1 (SIM-C). (d) \mathcal{G} at crack initiation for increasing mesh size h . Note h corresponds to the size of the refined mesh near the crack. Parameters are listed in Table H.1 (SIM-D). (e) For two values of h , the value of the field $1 - \eta$ on the line previously defined is given at initiation. Parameters are listed in Table H.1 (SIM-D). (f) \mathcal{G} at crack initiation for increasing values of the maximum stress σ prescribed in the cohesive zone model. Parameters are listed in Table H.1 (SIM-E).

the measurement of \mathcal{G}_{init} .

Finally, the set of simulations SIM-E did not reveal a dependence of \mathcal{G}_{init} on the maximum stress σ of the cohesive zone model (Fig.(4.6f)).

4.4.2.4 Operational definition

Because the approach to increasing toughness in soft materials consists in introducing dissipation mechanisms [153], we need to provide a definition of toughness and a methodology to measure it that takes into account the dissipative part of the energy release rate. Direct measurements of the global and dissipative energy release rates defined per Eqs.(4.10,4.11) cannot be obtained from the classic pure shear fracture test under monotonic loading. Therefore, our goal is to provide an operational metric accessible to experimentation, that reflects material properties as much as possible, together with guidelines to interpret the measurement.

To do so, we simulated a series of pure shear tests in similar conditions for increasingly dissipative materials (through an increase of the parameter α defined in Section 4.2.1). The resulting resistance and force-stretch curves are provided as Figs.(4.7a,c).

For $\alpha = -0.2$, the resistance curve is flat and resembles that of an elastic material. With increasing dissipation, \mathcal{G} keeps increasing after initiation and we observe slower increase and larger overall values with increasing α . Note that the rate of increase of the resistance curve can be divided into two components,

$$\frac{d\mathcal{G}}{dc} = \left(\frac{d\mathcal{G}}{d\lambda} \right) \left(\frac{dc}{d\lambda} \right)^{-1}. \quad (4.24)$$

The relative contribution of each can be appreciated from Fig.(4.7b): after the force peak, the rate of increase of \mathcal{G} with λ is linear while the rate of increase in crack length is superlinear, which is responsible for the flattening of the resistance curve. Clearly, the rate at which the resistance curve is flattening after the force peak is slower for increasing α (Fig.(4.7d)). This is also reflected on Fig.(4.7c) in the rate at which the force drops: we notice it drops quickly after the peak for $\alpha = -0.2$ while for $\alpha = 0.6$ the force is maintained close to its peak value upon increased stretching before eventually dropping. This correlation between how fast the force drops upon stretching after

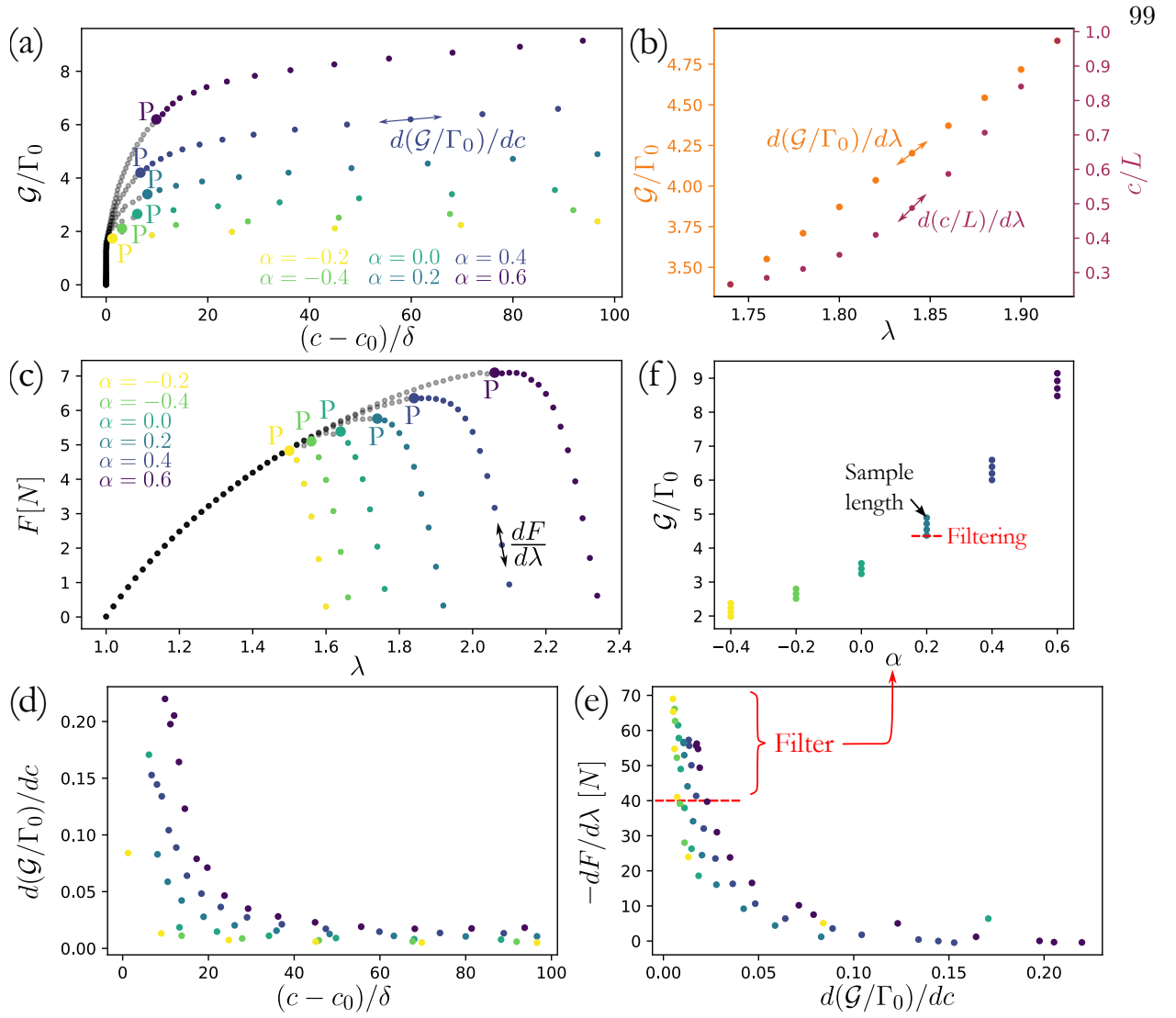


Figure 4.7: (a) Resistance curves for varying α . The competition of $d\mathcal{G}/d\lambda$ with $dc/d\lambda$ leads to the slope of the resistance curve $d\mathcal{G}/dc$. (b) Rates of increase of \mathcal{G}/Γ_0 and c/L with λ after the force peak. (c) Force-stretch curves for varying α . The force peak is labeled (P). The slope of the curve $dF/d\lambda$ drops after the peak. (d) Slope of the resistance curves after the force peak. For all values of α , the slope drops to almost zero and takes longer propagation for increasing α . (e) The drop in the slope of the resistance curve is correlated to a sharp drop in the slope of the force-stretch curve. Retaining the points for which the drop in force is larger than a limiting value ($-dF/d\lambda > 40N$) ensures the increase of \mathcal{G}/Γ_0 with further crack extension remains slow. (f) The values of \mathcal{G}/Γ_0 for the points filtered using this criterion are reported for each value of α . The lowest measurement is controlled by the filtering criterion while the largest is controlled by the length of the sample. Parameters are listed in Table H.1 (SIM-F).

the peak (measured by the slope $-dF/d\lambda$) and the flattening of the resistance curve (measured by dG/dc) is provided by Fig.(4.7e). Such correlation can also be observed for filled rubber in the experimental data of Alzughabi *et al* (on their figure 7) [3].

As discussed in Section 4.4.1, there can be no true steady state under monotonic loading. Therefore, the translational invariance required to obtain $G = \mathcal{G}$ is never achieved exactly. However, the resistance curves obtained with increasing α on Fig.(4.7a) clearly flatten around distinct values $\mathcal{G}(c \rightarrow L)$, reflecting a larger dissipated energy release rate G_D . To define an operative value of toughness and effectively compare different materials, we propose to use a criterion based on the drop of force measured by $-dF/d\lambda$. As illustrated on Fig.(4.7e), selecting points above a given value $-dF/d\lambda > (-dF/d\lambda)_{lim}$ ensures that the resistance curve is “flat enough”. This type of filtering is fully independent of the sample length. Indeed, if we were to use the value $\mathcal{G}(c = L)$ as a metric for toughness instead, we would be at a risk to underestimate the toughness when the length of the sample is too short.

We may notice this on Fig.(4.5c): if we were to use $\mathcal{G}(c = L)$ for the smallest sample ($L = 8H$), we would underestimate the toughness, while the criterion based on the slope would disqualify the measurement (note the significantly lower value of $-dF/d\lambda$ on Fig.(4.5c) for this sample). This type of filtering has been implemented to record the acceptable measures of operational toughness for increasingly dissipative materials on Fig.(4.7e). If the sample was not long enough, there would be no reported value of toughness after filtering. However, when it is, there is a scattering in the measured value where the lowest value is set by the arbitrarily defined limit in the slope $(-dF/d\lambda)_{lim}$ and the highest is set by the sample length. While the specific value of the acceptable slope for the drop of the force-stretch curve is set arbitrarily, the criterion itself is relevant because it ensures that the resistance curve is sufficiently flat. If we were able to observe this flattening in real time and adjust the experimental conditions to fix the global stretch λ to a constant value, we would reach a proper steady state at a value of $G = \mathcal{G}$ that is not too far from that measured using the proposed criterion. Therefore, we argue that this type of criterion can constitute an effective way to measure the toughness of different materials independently of the sample length.

While it is not clearly stated in their paper [115], Roucou *et al* seem to be using a similar criterion. In their experimental results (figure 5 in their publication), they observe a very clear drop in the force-stretch curves at a given corresponding critical stretch. They use this value to obtain what they call the *critical energy release rate*. The criterion we proposed is directly equivalent to their protocol, but it extends to situations where the drop in force is more progressive (as observed in [3]).

4.4.3 Effect of the sample height

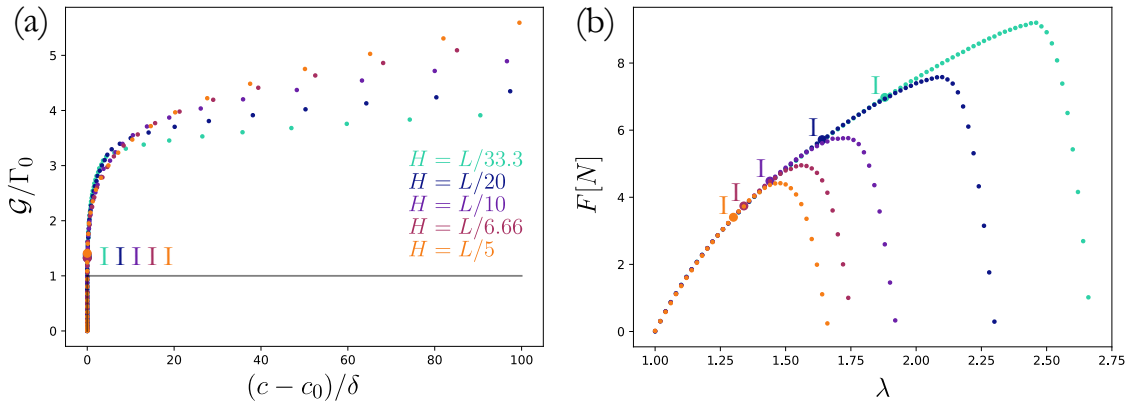


Figure 4.8: (a) Resistance curves for increasing sample height. The initiation points are labeled (I). (b) Force-stretch curves for increasing sample height. Other parameters are listed in Table H.1 (SIM-G).

In elastic materials, the value of stretch corresponding to the force peak varies with sample height H . Indeed, since $G = 2HW_{ff} = \Gamma_0$ when the crack starts propagating unstably, samples with larger H break at lower W_{ff} and therefore lower stretch. This is because, upon stretching a sample of an increment $d\lambda$, a larger amount of elastic energy may be stored in samples with larger H . For elastic materials, the resistance curve therefore remains unaffected by a change in sample height, while the force-stretch curve features a smaller force peak and stretch at break for increasing H . For inelastic materials however, we expect the resistance curve to be sensitive to a change in sample height. Indeed, dissipation due to the Mullins effect is sensitive to the maximum stretch.

Therefore, if initiation occurs at lower stretch in samples with larger H , we expect dissipation and thus the component G_D to be affected upon changing the height of the sample. Additionally, as we have demonstrated previously, the value of \mathcal{G} at initiation is typically larger than Γ_0 and varies with α . This also raises the question of whether or not the value of \mathcal{G} at initiation will be as insensitive to changes in H as in elastic materials.

On Fig.(4.8), we report the resistance and force-stretch curves obtained from simulations with increasing values of the sample height from $H = L/33.3$ to $H = L/5$. The first observation we can make on Fig.(4.8a) is that the initiation occurs for $\mathcal{G}_{init} > \Gamma_0 \forall H$, with no clear difference in \mathcal{G}_{init} from increasing H , similarly to elastic materials. Then, we observe that \mathcal{G} increases slightly slower with crack length for samples with larger H . Finally, the resistance curve for samples with larger H flattens at larger values of $\mathcal{G}(c \rightarrow L)$. On the force-stretch curves (Fig.(4.8b)), we observe a behavior reminiscent of what happens in elastic materials, with a force peak being reached at lower stretch for samples with larger H . The faster flattening of the resistance curve for larger samples is also reflected in the sharper drop in force, as discussed in the previous section.

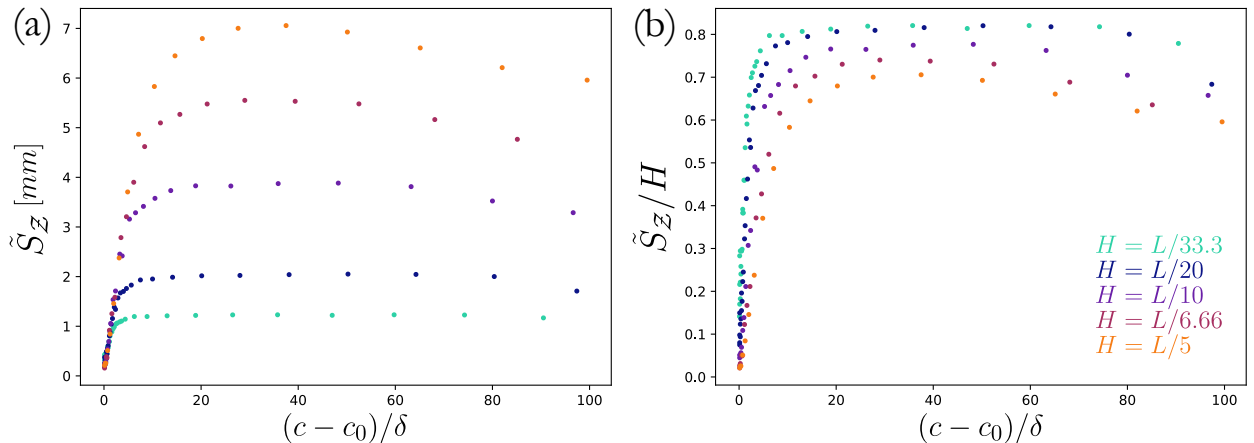


Figure 4.9: (a) Increase in the size of the damage zone with crack extension for different H . (b) Same data with the size of the damage zone normalized by H . Parameters are listed in Table H.1 (SIM-G).

We hypothesize that the differences in the rate of growth of \mathcal{G} with crack extension observed

for samples with different H could be related to differences in the rate of growth of a damage zone. Specifically, we expect the dimensions of the sample set a limit to the growth of such a damage zone, which could be used to explain the observed differences in the resistance curves. The damage zone is defined in Section 4.3 and its size is given by Eq.(4.20). On Fig.(4.9a), we plotted the evolution of \tilde{S}_D with crack extension: we first observe a linear increase followed by a plateau. If we normalize it by the height of the sample, we notice the final size is indeed controlled by H (Fig.(4.9b)).

4.5 Conclusion

This work focuses on the fracture of soft materials with rate-independent dissipation. Specifically, we focused on incompressible neo-Hookean solids with Mullins softening. This type of behavior is representative of a large class of materials including elastomers and multi-network hydrogels. Based on previous works [110, 88], we started by deriving a fracture criterion from first principles. We arrive at a decomposition of the global energy release rate into an intrinsic part and a dissipative part $G = \Gamma_0 + G_D$. We explain why direct measurement of these energy release rates is not possible by extending the traditional protocol of Rivlin and Thomas [114] for primarily elastic elastomers to inelastic solids. Therefore, we focused on interpreting the relationship between an operational metric \mathcal{G} , accessible to experimentation, and the energy release rate. Using a series of finite element simulations, we explored the influence of sample geometry and material properties on the outcome of pure shear tests, in order to distinguish what is related to their intrinsic properties from what is an artifact of the testing protocol. From our results, we suggest the following guidelines:

- ◊ The value of the operational metric \mathcal{G} at crack initiation is expected to depend on the measurement resolution. Additionally, our simulation did not reveal specific differences between the field and energy approaches.
- ◊ To compare the toughness of materials, it is relevant to measure the critical stretch based on the slope of the force-stretch curve. This type of criterion does not depend on sample length.

- ◊ As in elastic materials, the height of the sample does not influence the measurement of the intrinsic toughness. However, it affects the measurement of the total toughness, which should therefore be interpreted as apparent. We recommend using the same sample height to compare different materials.

To conclude, while the toughness of soft solids with Mullins softening cannot be interpreted as a material property, it is possible to effectively compare the performances of materials using simple mechanical testing with a few precautions. Ideally, we recommend that the full resistance curve (as defined in this chapter) be reported along the force-stretch curve for these materials, which calls for the measurement of crack length over time $c(t)$, as done in [3] for example.

Chapter 5

Investigating the mechanical failure mechanisms of a novel CFRP composite to inform computational models

The work presented in this chapter was a collaboration with my advisor Rong Long, researchers affiliated with the startup Rockytech (Louis Corcoran and Yinghua Jin) and researchers from the chemistry department of the University of Colorado Boulder (Hongxuan Chen and Wei Zhang). It was published in the SPIE conference proceedings [89].

5.1 Introduction

The United States Corporate Average Fuel Economy (CAFE) standards were signed into law in 1975, resulting in an $\sim 25\%$ reduction in oil consumption compared to initial projections [135]. Moreover, updates to these standards are expected to result in improve vehicle fuel economy by $> 25\%$ over the next few years (2026 compared to 2021) [102] resulting in technological advancements in individual vehicles and improvements to their operational environmental impact. Of these advancements, vehicle lightweighting has been developed as a means to significantly reduce vehicle fuel consumption, since fuel efficiency is up to 50% dependent on mass [78]. Indeed, it has been estimated that a mass reduction for a given vehicle of only 10kg can reduce the vehicles carbon emissions by nearly 1g/km traveled [1]. In this regard, carbon fiber reinforced polymer composites (CFRPs) can be a significant asset. CFRPs are utilized in a variety of industry sectors, including aerospace, defense, wind energy, and transportation, due to their competitive stiffness and strength (compared to steel and aluminium) available at much lower density compared to traditional ma-

terials [106]. In the automotive industry, however, many CFRP parts are limited to high end vehicles [105] because they are costly and energy intensive to produce [26]. Further, at functional end-of-life, composite recycling is technologically difficult, with the separation of carbon fibers from thermoset resin being a principal challenge [108]. Thus, there is reason to develop CFRPs that are cost-competitive and offer closed-loop recyclability while maintaining mechanical integrity.

In efforts to improve the closed loop recyclability of CFRPs, emerging technologies including High Performance Discontinuous Fiber (HiPerDiF) [109] alignment and Tailorable Universal Feedstock and Forming (TuFF) [143] technologies have been developed to produce CFRPs with high mechanical properties utilizing chopped recycled carbon fibers ($3 - 6\text{mm}$), successfully reusing carbon fibers to create structural components. Unfortunately, these techniques make use of thermoset polymers leading to the same recycling challenges of traditional CFRPs. Recently, we have utilized milled recycled carbon fibers and covalent adaptable networks, or CANs, to develop fully reproducible and recyclable CFRPs. Like thermosets, CANs result in a crosslinked polymer matrix, resulting in a material with robust mechanical and thermal properties. Unlike thermosets, which lack recyclability and post-processing malleability due to permanent crosslinks, CANs are capable of undergoing bond exchange reactions that allow the polymer matrix to rearrange under stress in the rubbery regime [63]. Further, CANs can be depolymerized [145], allowing the entire CFRP to be recycled with closed-loop efficiency.

The prospect of increased CAN-based CFRP use as automotive structural components calls for a fundamental understanding of their damage mechanisms. We expect (i) matrix cracking and (ii) fiber-matrix debonding to be the main contribution to damage in CFRP. While CFRP are glassy at temperatures of operating conditions, studying their rubbery behavior is a relevant starting point [83, 151]. In this work we characterize the dynamic mechanical behavior of the unfilled matrix under low stretch conditions. From these experiments, we show (1) that the bond exchange reaction in the vitrimer matrix may be modeled using the Arrhenius equation and (2) that the competition between the bond exchange rate and the loading rate controls the amount of rearrangement in the matrix (healing) and produces a mechanical response ranging from purely elastic to purely

viscous. Then, we examine the composite break interface via scanning electron microscopy (SEM) to understand what mechanisms lead to catastrophic failure (e.g., matrix cracking, fiber-matrix debonding). Finally, we propose a series of experiments to fully characterize the damage mechanisms of CFRP—data that will be utilized to inform the development of a constitutive model based on the statistical description of the network.

5.2 Methods

5.2.1 Problem breakdown

To understand the damage mechanisms in CFRP composites under extreme stretch, we broke down the problem as follows.

- (I) Understand the deformation and reconfiguration of the Vitrimer matrix under extreme stretch.
 - (I.i) Develop a model informed by experiments of the Vitrimer matrix under low stretch.
 - (I.ii) Informed by experiments, modify this model to include damage under extreme stretch.
- (II) Understand the deformation and reconfiguration of the CFRP under extreme stretch.
 - (II.i) Experimentally investigate the CFRP micro-structure.
 - (II.ii) Develop a method to align carbon fibers.
 - (II.iii) Informed by experiments, modify this model to include carbon fibers.

The present work will be concerned with (I.i) and (II.i). In Section 5.4, we explain our plan to complete the study.

5.2.2 Preparation of the samples

5.2.2.1 Vitrimer matrix

Please note that the vitrimer matrix used in this study is a trade secret of RockyTech Ltd. Crosslinker 1 (Oakwood Chemical), monomer 1 (Sigma-Aldrich), and monomer 2 (TCI America)

were used as received. Crosslinker 2 was synthesized from commercial starting material (TCI America) with quantitative conversion via proton nuclear magnetic resonance (H^1 NMR) and isolated via crystallization and vacuum filtration. Following this, crosslinker 1 and crosslinker 2 were added to a 20 mL scintillation vial (at optimized mol. ratios; vial 1) followed by the addition of 4.5 mL of DMF; this solution was then placed on a hotplate (80 °C, 240 rpm) and stirred until solid dissolution (10 min). monomer 1, monomer 2, and 1 mL DMF were added to a second scintillation vial (vial 2) and placed on a hotplate (80 °C) until dissolved (~ 10min). Following monomer dissolution, the contents of vial 2 were transferred to vial 1 via glass Pasteur pipet; vial 2 was then rinsed with 3 x 0.5 mL DMF and the rinsate was also transferred to vial 1 via Pasteur pipet. Vial 1 was then returned to the hotplate and stirred for an additional 10 min before being solution cast into a PTFE mold and transferred to a preheated oven. The resultant vitrimer matrix was cured over 18 hrs following a ramped heating protocol and, after curing, the vitrimer was removed from the oven. Warped specimens were flattened in a heat press and rectangle punchouts were cut from the polymer sample for characterization via dynamic mechanical analysis (DMA).

5.2.2.2 CFRP

Milled carbon fiber (Zoltek; mCF) was used as received. Carbon fiber-reinforced polymer composites were prepared following the same general procedure as outlined in Section 5.2.2 50 wt% mCF (of the final composite mass) was added to vial 1 following crosslinker dissolution in 2.5 mL DMF. This solution was then stirred on the hotplate for an additional 20 minutes before the addition of vial 2 contents plus 3 x 0.5 mL DMF rinsate (note: vial 2 contents were initially dissolved in 0.5 mL DMF). Vial 1 was then returned to the hotplate and stirred for an additional 10 min prior to solution-casting into a PTFE mold. Samples were cured over 18 hrs following a ramped heating protocol, flattened after curing, and rectangle punchouts were cut from the polymer for characterization via DMA.

5.2.3 Experimental testing

5.2.3.1 Dynamic mechanical analysis (DMA) and stress relaxation

Glass transition temperatures (T_g) of both vitrimer and composite were measured on a Q800 DMA (TA instruments) in tension mode with approximate sample dimensions of 5.1 mm (width) x 0.75 mm (thickness) x 15.5 mm (length) for the vitrimer. The tests were strain controlled at 0.1% engineering strain, a temperature range from 25 – 150 °C, initial soak time of 5 min, ramp rate of 3 °C/min, and frequency of 1 Hz. Stress relaxation experiments were conducted on a DMA Q850 (TA instruments) in tension mode with approximate vitrimer sample dimensions of 5 mm (width) x 0.8 mm (thickness) x 12 mm (length). Lastly, the engineering strain was fixed at 5% for the vitrimer matrix. Samples equilibrated at the test temperature for 5 min before the start of a given measurement.

5.2.3.2 Scanning electron microscopy (SEM)

Following tensile testing, a razor blade was used to cut a 3 mm section of sample away from the break interface of a given dogbone. These cut sections were then mounted on carbon tape on an SEM stub with the original break interface normal to the plane of the stub. This was done to ensure that the fracture interface observed via SEM failed under relevant testing conditions (i.e., tension at room temperature). Micrographs were taken on a Hitachi SU3500 microscope at an accelerating voltage of 10 kV and a working distance of 7 mm. Note that samples were not sputter coated due to the conductive nature of carbon fibers.

5.2.4 Multiscale modeling of CFRPs mechanics

Vitrimers are covalent adaptable networks (CAN). They have strong covalent bonds exhibiting exchange reactions that allow the matrix to rearrange under stress (above their glass transition temperature) without loss of connectivity. In this work we propose a statistical model of CAN, the macroscopic mechanical behavior is then obtained from the underlying network dynamics. The

emerging behavior upon loading is non-linear viscoelastic.

5.2.4.1 Statistical model of covalent adaptable networks

We describe CAN as networks of crosslinked flexible chains within an elementary volume of the continuum V_0 in thermal equilibrium with a heat bath at temperature T (Fig.(5.1a)). We restrict our attention to the mechanically active chains, *ie* chains crosslinked at both ends, assuming a concentration n_0 in V_0 . We denote \mathbf{r} , the end-to-end vector of chains in this network (Fig.(5.1b)). Chains constantly change their \mathbf{r} due to thermal fluctuations, exploring the conformation space $\Omega = \mathbb{R}^3$. In the undeformed configuration, we denote $P_0(\mathbf{r})$ the probability of finding a chain in a volume $d\Omega$ located at \mathbf{r} (e.g. Fig.(5.1c)). When a velocity gradient $\mathbf{L} = \dot{\mathbf{F}}\mathbf{F}^{-1}$ (with \mathbf{F} the deformation gradient) is applied, we assume chains deform accordingly $\dot{\mathbf{r}} = \mathbf{L}\mathbf{r}$. Additionally, bond exchange reactions may occur at rate k_e . Under these dynamic events, the probability of \mathbf{r} and the chain concentration become respectively $P(\mathbf{r}, t)$ and $n(t)$. Previous works [136] have shown that,

$$\frac{\partial P}{\partial t}(\mathbf{r}, t) = -\mathbf{L} : \left(\frac{\partial P(\mathbf{r}, t)}{\partial \mathbf{r}} \otimes \mathbf{r} \right) - P(\mathbf{r}, t)Tr(\mathbf{L}) - k_e(\mathbf{r})P(\mathbf{r}, t) + \langle k_e \rangle P_0(\mathbf{r}) \quad (5.1)$$

$$\frac{\partial n}{\partial t}(t) = -n(t)Tr(\mathbf{L}). \quad (5.2)$$

The first two terms in Eq.(5.1) may be combined into a divergence term $-\nabla \cdot (P\dot{\mathbf{r}})$ that captures the material derivative due to the velocity gradient, while the subsequent terms capture bond exchange reactions: chains detach in their current configuration (proportionally to P) but reattach in a stress-free configuration (proportionally to P_0). Note $\langle \bullet \rangle = \int_{\Omega} \bullet P d\Omega$ is used to denote integration over the configuration space. Eq.(5.2) reveals that the chain concentration may only vary due to change of volume: bond exchange reactions in CAN do not affect connectivity (contrary to dynamic networks made of ionic bonds).

This model highlights the importance of two rates dictating the rearrangement of CANs under stress: the rate associated to the deformation f (alternatively we may use the spectral norm of the velocity gradient $\|\mathbf{L}\|$) and the rate of bond exchange k_e . These two rates compete and we

may characterize the behavior using the Weissenberg number,

$$W = \frac{f}{k_e}. \quad (5.3)$$

When $W \gg 1$, the material is stretched too fast to allow reconfiguration through bond exchange while for $W \ll 1$ bond exchange reactions happen much faster than stretching. For CAN (but also for other dynamic networks), this competition of timescales produces a mechanical behavior ranging from elastic to fluid-like (see Section 5.3.2).

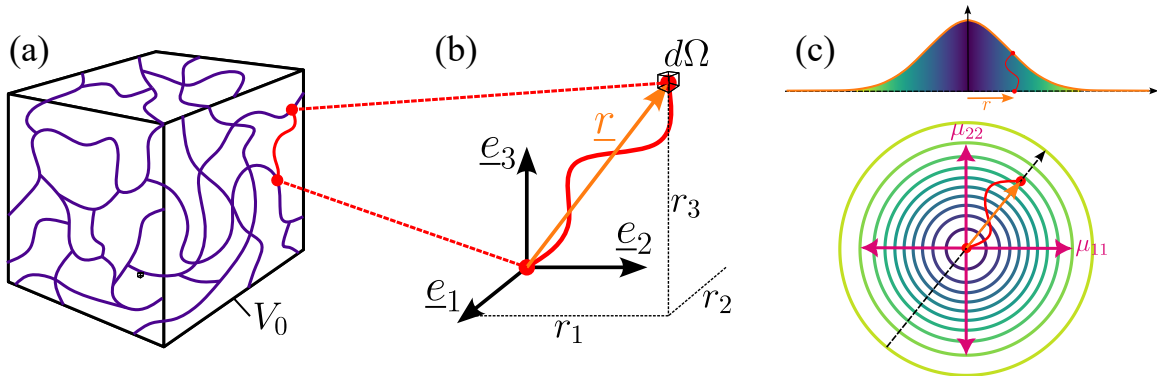


Figure 5.1: (a) Elementary volume of material containing the polymer network. (b) In the conformation space Ω , \mathbf{r} represents chains end-to-end vectors. (c) The distribution $P(\mathbf{r})$ projected over $(\mathbf{e}_1, \mathbf{e}_2)$, the components of $\boldsymbol{\mu}$ measure average chain stretch in principal directions. A 1d projection is also provided: note the typically higher likelihood of short versus long chains.

5.2.4.2 Constitutive behavior

Let $\psi(\mathbf{r}) = \mathcal{U}(\mathbf{r}) - T\mathcal{S}(\mathbf{r})$ be the Helmholtz free energy of a chain with \mathbf{r} . As there are less possible arrangements of Kuhn segments leading to larger \mathbf{r} , the entropy \mathcal{S} of long chains is larger. When Kuhn segments are mostly aligned, they may stretch and an additional enthalpic contribution \mathcal{U} should be considered. The network free energy may be written as

$$\Psi(t) = n(t)\langle\psi\rangle + p(\det(\mathbf{F}) - 1), \quad (5.4)$$

where the first term is the sum of all energy stored in the chains and the second term accounts for volume exclusion represented through the Lagrange multiplier p enforcing the incompressibility condition $\det(\mathbf{F}) = 1$. Assuming an isothermal process, the Clausius-Duhem inequality reads

$$D = \boldsymbol{\sigma} : \mathbf{L} - d\Psi/dt \geq 0, \quad (5.5)$$

where $\boldsymbol{\sigma}$ is the Cauchy stress and D is the mechanical dissipation. The evolution $d\Psi/dt$ can be obtained from Eqs.(5.1,5.2) and we may solve for $\boldsymbol{\sigma}$ and D : this is how the constitutive behavior is derived from the CAN's dynamics.

5.2.5 Reduced model

5.2.5.1 Stress under low stretch

Under low stretch, we may assume the chains free energy is entropy dominated, $\psi \simeq -T\mathcal{S}$. In this case, it is relevant to use the free jointed (or ideal) chain model with free energy $\psi = (3kT/2Nb^2)|\mathbf{r}|^2$ where kT is the thermal energy, N the number of Kuhn segments making up the chain and b their length. This choice also sets the initial distribution as the Gaussian $P_0 = (3/2\pi Nb^2)^{3/2} \exp(-(3/2Nb^2)|\mathbf{r}|^2)$. As shown by Vernerey *et al* [136], under these conditions the Cauchy stress may be written as

$$\boldsymbol{\sigma} = n(t)kT(\boldsymbol{\mu} - \mathbf{I}) + p\mathbf{I}, \quad (5.6)$$

where $\boldsymbol{\mu} = (3/Nb^2)\langle \mathbf{r} \otimes \mathbf{r} \rangle$ is called conformation tensor and describes the average chain stretch in the principal directions of the network. The evolution follows from Eq.(5.1) (with $\mathbf{k}_e = (3/Nb^2)\langle k_e(\mathbf{r})\mathbf{r} \otimes \mathbf{r} \rangle$),

$$\frac{d\boldsymbol{\mu}}{dt} = \mathbf{L}\boldsymbol{\mu} + \boldsymbol{\mu}\mathbf{L}^T - \mathbf{k}_e + \langle k_e \rangle \mathbf{I}. \quad (5.7)$$

5.2.5.2 Arrhenius bond exchange rate

Under extreme deformation, we expect stretched chains to exert forces at their crosslinks thereby increasing the rate of exchange: in general $k_e(\mathbf{r})$ depends on the end-to-end vector. How-

ever, under low stretch, it is reasonable to assume thermal energy dominates: we model the bond exchange reaction with the Arrhenius equation

$$k_e = \nu \exp\left(-\frac{E_a}{RT}\right), \quad (5.8)$$

with E_a the activation energy of the reaction and R the gas constant. In this case we may simplify $\langle k_e \rangle = k_e$ and $\mathbf{k}_e = k_e \boldsymbol{\mu}$ and Eq.(5.7) reduces to $d\boldsymbol{\mu}/dt = \mathbf{L}\boldsymbol{\mu} + \boldsymbol{\mu}\mathbf{L}^T - k_e(\boldsymbol{\mu} - \mathbf{I})$.

5.3 Results

5.3.1 Stress relaxation under low stretch

As explained in Section 5.2.5, under low stretch we hypothesize the bond exchange reaction is Arrhenius-like and the rearrangement of CANs under stress can be understood as a competition between the stretching and bond exchange reaction rates. To verify this hypothesis experimentally, we stretched samples at 5% engineering strain and recorded stress relaxation over time for a set of temperatures in the rubbery regime. Fig.(5.2a) shows the storage and loss moduli with their ratio $\tan(\delta)$ for temperatures $25^\circ C < T < 150^\circ C$. The glass transition temperature has been measured as the first peak of the $\tan(\delta)$ curve as $T_g \simeq 70^\circ C$. Additionally, based on this result we define $T > T_r \simeq 135^\circ C$ as the rubbery regime, which is the region of validity of the model presented in Section 5.2.4. The stress relaxation data is provided as Fig.(5.2b), where the natural logarithm of the stress is reported. This is because under constant stretch ($\mathbf{L} = \mathbf{0}$) with k_e obeying Eq.(5.8), we may solve for $\boldsymbol{\mu}$ in Eq.(5.7) and obtain $\boldsymbol{\mu} = \boldsymbol{\mu}_0 \exp(-k_e t) + \mathbf{I}$. Therefore, the stress in Eq.(5.6) becomes $\boldsymbol{\sigma} = n(t)kT\boldsymbol{\mu}_0 \exp(-k_e t) + p\mathbf{I}$ where $p = -n(t)kT(\mu_{22})_0 \exp(-k_e t)$: it decays exponentially with rate k_e . According to the model, the natural logarithm of the stress should therefore decrease linearly with time. This is indeed the case experimentally for $t > 300s$, at all temperatures. For $t < 300s$ another mechanism, not described by the model, is clearly at play. For example, chains entanglements are ignored in our model and could explain such differences.

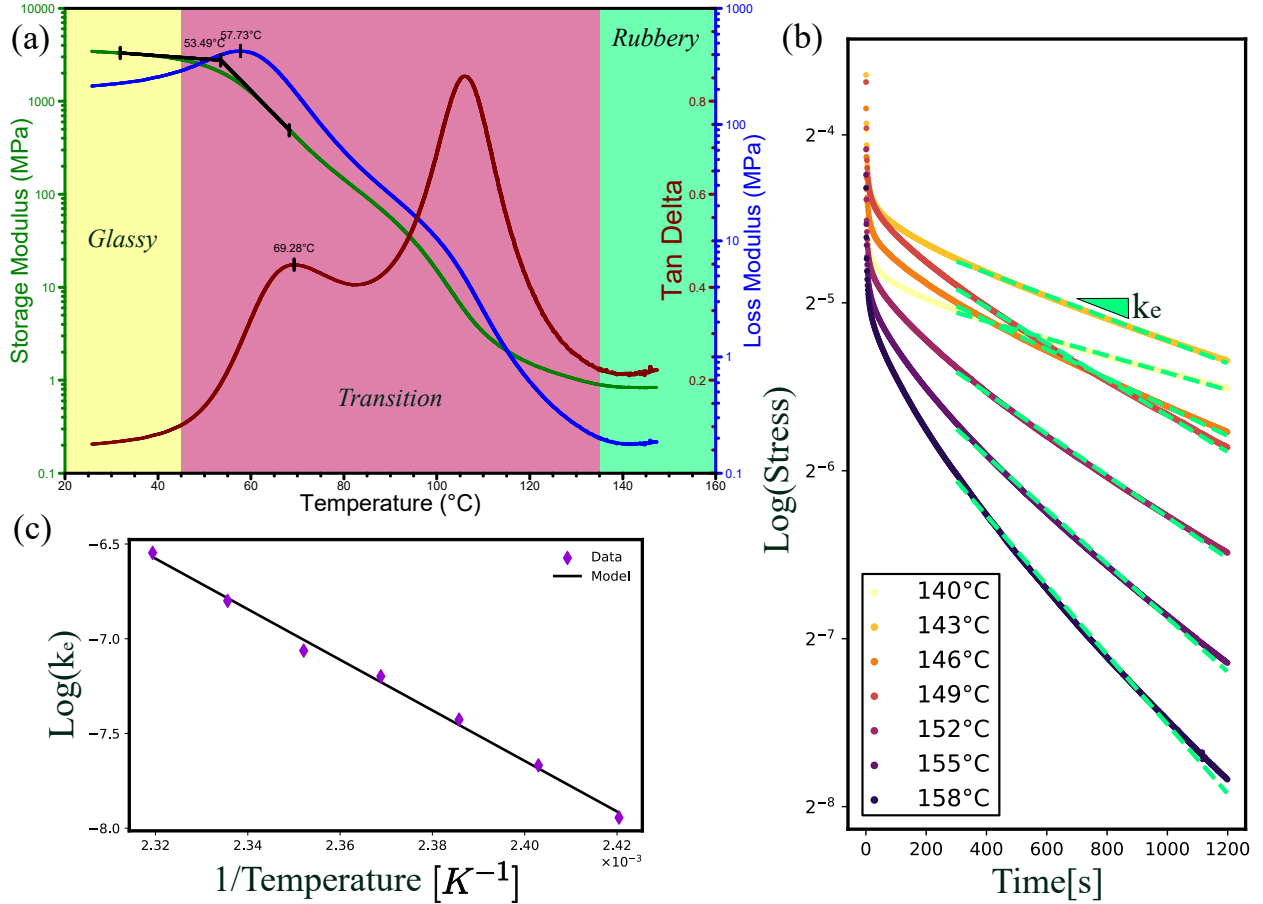


Figure 5.2: (a) Strain controlled temperature ramp data for vitrimer matrix with $T_g \simeq 70^\circ C$ as determined from the first local maxima on the Tan Delta curve. We define $T > T_r = 135^\circ C$ as the limit of the rubbery regime. (b) Stress relaxation data for $T_r < 140^\circ C < T < 158^\circ C$, with stress plotted on base 2 logarithmic scale. The green dotted lines have been fitted to the data for $t > 300s$, indicating an exponential decay of the stress. The decay rate $k_e(T)$ is obtained at each temperature as the slope of the dotted line. (c) The base 2 logarithm of $k_e(T)$ is plotted according to $1/T$. The Arrhenius relationship of Eq.(5.8) fits the data with determination coefficient $R^2 = 0.995$ and we find $E_a = 1.11 \times 10^5 J/mol$ and $\nu = 2.44 \times 10^1 Hz$. Note the temperature is reported in degrees Kelvin for this plot.

For the relevant part of the curve, we fitted the exponential decay predicted by the model over the data and recorded the rate k_e for all temperature values. We then plotted the natural

logarithm of k_e over the corresponding values of $1/T$ (Fig.(5.2c)). If the rate of bond exchange behaves according to Eq.(5.8), we expect $\log(k_e)$ to decrease linearly with $1/T$. A determination coefficient of $\mathcal{R}^2 = 0.995$ confirms that bond exchange reaction in the Vitrimer matrix is indeed Arrhenius-like.

5.3.2 DMA: model prediction

In this section we used our model to predict the behavior of the Vitrimer matrix under loading with increasing frequency in the rubbery regime. The storage and loss moduli reported on Fig.(5.3b) are defined as

$$G' = \frac{\sigma_0}{\epsilon_0} \cos(\delta) \text{ and } G'' = \frac{\sigma_0}{\epsilon_0} \sin(\delta), \quad (5.9)$$

where ϵ_0 and σ_0 are the amplitudes of the sine waves of the imposed engineering strain and the Cauchy stress predicted by the model. The phase shift δ is measured between the signals $\epsilon(t)$ and $\sigma(t)$ after the stress relaxed and became periodic (Fig.(5.3a)). The procedure is repeated for increasing loading frequency f and the moduli are reported according to the ratio $\mathcal{W} = f/k_e$ defined as the Weissenberg number (Eq.(5.3)). For $\mathcal{W} \ll 1$, we observe $G' \rightarrow 0$ and $G'' \rightarrow 0$, indicating fluid-like behavior: bond exchange reaction happens much faster than loading and few energy is dissipated because chains do not have time store any before returning to their stress-free state. When $\mathcal{W} \gg 1$, $G' \rightarrow \sigma_0/\epsilon_0$ and $G'' \rightarrow 0$ (as $\delta \rightarrow 0$), indicative of elastic behavior: bond exchange happens very slowly compared to loading and all the energy is stored elastically in polymer chains. In between, we observe an increase in loss modulus with a peak at $\mathcal{W} = 1$: when the loading rate matches the bond exchange rate, chains have time to store energy before they eventually rearrange, thereby dissipating large amounts of energy.

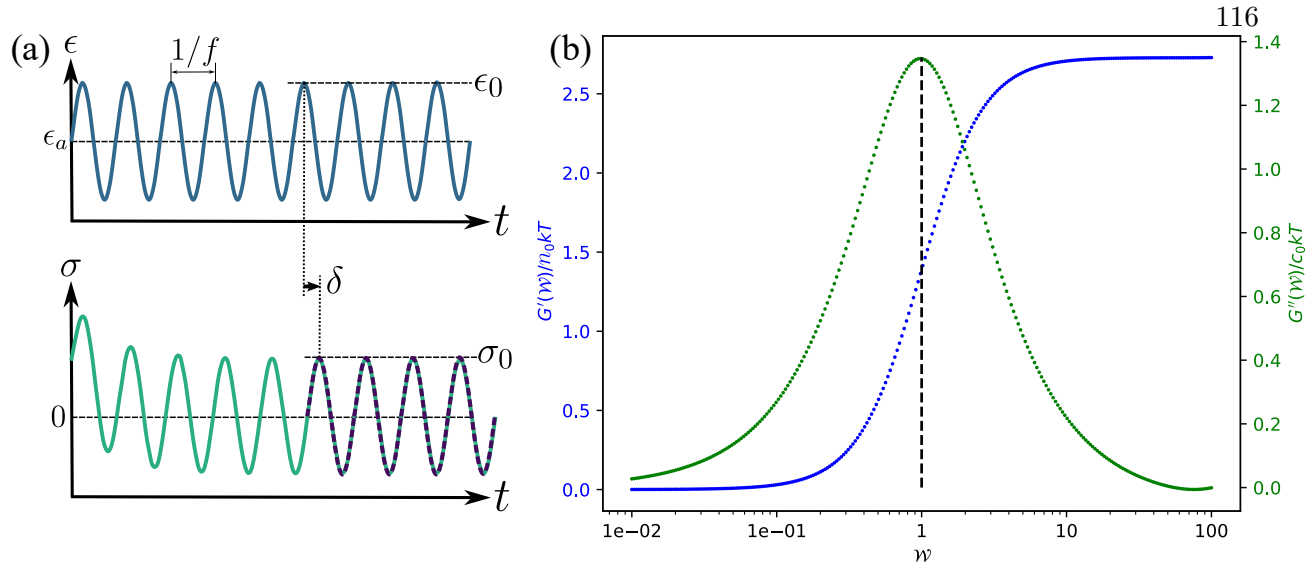


Figure 5.3: (a) Procedure to obtain the storage and loss modulus. The engineering strain is imposed as a sine wave with frequency f and amplitude ϵ_0 . The model prediction of the Cauchy stress σ is recorded over time. A sine wave is fitted over the stabilized part of the signal (after stress relaxation) and amplitudes σ_0 and phase shift δ are recorded. (b) Varying $\mathcal{W} = f/k_e$ through f , the signals $G'(\mathcal{W}) = \sigma_0/\epsilon_0\cos(\delta)$ and $G''(\mathcal{W}) = \sigma_0/\epsilon_0\sin(\delta)$ are recorded for $10^{-2} < \mathcal{W} < 10^2$. Note we normalized G' and G'' by n_0kT with n_0 the initial chain concentration and kT the thermal energy.

5.3.3 Scanning Electron Microscopy results

Characterization via SEM was utilized to investigate the fracture morphology of composite dogbones after tensile failure. As can be seen in Fig.(5.4), there was evidence of both poor (red arrows) and strong (white arrows) fiber-matrix adhesion for these composites, confirming our expectations that both mechanisms would contribute to damage in CFRPs. In regions with poor fiber-matrix adhesion, it is likely that fiber pull-out (*i.e.*, fiber-matrix debonding), matrix cracking, and matrix defects all had a role in localized composite failure, eventually leading to catastrophic failure of the CFRP. In regions with good fiber-matrix adhesion, matrix is seen bound to the fibers after catastrophic failure, suggesting that matrix cracking was the initiator of localized failure.

Lastly, there is evidence that the fiber-matrix adhesion was strong enough to induce fiber cracking (Fig.(5.4b)) since the break interface depicts a fully embedded fiber, though it is possible that this is simply the end of the discontinuous fiber. Considering the demonstrated instances of matrix remaining bound to fibers after tensile failure, improved processing conditions might drive the initial failure method towards matrix cracking, which would theoretically be mendable via inherent bond exchange reactions in the matrix. Indeed, removing voids during curing would eliminate defect sites and likely improve overall matrix-fiber adhesion.

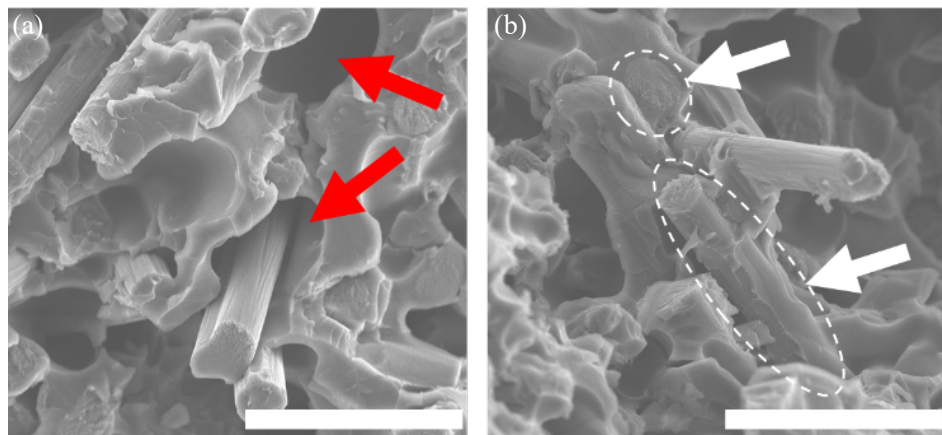


Figure 5.4: Composite micrographs collected at the fracture interface of tensile dogbones; scale bars = $30\mu m$. Note what appears to be voids present in the matrix and at the fiber-matrix interface of some carbon fiber fillers (red arrows) while others exhibit strong adhesion at the matrix-fiber interface (white arrows).

5.4 Preliminary conclusion and future work

With this study we have successfully characterized the behavior of the Vitrimer matrix under low stretch. We understand that bond exchange reactions happen at a rate k_e predicted by the Arrhenius equation and this rate competes with the loading rate to give rise to the observed mechanical behavior. Lastly, we have confirmed via SEM characterization that both matrix cracking and fiber-matrix debonding contribute to CFRP damage, and suggest that improved composite

processing will drive matrix cracking to become the more prevalent initiator of catastrophic failure.

In the future, an additional mechanism under extreme stretching conditions will be considered: chain rupture. When carbon fibers (CF) are introduced to form the CFRP composite, our preliminary experimental investigation revealed that the interface between the CF and the matrix should be given particular attention. On top of chain rupture, we expect the additional damage at this interface to play a role under extreme (and potentially moderate) stretch. In the following, we describe our experimental plan and the extension of the model necessary to capture these more complex aspects of the CFRP behavior.

5.4.1 Experimental plan to study damage

To study damage in the CFRP, we propose the experiment described by Fig.(5.5a), inspired by previous works on filled elastomers [11, 23, 91]. In these studies, the authors show that fillers (in this case carbon black nano particles) lead to important energy dissipation under cyclic loading. Experimentally, they observe the so called Mullins effect: when stretching up to λ_{max} , hysteresis is observed for the first few cycles only, after which the stress-stretch response stabilizes. Further increasing λ_{max} results in added hysteresis for another series of cycles. This observed dependence on the all-time maximum load has been attributed to complex damage mechanisms arising from the coupling between the polymer network and fillers aggregates [91, 12]. Due to the complexity of these mechanisms, many simplified damage models have been proposed. A relevant starting point is the network alteration theory proposed by Marckmann *et al* [91], which can readily be used within our theoretical framework [23]. Adding this type of condition in our model and comparing to such experimental results will therefore help us better understanding the damage mechanisms resulting from using CF as fillers.

Additionally, Diani *et al* showed the existence of damage-induced anisotropy in carbon black (CB) filled rubbers. We plan on replicating their experiment, described by Fig.(5.5b), on the CFRP composites. The idea is to stretch two samples for a few cycles in a given direction, then to repeat

the procedure for one of the samples and change the direction for the other. Diani *et al* observed a softening for the sample that had been turned, revealing damage-induced softening.

CB nano particles are spherical while the CFRP fillers are fibers. For an isotropic CFRP, in which fibers have no preferred direction, we expect to measure a similar damage-induced anisotropy to Diani *et al*. Additionally, we plan on developing a methodology to align fibers and study the effect of this alignment on the damage-induced anisotropy.

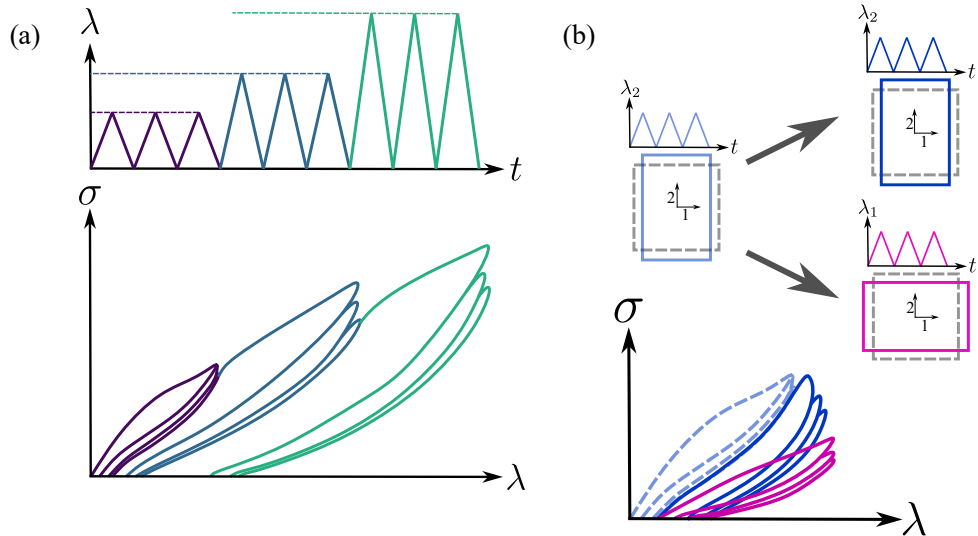


Figure 5.5: (a) Proposed experiment to study damage in CFRP. Under cyclic stretch with increasing magnitude, the stress-stretch curve is expected to feature Mullins effect. (b) Proposed experiment to study damage-induced softening. Two samples are stretched for a few cycles in direction 2, then the same experiment is repeated on the first sample while the same magnitude of stretch is applied in direction 1 to the second sample.

5.4.2 Extension of the model to study damage

To account for extreme stretch, the model presented in Section 5.2.4 needs to be extended. First, it is necessary to consider an enthalpic contribution in the expression of the chain free energy to account for Kuhn segments stretch [90]. With this term, reduction of the model as

described in Section 5.2.5 is not possible: our ability to define a tensor μ relies on the linearity between the force acting on the chain and its end-to-end vector, which is lost when considering an enthalpic contribution. However, this is not a major issue since tracking the evolution of the full distribution $P(\mathbf{r}, t)$ over time at a single material point is not computationally challenging. The second consequence of extreme stretching is that the Arrhenius equation will likely not suffice to model the bond exchange reaction rate: large forces applied on polymer chain will likely increase this rate. Modified Arrhenius equation have been proposed by Bell [8] and Tanaka and Edwards [130] to account for this effect and may readily be used. Chain damage has also been modeled within this framework as a flux through a damage surface with a condition of the type $P(|\mathbf{r}| > r_c, t) = 0$ by Lamont *et al* [75].

Accounting for the effect of CF can be done initially through a condition akin to the network alteration theory of Marckmann *et al*, which may suffice for isotropic CFRPs. However it cannot account for the fiber direction to study samples with aligned fibers. Another approach could be to follow the work of Sridhar *et al* [124]: their model of nematic networks made of stiff rods and flexible chains could be relevant provided we find a way to allow chains to detach from the rods.

Chapter 6

Summary and future work

In this thesis I have presented three research projects, hopefully contributing to a better understanding of the fatigue, fracture and damage of synthetic polymers. One common theme throughout this work has been the role played by dissipation mechanisms in controlling fracture in these materials.

In chapter 3, we examined the energy dissipated through viscous effects and the energy available for driving crack growth under cyclic loading. In particular, energy dissipation is controlled by an interplay of three time scales: the material relaxation time, the timescale associated with crack propagation (i.e., crack speed) and the loading frequency. By tracking the stress history of material points around the crack tip under concurrent crack propagation and cyclic loading, we derived an integral equation governing crack speed within a loading cycle.

In chapter 4, we considered materials with rate-independent dissipation. We discussed the use of an operational metric to measure the apparent toughness of synthetic polymers and provided guidelines for interpreting the outcome of pure shear tests under monotonic loading.

In chapter 5, we have outlined a modeling framework for analyzing the concurrent viscoelastic and damage-induced dissipation in carbon fibers reinforced polymers.

Further research is necessary to expand on the results of this dissertation. First, while viscoelasticity captures the dominant behavior of the fatigue fracture of synthetic polymers, considering second order effects like Mullins softening and strain-induced crystallization are needed to obtain a complete picture. Our work also highlighted the importance of characterizing the strain

and stress fields during cyclic crack propagation, which suggest focusing on both computational and experimental work in the future. Regarding chapter 4, an important limitation is due to the use of a cohesive zone model to control crack growth in our simulations. This necessarily restricts our understanding of crack initiation because it ignores the complexities of the energy transfer from the macroscopic to the molecular scales. If we wish to better understand crack initiation, I believe it is necessary to adopt a multi-scale approach. Finally, the limitations and future directions for the work presented in chapter 5 are thoroughly discussed therein. It would start with experimental investigations to characterize the softening and hysteresis upon cyclic stretching with increasing magnitude, including experiments to probe the induced anisotropy. Then, based on our observations of the matrix-fibers interface, extensions within the proposed modeling framework should be implemented to compare with these experiments.

Bibliography

- [1] H. Ahmad, A. A. Markina, M. V. Porotnikov, and F. Ahmad. A review of carbon fiber materials in automotive industry. volume 971. IOP Publishing Ltd, 11 2020.
- [2] Yuki Akagi, Hayato Sakurai, Jian Ping Gong, Ung-il Chung, and Takamasa Sakai. Fracture energy of polymer gels with controlled network structures. *The Journal of chemical physics*, 139(14), 2013.
- [3] Saleh Alzugaibi, Julien Caillard, Davide Colombo, and Rong Long. Energy dissipation during crack growth in rubbers with mullins softening. *Advanced Engineering Materials*, page 2402173, 2025.
- [4] Ted L Anderson. *Fracture mechanics: fundamentals and applications*. CRC press, 2017.
- [5] Ellen M Arruda and Mary C Boyce. A three-dimensional constitutive model for the large stretch behavior of rubber elastic materials. *Journal of the Mechanics and Physics of Solids*, 41(2):389–412, 1993.
- [6] Ruobing Bai, Jiawei Yang, and Zhigang Suo. Fatigue of hydrogels. *European Journal of Mechanics-A/Solids*, 74:337–370, 2019.
- [7] Tristan Baumberger, Christiane Caroli, and David Martina. Fracture of a biopolymer gel as a viscoplastic disentanglement process. *The European Physical Journal E*, 21:81–89, 2006.
- [8] George I Bell. Models for the specific adhesion of cells to cells: a theoretical framework for adhesion mediated by reversible bonds between cell surface molecules. *Science*, 200(4342):618–627, 1978.
- [9] Shlomo Breuer and E Turan Onat. On the determination of free energy in linear viscoelastic solids. *Zeitschrift für angewandte Mathematik und Physik ZAMP*, 15:184–191, 1964.
- [10] Hugh R Brown. A model of the fracture of double network gels. *Macromolecules*, 40(10):3815–3818, 2007.
- [11] Roger Brown. *Physical testing of rubber*. Springer Science & Business Media, 2006.
- [12] F Bueche. Mullins effect and rubber–filler interaction. *Journal of applied polymer Science*, 5(15):271–281, 1961.
- [13] INGLIS CE. Stresses in a plate due to the presence of cracks and sharp corners. *Trans Inst Naval Archit*, 55:219–241, 1913.

- [14] Manoj K Chaudhury. Rate-dependent fracture at adhesive interface. *The Journal of Physical Chemistry B*, 103(31):6562–6566, 1999.
- [15] Laurent Chazeau, J-M Chenal, C Gauthier, J Kallungal, and J Caillard. About the influence of materials parameters on the ultimate and fatigue properties of elastomers. *Fatigue Crack Growth in Rubber Materials*, pages 297–329, 2020.
- [16] Richard M Christensen. *Theory of viscoelasticity - an introduction*. Academic Press, 2 edition, 1982.
- [17] RM Christensen. A rate-dependent criterion for crack growth. *International Journal of Fracture*, 15:3–21, 1979.
- [18] Costantino Creton and Matteo Ciccotti. Fracture and adhesion of soft materials: a review. *Reports on Progress in Physics*, 79(4):046601, 2016.
- [19] Antonella Cristiano, Alba Marcellan, Bert J Keestra, Paul Steeman, and Costantino Creton. Fracture of model polyurethane elastomeric networks. *Journal of Polymer Science Part B: Polymer Physics*, 49(5):355–367, 2011.
- [20] PIERRE-GILLES de Gennes. Soft adhesives. *Langmuir*, 12(19):4497–4500, 1996.
- [21] Quentin Demassieux. *Structural changes in the process zone of a cyclic fatigue crack in filled natural rubber*. PhD thesis, Paris 6, 2016.
- [22] J Diani and Patrick Le Tallec. A fully equilibrated microsphere model with damage for rubberlike materials. *Journal of the Mechanics and Physics of Solids*, 124:702–713, 2019.
- [23] Julie Diani, Mathias Brieu, and JM Vacherand. A damage directional constitutive model for mullins effect with permanent set and induced anisotropy. *European Journal of Mechanics-A/Solids*, 25(3):483–496, 2006.
- [24] Julie Diani, Bruno Fayolle, and Pierre Gilormini. A review on the mullins effect. *European Polymer Journal*, 45(3):601–612, 2009.
- [25] Rodrigo Diaz, Julie Diani, and Pierre Gilormini. Physical interpretation of the mullins softening in a carbon-black filled sbr. *Polymer*, 55(19):4942–4947, 2014.
- [26] Phuong Anh Vo Dong, Catherine Azzaro-Pantel, and Anne Laure Cadene. Economic and environmental assessment of recovery and disposal pathways for cfrp waste management. *Resources, Conservation and Recycling*, 133:63–75, 6 2018.
- [27] Etienne Ducrot, Yulan Chen, Markus Bulters, Rint P Sijbesma, and Costantino Creton. Toughening elastomers with sacrificial bonds and watching them break. *Science*, 344(6180):186–189, 2014.
- [28] T. Alshuth F. Abraham and S. Jerrams. Dependence on mean stress and stress amplitude of fatigue life of epdm elastomers. *Plastics, Rubber and Composites*, 30(9):421–425, 2001.
- [29] JD Ferry. *Viscoelastic Properties of Polymers*, volume 264. Wiley, 1980.

- [30] Tobias Gehling, Jacopo Schieppati, Winoj Balasooriya, Roman Christopher Kerschbaumer, and Gerald Pinter. Fatigue behavior of elastomeric components: A review of the key factors of rubber formulation, manufacturing, and service conditions. *Polymer Reviews*, pages 1–42, 2023.
- [31] Alan N Gent. *Engineering with rubber: how to design rubber components*. Carl Hanser Verlag GmbH Co KG, 2012.
- [32] AN Gent. Crystallization and the relaxation of stress in stretched natural rubber vulcanizates. *Transactions of the Faraday Society*, 50:521–533, 1954.
- [33] AN Gent. Compression of rubber blocks. *Rubber chemistry and technology*, 67(3):549–558, 1994.
- [34] AN Gent. Adhesion and strength of viscoelastic solids. is there a relationship between adhesion and bulk properties? *Langmuir*, 12(19):4492–4496, 1996.
- [35] AN Gent, PB Lindley, and A Gt Thomas. Cut growth and fatigue of rubbers. i. the relationship between cut growth and fatigue. *Rubber Chemistry and Technology*, 38(2):292–300, 1965.
- [36] AN Gent, PB Lindley, and AG Thomas. Cut growth and fatigue of rubbers. i. the relationship between cut growth and fatigue. *Journal of Applied Polymer Science*, 8(1):455–466, 1964.
- [37] Christophe Geuzaine and Jean-François Remacle. Gmsh: A 3-d finite element mesh generator with built-in pre-and post-processing facilities. *International journal for numerical methods in engineering*, 79(11):1309–1331, 2009.
- [38] JM Golden. Minimal states and maximum free energies of materials with memory. *Computers & structures*, 84(17-18):1115–1124, 2006.
- [39] Jian Ping Gong. Why are double network hydrogels so tough? *Soft Matter*, 6(12):2583–2590, 2010.
- [40] Jian Ping Gong, Yoshinori Katsuyama, Takayuki Kurokawa, and Yoshihito Osada. Double-network hydrogels with extremely high mechanical strength. *Advanced materials*, 15(14):1155–1158, 2003.
- [41] GAC Graham. The correspondence principle of linear viscoelasticity theory for mixed boundary value problems involving time-dependent boundary regions. *Quarterly of Applied Mathematics*, 26(2):167–174, 1968.
- [42] GAC Graham. Two extending crack problems in linear viscoelasticity theory. *Quarterly of Applied Mathematics*, 27(4):497–507, 1970.
- [43] GAC Graham and JM Golden. The generalized partial correspondence principle in linear viscoelasticity. *Quarterly of applied mathematics*, 46(3):527–538, 1988.
- [44] François Grasland. *Vieillissement du caoutchouc naturel par thermo-oxydation: Etudes de ses conséquences sur la cristallisation sous déformation, la fissuration et la rupture*. PhD thesis, Université de Lyon, 2018.

- [45] HW Greensmith. Rupture of rubber. vii. effect of rate of extension in tensile tests. *Journal of applied polymer science*, 3(8):175–182, 1960.
- [46] JA Greenwood. The theory of viscoelastic crack propagation and healing. *Journal of Physics D: Applied Physics*, 37(18):2557, 2004.
- [47] Alan Arnold Griffith. Vi. the phenomena of rupture and flow in solids. *Philosophical transactions of the royal society of london. Series A, containing papers of a mathematical or physical character*, 221(582-593):163–198, 1921.
- [48] Q. Guo, F. Zaïri, C. Ovalle Rodas, and X. Guo. Constitutive modeling of the cyclic dissipation in thin and thick rubber specimens. *ZAMM-Journal of Applied Mathematics and Mechanics/Zeitschrift für Angewandte Mathematik und Mechanik*, 98(10):1878–1899, 2018.
- [49] Qiang Guo, Julien Caillard, Davide Colombo, and Rong Long. Dynamic effect in the fatigue fracture of viscoelastic solids. *Extreme Mechanics Letters*, 54:101726, 2022.
- [50] Morton E Gurtin. On the energy release rate in quasi-static elastic crack propagation. *Journal of Elasticity*, 9(2):187–195, 1979.
- [51] Morton E Gurtin. Thermodynamics and the griffith criterion for brittle fracture. *International Journal of Solids and Structures*, 15(7):553–560, 1979.
- [52] Morton E Gurtin, Eliot Fried, and Lallit Anand. *The mechanics and thermodynamics of continua*. Cambridge university press, 2010.
- [53] Morton E Gurtin and William J Hrusa. On energies for nonlinear viscoelastic materials of single-integral type. *Quarterly of applied mathematics*, 46(2):381–392, 1988.
- [54] Gert Heinrich and Manfred Klüppel. Basic mechanisms and predictive testing of tire-road abrasion. In *Degradation of Elastomers in Practice, Experiments and Modeling*, pages 1–14. Springer, 2022.
- [55] Gerhard A Holzapfel. Nonlinear solid mechanics: a continuum approach for engineering science, 2002.
- [56] Chung-Yuen Hui, Da-Ben Xu, and Edward J Kramer. A fracture model for a weak interface in a viscoelastic material (small scale yielding analysis). *Journal of applied physics*, 72(8):3294–3304, 1992.
- [57] Chung-Yuen Hui, Bangguo Zhu, and Rong Long. Steady state crack growth in viscoelastic solids: A comparative study. *Journal of the Mechanics and Physics of Solids*, 159:104748, 2022.
- [58] CY Hui, A Ruina, R Long, and A Jagota. Cohesive zone models and fracture. *The Journal of Adhesion*, 87(1):1–52, 2011.
- [59] Johann R Katz. X-ray spectrography of polymers and in particular those having a rubber-like extensibility. *Transactions of the Faraday Society*, 32:77–94, 1936.
- [60] Christoph Keplinger, Jeong-Yun Sun, Choon Chiang Foo, Philipp Rothemund, George M Whitesides, and Zhigang Suo. Stretchable, transparent, ionic conductors. *Science*, 341(6149):984–987, 2013.

- [61] Dong Chan Kim, Hyung Joon Shim, Woongchan Lee, Ja Hoon Koo, and Dae-Hyeong Kim. Material-based approaches for the fabrication of stretchable electronics. *Advanced Materials*, 32(15):1902743, 2020.
- [62] Reinhold Kipscholl and Radek Stoček. Degradation of tires during intended usage. In *Degradation of Elastomers in Practice, Experiments and Modeling*, pages 185–207. Springer, 2022.
- [63] Christopher J. Kloxin and Christopher N. Bowman. Covalent adaptable networks: Smart, reconfigurable and responsive network systems. *Chemical Society Reviews*, 42:7161–7173, 8 2013.
- [64] M Klüppel. Evaluation of viscoelastic master curves of filled elastomers and applications to fracture mechanics. *Journal of Physics: Condensed Matter*, 21(3):035104, 2008.
- [65] Wolfgang G Knauss. A review of fracture in viscoelastic materials. *International Journal of Fracture*, 196:99–146, 2015.
- [66] Wolfgang Gustav Knauss. Stresses in an infinite strip containing a semi-infinite crack. *Journal of Applied Mechanics*, 33:356–362, 1966.
- [67] James K Knowles. A note on the energy release rate in quasi-static elastic crack propagation. *SIAM Journal on Applied Mathematics*, 41(3):401–412, 1981.
- [68] Werner Kuhn and Franz Grün. Statistical behavior of the single chain molecule and its relation to the statistical behavior of assemblies consisting of many chain molecules. *Journal of polymer science*, 1(3):183–199, 1946.
- [69] GJ Lake. Fatigue and fracture of elastomers. *Rubber chemistry and technology*, 68(3):435–460, 1995.
- [70] GJ Lake. Application of fracture mechanics to crack growth in rubber-cord laminates. *Rubber chemistry and technology*, 74(3):509–524, 2001.
- [71] GJ Lake and PB Lindley. Cut growth and fatigue of rubbers. ii. experiments on a noncrys-tallizing rubber. *Journal of Applied Polymer Science*, 8(2):707–721, 1964.
- [72] GJ Lake and PB Lindley. The mechanical fatigue limit for rubber. *Journal of Applied Polymer Science*, 9(4):1233–1251, 1965.
- [73] GJ Lake and AG Thomas. The strength of highly elastic materials. *Proceedings of the Royal Society of London. Series A. Mathematical and Physical Sciences*, 300(1460):108–119, 1967.
- [74] Samuel Lamont and Franck J Vernerey. A transient microsphere model for nonlinear viscoelas-ticity in dynamic polymer networks. *Journal of Applied Mechanics*, 89(1):011009, 2022.
- [75] Samuel C Lamont, Jason Mulderrig, Nikolaos Bouklas, and Franck J Vernerey. Rate-dependent damage mechanics of polymer networks with reversible bonds. *Macromolecules*, 54(23):10801–10813, 2021.
- [76] Shawn R Lavoie, Rong Long, and Tian Tang. A rate-dependent damage model for elastomers at large strain. *Extreme Mechanics Letters*, 8:114–124, 2016.

- [77] Bruce P Lee and Shari Konst. Novel hydrogel actuator inspired by reversible mussel adhesive protein chemistry. *Adv. Mater.*, 26(21):3415–3419, 2014.
- [78] Geoffrey M Lewis, Cailin A Buchanan, Krutarth D Jhaveri, John L Sullivan, Jarod C Kelly, Sujit Das, Alan I Taub, and Gregory A Keoleian. Green principles for vehicle lightweighting. *Environmental science & technology*, 53(8):4063–4077, 2019.
- [79] Xueyu Li, Kunpeng Cui, Takayuki Kurokawa, Ya Nan Ye, Tao Lin Sun, Chengtao Yu, Costantino Creton, and Jian Ping Gong. Effect of mesoscale phase contrast on fatigue-delaying behavior of self-healing hydrogels. *Science advances*, 7(16):eabe8210, 2021.
- [80] Xueyu Li, Kunpeng Cui, Tao Lin Sun, Lingpu Meng, Chengtao Yu, Liangbin Li, Costantino Creton, Takayuki Kurokawa, and Jian Ping Gong. Mesoscale bicontinuous networks in self-healing hydrogels delay fatigue fracture. *Proceedings of the National Academy of Sciences*, 117(14):7606–7612, 2020.
- [81] PB Lindley. Relation between hysteresis and the dynamic crack growth resistance of natural rubber. *International Journal of Fracture*, 9:449–462, 1973.
- [82] PB Lindley. Non-relaxing crack growth and fatigue in a non-crystallizing rubber. *Rubber Chemistry and Technology*, 47(5):1253–1264, 1974.
- [83] Yiping Liu, Ken Gall, Martin L Dunn, Alan R Greenberg, and Julie Diani. Thermomechanics of shape memory polymers: uniaxial experiments and constitutive modeling. *International Journal of Plasticity*, 22(2):279–313, 2006.
- [84] Rong Long and Chung-Yuen Hui. Crack tip fields in soft elastic solids subjected to large quasi-static deformation—a review. *Extreme Mechanics Letters*, 4:131–155, 2015.
- [85] Rong Long and Chung-Yuen Hui. Fracture toughness of hydrogels: measurement and interpretation. *Soft Matter*, 12(39):8069–8086, 2016.
- [86] Rong Long, Chung-Yuen Hui, Jian Ping Gong, and Eran Bouchbinder. The fracture of highly deformable soft materials: A tale of two length scales. *Annual Review of Condensed Matter Physics*, 12:71–94, 2021.
- [87] Guillaume Lostec. Post-processing tutorial. https://github.com/Guillaume-Lostec/Abaqus_Python_Plottin/.
- [88] Guillaume Lostec, Julien Caillard, Davide Colombo, and Rong Long. A theory of fatigue fracture in viscoelastic solids. *Journal of the Mechanics and Physics of Solids*, page 106047, 2025.
- [89] Guillaume Lostec, Louis Corcoran, Hongxuan Chen, Wei Zhang, Rong Long, and Yinghua Jin. Investigating the mechanical failure mechanisms of a novel cfrp composite to inform computational models. In *Nondestructive Characterization and Monitoring of Advanced Materials, Aerospace, Civil Infrastructure, and Transportation XVIII*, volume 12950, pages 214–224. SPIE, 2024.
- [90] Yunwei Mao, Brandon Talamini, and Lallit Anand. Rupture of polymers by chain scission. *Extreme Mechanics Letters*, 13:17–24, 2017.

- [91] Gilles Marckmann, Erwan Verron, Laurent Gornet, Gregory Chagnon, Pierre Charrier, and Patrice Fort. A theory of network alteration for the mullins effect. *Journal of the Mechanics and Physics of Solids*, 50(9):2011–2028, 2002.
- [92] James E Mark, Burak Erman, and Mike Roland. *The science and technology of rubber*. Academic press, 2013.
- [93] WV Mars and A Fatemi. A literature survey on fatigue analysis approaches for rubber. *International Journal of fatigue*, 24(9):949–961, 2002.
- [94] WV Mars and A Fatemi. Factors that affect the fatigue life of rubber: a literature survey. *Rubber Chemistry and Technology*, 77(3):391–412, 2004.
- [95] Yannick Merckel. *Experimental characterization and modeling of the mechanical behavior of filled rubbers under cyclic loading conditions*. PhD thesis, Ecole Centrale de Lille, 2012.
- [96] C Miehe, Serdar Göktepe, and F20965751091 Lulei. A micro-macro approach to rubber-like materials—part i: the non-affine micro-sphere model of rubber elasticity. *Journal of the Mechanics and Physics of Solids*, 52(11):2617–2660, 2004.
- [97] Pierre Millereau, Etienne Ducrot, Jess M Clough, Meredith E Wiseman, Hugh R Brown, Rint P Sijbesma, and Costantino Creton. Mechanics of elastomeric molecular composites. *Proceedings of the National Academy of Sciences*, 115(37):9110–9115, 2018.
- [98] AH Muhr and AD Roberts. Rubber abrasion and wear. *Wear*, 158(1-2):213–228, 1992.
- [99] Leonard Mullins. Softening of rubber by deformation. *Rubber chemistry and technology*, 42(1):339–362, 1969.
- [100] Samy Mzabi. *Caractérisation et analyse des mécanismes de fracture en fatigue des élastomères chargés*. PhD thesis, Paris 6, 2010.
- [101] Samy Mzabi, Daniel Berghezan, Stéphane Roux, Francois Hild, and Costantino Creton. A critical local energy release rate criterion for fatigue fracture of elastomers. *Journal of Polymer Science Part B: Polymer Physics*, 49(21):1518–1524, 2011.
- [102] National Highway Traffic Safety Administration and others. Corporate average fuel economy standards for model years 2024–2026 passenger cars and light trucks. *Federal Register*, 87.
- [103] Ray W Ogden and David George Roxburgh. A pseudo-elastic model for the mullins effect in filled rubber. *Proceedings of the Royal Society of London. Series A: Mathematical, Physical and Engineering Sciences*, 455(1988):2861–2877, 1999.
- [104] Egon Orowan. Fracture and strength of solids. *Reports on progress in physics*, 12(1):185, 1949.
- [105] Rozaini Othman, M Hisyam Basri, Iswadi Ismail, Muhammad Arif Ab, Hamid Pahmi, Mahamad Hisyam, Mahamad Basri, Hazim Sharudin, and Abdul Rahman Hemdi. Application of carbon fiber reinforced plastics in automotive industry: A review. *Journal of Mechanical Manufacturing*, 1, 2019.

- [106] Dervis Ozkan, Mustafa Sabri Gok, and Abdullah Cahit Karaoglanli. Carbon Fiber Reinforced Polymer (CFRP) Composite Materials, Their Characteristic Properties, Industrial Application Areas and Their Machinability, volume 124, pages 235–253. Springer, 2020.
- [107] BNJ Persson and EA Brener. Crack propagation in viscoelastic solids. Physical Review E, 71(3):036123, 2005.
- [108] S.J. Pickering. Recycling technologies for thermoset composite materials - current status. Composites Part A: Applied Science and Manufacturing, 37:1206 –1215, 2006.
- [109] Thomas R. Pozegic, Samantha Huntley, Marco L. Longana, Suihua He, R. M. Indrachapa Bandara, Simon G. King, and Ian Hamerton. Improving dispersion of recycled discontinuous carbon fibres to increase fibre throughput in the hiperdif process. Materials, 13, 4 2020.
- [110] Yuan Qi, Julien Caillard, and Rong Long. Fracture toughness of soft materials with rate-independent hysteresis. Journal of the Mechanics and Physics of Solids, 118:341–364, 2018.
- [111] Yuan Qi, Zhanan Zou, Jianliang Xiao, and Rong Long. Mapping the nonlinear crack tip deformation field in soft elastomer with a particle tracking method. Journal of the Mechanics and Physics of Solids, 125:326–346, 2019.
- [112] James R Rice. A path independent integral and the approximate analysis of strain concentration by notches and cracks. Journal on Applied Mechanics, 35(2):379–386, 1968.
- [113] JR Rice. Discussion: “stresses in an infinite strip containing a semi-infinite crack” (knauss, wg, 1966, asme j. appl. mech., 33, pp. 356–362). Journal of Applied Mechanics, 34:248–249, 1967.
- [114] RS Rivlin and A Gr Thomas. Rupture of rubber. i. characteristic energy for tearing. Journal of polymer science, 10(3):291–318, 1953.
- [115] David Roucou, Julie Diani, Mathias Brieu, and Davide Colombo. Experimental identification of fracture toughness of a carbon black-filled styrene butadiene rubber undergoing energy dissipation by mullins softening. Mechanics of Materials, 151:103645, 2020.
- [116] David Roucou, Julie Diani, Mathias Brieu, and Armel Mbiakop-Ngassa. Critical strain energy release rate for rubbers: single edge notch tension versus pure shear tests. International Journal of Fracture, 216:31–39, 2019.
- [117] Pierre Rublon. Etude expérimentale multi-échelle de la propagation de fissure de fatigue dans le caoutchouc naturel. PhD thesis, Ecole Centrale de Nantes (ECN), 2013.
- [118] F Saulnier, Thierry Ondarçuhu, A Aradian, and Elie Raphaël. Adhesion between a viscoelastic material and a solid surface. Macromolecules, 37(3):1067–1075, 2004.
- [119] Richard A Schapery. A theory of crack initiation and growth in viscoelastic media: I. theoretical development. International Journal of fracture, 11:141–159, 1975.
- [120] Richard A Schapery. Correspondence principles and a generalized j integral for large deformation and fracture analysis of viscoelastic media. International journal of fracture, 25:195–223, 1984.

- [121] Jacopo Schieppati, Bernd Schrittesser, Alfred Wondracek, Stefan Robin, Armin Holzner, and Gerald Pinter. Effect of mechanical loading history on fatigue crack growth of non-crystallizing rubber. *Engineering Fracture Mechanics*, 257:108010, 2021.
- [122] Tong Shen and Franck J Vernerey. Rate-dependent fracture of transient networks. *Journal of the Mechanics and Physics of Solids*, 143:104028, 2020.
- [123] Juliette Slootman, Victoria Waltz, C Joshua Yeh, Christoph Baumann, Robert Göstl, Jean Comtet, and Costantino Creton. Quantifying rate-and temperature-dependent molecular damage in elastomer fracture. *Physical Review X*, 10(4):041045, 2020.
- [124] Shankar Lalitha Sridhar and Franck J Vernerey. Mechanics of transiently cross-linked nematic networks. *Journal of the Mechanics and Physics of Solids*, 141:104021, 2020.
- [125] Franziska Stadlbauer, Thomas Koch, Vasiliki-Maria Archodoulaki, Florian Planitzer, Wolfgang Fidi, and Armin Holzner. Influence of experimental parameters on fatigue crack growth and heat build-up in rubber. *Materials*, 6(12):5502–5516, 2013.
- [126] Radek Stoček. Some revisions of fatigue crack growth characteristics of rubber. *Fatigue crack growth in rubber materials: experiments and modelling*, pages 1–18, 2021.
- [127] Jeong-Yun Sun, Xuanhe Zhao, Widusha RK Illeperuma, Ovijit Chaudhuri, Kyu Hwan Oh, David J Mooney, Joost J Vlassak, and Zhigang Suo. Highly stretchable and tough hydrogels. *Nature*, 489(7414):133–136, 2012.
- [128] Tao Lin Sun, Takayuki Kurokawa, Shinya Kuroda, Abu Bin Ihsan, Taigo Akasaki, Koshiro Sato, Md Anamul Haque, Tasuku Nakajima, and Jian Ping Gong. Physical hydrogels composed of polyampholytes demonstrate high toughness and viscoelasticity. *Nature materials*, 12(10):932–937, 2013.
- [129] H Tada, PC Paris, and GR Irwin. The stress analysis of cracks handbook, del research corporation, st. Louis, Missouri, 1973.
- [130] F Tanaka and SF Edwards. Viscoelastic properties of physically crosslinked networks. 1. transient network theory. *Macromolecules*, 25(5):1516–1523, 1992.
- [131] Yoshimi Tanaka. A local damage model for anomalous high toughness of double-network gels. *Europhysics Letters*, 78(5):56005, 2007.
- [132] Yoshimi Tanaka, Rikimaru Kuwabara, Yang-Ho Na, Takayuki Kurokawa, Jian Ping Gong, and Yoshihito Osada. Determination of fracture energy of high strength double network hydrogels. *The Journal of Physical Chemistry B*, 109(23):11559–11562, 2005.
- [133] AG Thomas. Rupture of rubber. ii. the strain concentration at an incision. *Journal of Polymer science*, 18(88):177–188, 1955.
- [134] LRG Treloar. The elasticity of a network of long-chain molecules.—iii. *Transactions of the Faraday Society*, 42:83–94, 1946.
- [135] United States Department of Transportation. National highway transportation safety administration, 4 2022.

- [136] Franck J Vernerey, Rong Long, and Roberto Brighenti. A statistically-based continuum theory for polymers with transient networks. *Journal of the Mechanics and Physics of Solids*, 107:1–20, 2017.
- [137] Shi-Qing Wang, Zehao Fan, Chaitanya Gupta, Asal Siavoshani, and Travis Smith. Fracture behavior of polymers in plastic and elastomeric states. *Macromolecules*, 57(9):3875–3900, 2024.
- [138] Xiao Wang and Wei Hong. Pseudo-elasticity of a double network gel. *Soft Matter*, 7(18):8576–8581, 2011.
- [139] Rebecca E Webber, Costantino Creton, Hugh R Brown, and Jian Ping Gong. Large strain hysteresis and mullins effect of tough double-network hydrogels. *Macromolecules*, 40(8):2919–2927, 2007.
- [140] George M Whitesides. Soft robotics. *Angewandte Chemie International Edition*, 57(16):4258–4273, 2018.
- [141] Tianhao Yang, Kenneth M Liechti, and Rui Huang. A multiscale cohesive zone model for rate-dependent fracture of interfaces. *Journal of the Mechanics and Physics of Solids*, 145:104142, 2020.
- [142] Xingwei Yang, Michael J Wald, Ryan Birringer, Jonathan Kemling, Aaron Hedegaard, John Martin, Jason Clapper, and Rong Long. Intrinsic fracture toughness of a soft viscoelastic adhesive. *Journal of the Mechanics and Physics of Solids*, 192:105797, 2024.
- [143] Shridhar Yarlagadda, Joseph Deitzel, Dirk Heider, John Tierney, and John W Gillespie. Tailorable universal feedstock for forming (tuff): Overview and performance. *Society for the Advancement of Material and Process Engineers Conference Proceedings*, 2019.
- [144] Kazunori Yasuda, Nobuto Kitamura, Jian Ping Gong, Kazunobu Arakaki, Hyuck Joon Kwon, Shin Onodera, Yong Mei Chen, Takayuki Kurokawa, Fuminori Kanaya, Yoshihiro Ohmiya, et al. A novel double-network hydrogel induces spontaneous articular cartilage regeneration in vivo in a large osteochondral defect. *Macromolecular bioscience*, 9(4):307–316, 2009.
- [145] Luxia Yu, Zepeng Lei, Xiaohao Sun, Peiran Ding, Aaron Wesche, Yinghua Jin, Wei Zhang, and Rong Long. Rapid fabrication of fiber-reinforced polyimine composites with reprocessability, repairability, and recyclability. *ACS Applied Polymer Materials*, 3:5808–5817, 11 2021.
- [146] Alan T Zehnder. *Fracture mechanics*, volume 62. Springer Science & Business Media, 2012.
- [147] Alan T. Zehnder. *Fracture Mechanics*. Springer, 2012.
- [148] HP Zhang, J Niemczura, G Dennis, K Ravi-Chandar, and M Marder. Toughening effect of strain-induced crystallites in natural rubber. *Physical review letters*, 102(24):245503, 2009.
- [149] Huan Zhang, Arthur K Scholz, Jordan de Crevoisier, Daniel Berghezan, Theyencheri Narayanan, Edward J Kramer, and Costantino Creton. Nanocavitation around a crack tip in a soft nanocomposite: A scanning microbeam small angle x-ray scattering study. *Journal of Polymer Science Part B: Polymer Physics*, 53(6):422–429, 2015.

- [150] Teng Zhang, Shaoting Lin, Hyunwoo Yuk, and Xuanhe Zhao. Predicting fracture energies and crack-tip fields of soft tough materials. *Extreme Mechanics Letters*, 4:1–8, 2015.
- [151] Qian Zhao, H Jerry Qi, and Tao Xie. Recent progress in shape memory polymer: New behavior, enabling materials, and mechanistic understanding. *Progress in Polymer Science*, 49:79–120, 2015.
- [152] Xuanhe Zhao. A theory for large deformation and damage of interpenetrating polymer networks. *Journal of the Mechanics and Physics of Solids*, 60(2):319–332, 2012.
- [153] Xuanhe Zhao. Multi-scale multi-mechanism design of tough hydrogels: building dissipation into stretchy networks. *Soft matter*, 10(5):672–687, 2014.
- [154] Yong Zheng, Takahiro Matsuda, Tasuku Nakajima, Wei Cui, Ye Zhang, Chung-Yuen Hui, Takayuki Kurokawa, and Jian Ping Gong. How chain dynamics affects crack initiation in double-network gels. *Proceedings of the National Academy of Sciences*, 118(49):e2111880118, 2021.
- [155] Xian-Kui Zhu and James A Joyce. Review of fracture toughness (g , k , j , ctod , ctoa) testing and standardization. *Engineering fracture mechanics*, 85:1–46, 2012.

Appendix A

Cohesive zone model and the fracture energy

To relate Γ_0 to the cohesive zone for an actively propagating crack, we start with the volumetric integral of the stress power density $\mathbf{S} : d\mathbf{E}/dt$. Using the identity that $\mathbf{S} : d\mathbf{E}/dt = \mathbf{P} : d\mathbf{F}/dt$ and the chain rule that $\nabla_{\mathbf{X}} \cdot (\mathbf{P} \cdot (d\mathbf{u}/dt)) = \mathbf{P} : d\mathbf{F}/dt + (\nabla_{\mathbf{X}} \cdot \mathbf{P}) \cdot (d\mathbf{u}/dt)$, we obtain

$$\int_{\Omega} \mathbf{S} : \frac{d\mathbf{E}}{dt} d\mathcal{V} = \int_{\Omega} \mathbf{P} : \frac{d\mathbf{F}}{dt} d\mathcal{V} = \int_{\Omega} \nabla_{\mathbf{X}} \cdot (\mathbf{P} \cdot \frac{d\mathbf{u}}{dt}) d\mathcal{V}, \quad (\text{A.1})$$

where we have imposed the equilibrium equation in the absence of body forces, i.e., $(\nabla_{\mathbf{X}} \cdot \mathbf{P}) = \mathbf{0}$.

Applying the divergence theorem to Eq.(A.1) and using $\mathbf{t} = \mathbf{P} \cdot \mathbf{n}$, we have

$$\int_{\Omega} \mathbf{S} : \frac{d\mathbf{E}}{dt} d\mathcal{V} = \int_{\partial\Omega} \mathbf{t} \cdot \frac{d\mathbf{u}}{dt} dS + \int_{A_c} \left(\mathbf{t}^+ \cdot \frac{d\mathbf{u}^+}{dt} + \mathbf{t}^- \cdot \frac{d\mathbf{u}^-}{dt} \right) dS, \quad (\text{A.2})$$

where A_c denotes the cohesive zone area, \mathbf{t}^+ and \mathbf{t}^- are traction vectors on the two opposing surfaces of the cohesive zone, and \mathbf{u}^+ and \mathbf{u}^- are the corresponding displacements of the cohesive zone surfaces. Note that we have applied the traction-free condition on the crack surfaces. Given that $\mathbf{t}^+ = -\mathbf{t}^-$, we define the cohesive separation vector as $\mathbf{u}_c = \mathbf{u}^+ - \mathbf{u}^-$ and denote the cohesive traction as $\mathbf{t}_c = \mathbf{t}^- = -\mathbf{t}^+$. This definition allows us to maintain $\mathbf{t}_c \cdot d\mathbf{u}_c \geq 0$. Using this notation, Eq.(A.2) can be rewritten as

$$\int_{\Omega} \mathbf{S} : \frac{d\mathbf{E}}{dt} d\mathcal{V} = \int_{\partial\Omega} \mathbf{t} \cdot \frac{d\mathbf{u}}{dt} dS - \int_{A_c} \mathbf{t}_c \cdot \frac{d\mathbf{u}_c}{dt} dS, \quad (\text{A.3})$$

Comparing Eq.(A.3) and Eq.(5.5), we identify

$$\int_{A_c} \mathbf{t}_c \cdot \frac{d\mathbf{u}_c}{dt} dS = \int_C \Gamma_0(\xi) \frac{dv}{dt} d\xi. \quad (\text{A.4})$$

Since we have assumed planar crack surfaces and self-similar growth of the crack front \mathcal{C} , the cohesive zone A_c should be on the same plane of the crack surface. At any given time, we can parameterize A_c using two coordinates: ξ and ζ that are along and perpendicular to the crack front \mathcal{C} , respectively. For an actively propagating crack, the cohesive zone is fully developed and is independent of the stress and strain fields in the bulk solid. Therefore, both \mathbf{t}_c and \mathbf{u}_c depend on the position relative to the crack front, i.e., $\mathbf{t}_c(\xi, \zeta^*)$ and $\mathbf{u}_c(\xi, \zeta^*)$ (see Fig.(3.2b)), where $\zeta^* = \zeta - \zeta_0$ and ζ_0 denotes the crack front location at a given ξ . Note that ζ_0 is time dependent due to crack propagation. Therefore, the left hand side of Eq.(A.4) can be written as

$$\int_{A_c} \mathbf{t}_c \cdot \frac{d\mathbf{u}_c}{dt} dS = \int_{\mathcal{C}} \int_0^{\zeta_m} \mathbf{t}_c \cdot \frac{d\mathbf{u}_c}{dt} d\zeta^* d\xi, \quad (\text{A.5})$$

where ζ_m denotes the maximum extent of cohesive zone and corresponds to the point where there is no cohesive separation (i.e., $\mathbf{u}_c = \mathbf{0}$). Using $d\mathbf{u}_c/dt = (\partial\mathbf{u}_c/\partial\zeta^*)(d\zeta^*/dt)$ and $d\zeta^*/dt = -d\zeta_0/dt$, we can further write Eq.(A.5) as

$$\int_{A_c} \mathbf{t}_c \cdot \frac{d\mathbf{u}_c}{dt} dS = \int_{\mathcal{C}} \left(\int_0^{\zeta_m} \mathbf{t}_c \cdot \frac{\partial\mathbf{u}_c}{\partial\zeta^*} d\zeta^* \right) \left(-\frac{d\zeta_0}{dt} \right) d\xi. \quad (\text{A.6})$$

We recognize that $d\zeta_0/dt = dv/dt$ (see Fig.(3.1)). Additionally, the assumption of uniform Γ_0 and cohesive zone along the crack front \mathcal{C} implies that $\Gamma_0(\xi) = \Gamma_0$ and $\mathbf{u}_c(\xi, \zeta^*) = \mathbf{u}_c(\zeta^*)$. Therefore, we have

$$\Gamma_0 = - \int_0^{\zeta_m} \mathbf{t}_c \cdot \frac{d\mathbf{u}_c}{d\zeta^*} d\zeta^* = \int_0^{\mathbf{u}_c^{max}} \mathbf{t}_c \cdot d\mathbf{u}_c. \quad (\text{A.7})$$

where $\mathbf{u}_c^{max} = \mathbf{u}_c(\zeta^* = 0)$ is the cohesive separation at the crack front. This equation shows that Γ_0 is equal to the integral of cohesive traction with respect to the separation.

Appendix B

Standard linear solid: creep compliance and free energy

B.0.1 Creep compliance

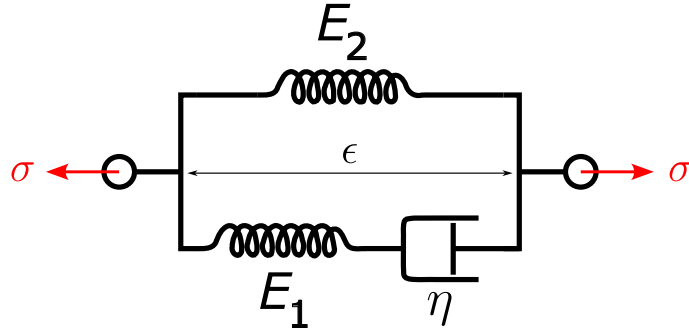


Figure B.1: Schematic representation of the standard linear solid model under uniaxial tension. The differential equation between $\sigma(t)$ and $\epsilon(t)$ is obtained from the spring/dashpot models and the rules of parallel/series components.

Consider a standard linear solid schematized in Fig.(B.1) under uniaxial tension with stress $\sigma(t)$ and strain $\epsilon(t)$. We define the uniaxial creep compliance function $J(t)$ such that

$$\epsilon(t) = \int_0^t J(t-t') \frac{d\sigma(t')}{dt'} dt'. \quad (\text{B.1})$$

On the other hand, to adapt Eq.(3.17) to uniaxial tension, we assume the Poisson's ratio ν of the viscoelastic solid is a time-independent constant. Indeed, the incompressibility assumption implies that $\nu = 1/2$. Consequently, Eq.(3.17) degenerates to the following form

$$(1 + \nu)\epsilon(t) = \int_0^t J_s(t-t') \frac{d\sigma(t')}{dt'} dt', \quad (\text{B.2})$$

Comparing Eq.(B.1) and Eq.(B.2), we conclude that $J_s(t) = (1 + \nu)J(t)$.

The differential equation corresponding to the standard linear solid model under uniaxial tension is,

$$\sigma(t) + \frac{\eta}{E_1} \frac{d\sigma(t)}{dt} = E_2 \epsilon(t) + \frac{\eta}{E_1} (E_1 + E_2) \frac{d\epsilon(t)}{dt}, \quad (\text{B.3})$$

The Laplace transform of Eq.(B.3) gives,

$$\bar{\epsilon}(s) = \frac{1 + \tau s}{E_\infty + E_0 \tau s} \bar{\sigma}(s), \quad (\text{B.4})$$

where s is the Laplace variable, $\tau = \eta/E_1$, $E_\infty = E_2$ and $E_0 = E_1 + E_2$. The Laplace transform of Eq.(B.1) is,

$$\bar{\epsilon}(s) = s \bar{J}(s) \bar{\sigma}(s), \quad (\text{B.5})$$

where $\bar{J}(s)$ is the Laplace transform of the uniaxial creep compliance function $J(t)$. We can now identify that

$$\bar{J}(s) = \frac{1}{s} \frac{1 + \tau s}{E_\infty + E_0 \tau s} \quad (\text{B.6})$$

The inverse Laplace transform of $\bar{J}(s)$ gives the result of Eq.(3.19) in the main text.

B.0.2 Free energy

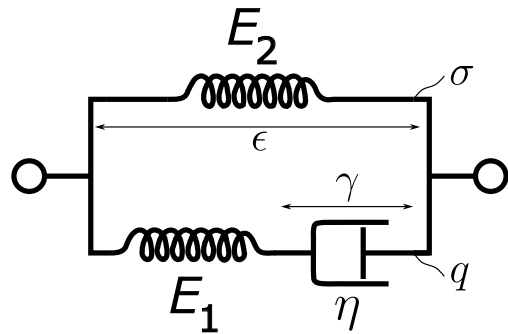


Figure B.2: Standard linear solid model. Total strain ϵ , strain in the dashpot γ , stress in the top branch σ and stress in the Maxwell branch q .

Let us start with the free energy density ψ_{1d} of the one-dimensional (1D) rheological model depicted in Fig.(B.2). It is equal to the sum of the strain energy density stored in both springs with Young's modulus $E_1 = E_0 - E_\infty$ and $E_2 = E_\infty$:

$$\psi_{1d} = \frac{1}{2} \left(\frac{(\sigma - q)^2}{E_\infty} + \frac{q^2}{E_0 - E_\infty} \right), \quad (\text{B.7})$$

where we defined q as the stress in the Maxwell branch containing the spring with constant E_1 and the dashpot. The stress q relaxes over time and therefore is often referred to as the non-equilibrium stress. The ψ_{1d} in Eq.(B.7) can be extended to a form for 3D multi-axial stress states by using the stress tensor \mathbf{S} and the non-equilibrium stress tensor \mathbf{Q} in place of σ and q , respectively. In the 1D form, the strain energy density in each spring is equal to half of the product between the stress and the corresponding strain, e.g., q and $q/(E_0 - E_\infty)$ for the spring E_1 . In the 3D form, the stress-strain product is replaced by a double dot product between the stress and strain tensors for each spring. Because of the incompressibility assumption, only the deviatoric component of the stress tensor produces non-zero double dot product with the stress tensor. Therefore, we replace the stress $\sigma - q$ and q in Eq.(B.7) by $\mathbf{S}^{dev} - \mathbf{Q}^{dev}$ and \mathbf{Q}^{dev} , and the corresponding elastic strain tensors are given by $(1 + \nu)(\mathbf{S}^{dev} - \mathbf{Q}^{dev})/E_\infty$ and $(1 + \nu)\mathbf{Q}^{dev}/(E_0 - E_\infty)$, respectively. The factor $1 + \nu$ originates from the ratio of J_s/J . By setting $\nu = 1/2$, we obtain the free energy density ψ in Eq.(5.4).

To obtain Eq.(3.22) and Eq.(3.23), let us again start from the 1D case. The stress in the Maxwell branch can be written as

$$q = (E_0 - E_\infty)(\epsilon - \gamma), \quad (\text{B.8})$$

where ϵ is the total strain and γ is the strain in the dashpot. We differentiate Eq.(B.8) and apply $\epsilon = (\sigma - q)/E_\infty$ using the spring branch to obtain

$$\dot{q} + \frac{q}{\tau_c} = (1 - \frac{E_\infty}{E_0})\dot{\sigma}, \quad (\text{B.9})$$

where we recognized $\tau_c = \frac{E_0}{E_\infty} \frac{\eta}{E_0 - E_\infty}$. The solution to this first order linear ordinary differential

equation can be found using the initial condition $\sigma(t = 0) = 0$ and $\epsilon(t = 0) = 0$, i.e.,

$$q(t) = \exp\left(-\frac{t}{\tau_c}\right) \int_0^t \exp\left(\frac{t'}{\tau_c}\right) \left(1 - \frac{E_\infty}{E_0}\right) \dot{\sigma}(t') dt'. \quad (\text{B.10})$$

Defining \mathcal{R} as Eq.(3.23), we can rewrite Eq.(B.10) as:

$$q(t) = \mathcal{R}_0 \sigma(t) + \int_0^t \dot{\mathcal{R}}(t - t') \sigma(t') dt', \quad (\text{B.11})$$

which is the 1D form of Eq.(3.22).

When $t \gg \tau_c$, the dashpot is fully extended and $q \rightarrow 0$ while $\psi_{1d} \rightarrow \sigma^2/(2E_\infty)$. When $t \rightarrow 0$, we have $q \rightarrow \mathcal{R}_0 \sigma = (1 - E_\infty/E_0)\sigma$, which, after a couple of omitted rearrangements, yields $\psi_{1d} \rightarrow \sigma^2/(2E_0)$, i.e., the dashpot does not have enough time to extend and both springs store the entire energy without any dissipation. These limiting behaviors can be written in tensorial form as in Eq.(3.24).

Appendix C

Intrinsic energy release rate for the pure shear configuration

Starting from Eq.(3.32), we use Eq.(3.30) for the stress field and Eq.(3.20) for the stress-strain relation to obtain

$$G_0 = \int_{\delta\Omega_l} K(t) \mathbf{d}(\mathbf{X}_c) : \frac{\partial}{\partial X_c} \left[\frac{3}{2} J_0 K(t) \mathbf{d}^{dev}(\mathbf{X}_c) \right] dS_l + \int_{\delta\Omega_l} K(t) \mathbf{d}(\mathbf{X}_c) : \frac{\partial}{\partial X_c} \left[\int_0^t \frac{3}{2} j(t-t') K(t') \mathbf{d}^{dev}(\mathbf{X}_{c'}) dt' \right] dS_l, \quad (\text{C.1})$$

where $\mathbf{d}^{dev} = \mathbf{d} - \text{tr}(\mathbf{d})\mathbf{I}/3$ and $\mathbf{X}_{c'} = \mathbf{X}_c + \Delta c(t, t')\mathbf{e}_1$. Note that $\Delta c(t, t')$ is the difference in the crack length at the current time t and a time t' prior to t , i.e., $\Delta c(t, t') = c(t) - c(t')$. For the first integral in Eq.(C.1), we factor the term $J_0 K^2(t)$ out of the spatial integral. For the second integral in Eq.(C.1), we switch the order of spatial and temporal integrals. As a result, Eq.(C.1) becomes

$$G_0 = J_0 K^2(t) \int_{\delta\Omega_l} \frac{3}{2} \mathbf{d}(\mathbf{X}_c) : \frac{\partial \mathbf{d}^{dev}}{\partial X_c}(\mathbf{X}_c) dS_l + K(t) \int_0^t j(t-t') K(t') \left[\int_{\delta\Omega_l} \frac{3}{2} \mathbf{d}(\mathbf{X}_c) : \frac{\partial \mathbf{d}^{dev}}{\partial X_c}(\mathbf{X}_{c'}) dS_l \right] dt'. \quad (\text{C.2})$$

This is essentially Eq.(3.33) with the two spatial integrals defined in Eq.(3.34) and (3.35). Note that in Eq.(3.34) and (3.35), the surface element dS_l and integration domain $\partial\Omega$ have been rewritten in terms of coordinates \mathbf{X}_c in the translating frame.

Appendix D

Nominal intrinsic energy release rate in the phantom state

We write the nominal intrinsic energy release rate for the phantom state following Eq.(3.32):

$$\hat{G}_0 = \int_{\partial\Omega_l} \mathbf{S} : \frac{\partial \hat{\mathbf{E}}}{\partial X_c} dS_l. \quad (\text{D.1})$$

Using Eq.(3.30) and (3.37), we have

$$\hat{G}_0 = K(t)\mathcal{B}(t)\frac{3}{2} \int_{\mathbf{X}_c} \mathbf{d}(\mathbf{X}_c) : \frac{\partial \mathbf{d}^{dev}}{\partial X_c}(\mathbf{X}_c) d\mathbf{X}_c = K(t)B(t)\mathcal{I}_{cc}, \quad (\text{D.2})$$

where

$$\mathcal{B}(t) = J_0K(t) + \int_0^t \dot{J}(t-t')K(t')dt'. \quad (\text{D.3})$$

Using the identities that $\mathbf{d} = \mathbf{d}^{dev} - \text{tr}(\mathbf{d})\mathbf{I}/3$ and $\mathbf{I} : \mathbf{d}^{dev} = 0$, we can show that

$$\mathbf{d} : \frac{\partial \mathbf{d}^{dev}}{\partial X_c} = \mathbf{d}^{dev} : \frac{\partial \mathbf{d}^{dev}}{\partial X_c} = \frac{1}{2} \frac{\partial(\mathbf{d}^{dev} : \mathbf{d}^{dev})}{\partial X_c}. \quad (\text{D.4})$$

This allows us to carry out the spatial integral \mathcal{I}_{cc} as follows

$$\mathcal{I}_{cc} = \int_{-H/2}^{H/2} \int_{-\infty}^{+\infty} \frac{3}{4} \frac{\partial(\mathbf{d}^{dev} : \mathbf{d}^{dev})}{\partial X_c} dX_c dY_c, \quad (\text{D.5})$$

where we have used the integration domain for an ideal pure shear configuration: $X_c \in (-\infty, +\infty)$ and $Y_c \in (-H/2, +H/2)$. Knowing that \mathbf{d}^{dev} vanishes at $X_c = -\infty$ (i.e., far behind the crack tip) and is independent of Y_c at $X_c = +\infty$, we have

$$\mathcal{I}_{cc} = \frac{3H}{4}(\mathbf{d}^{dev} : \mathbf{d}^{dev})|_{X_c=+\infty} = \frac{3H}{4}(\mathbf{d} : \mathbf{d}^{dev})|_{X_c=+\infty}. \quad (\text{D.6})$$

Therefore, the expression for \hat{G}_0 becomes

$$\hat{G}_0 = \frac{H}{2} (K(t)\mathbf{d}|_{X_c=+\infty}) : \left(\frac{3}{2} \mathcal{B}(t) \mathbf{d}^{dev}|_{X_c=+\infty} \right) = \frac{H}{2} (\mathbf{S} : \hat{\mathbf{E}})|_{X_c=+\infty}. \quad (\text{D.7})$$

Since the actual and phantom state are identical in the far field, we have:

$$\hat{G}_0 = \frac{H}{2} (\mathbf{S} : \mathbf{E})|_{X_c=+\infty}. \quad (\text{D.8})$$

On the other hand, the global energy release rate G in the actual state, as defined in Eq.(3.9), becomes the following form for the pure shear configuration

$$G = \int_{-H/2}^{H/2} \int_{-\infty}^{\infty} \frac{\partial \psi}{\partial X_c} dX_c dY_c = H\psi|_{X_c=+\infty} = \frac{3H}{4E_{\infty}} (\mathbf{S}^{dev} : \mathbf{S}^{dev})|_{X_c=+\infty}, \quad (\text{D.9})$$

where we have used Eq.(3.24) because the material far ahead of the crack tip is fully relaxed.

To compare \hat{G}_0 and G , we note that Eq.(3.20) degenerates to the following form for the fully relaxed material far ahead of the crack tip:

$$\mathbf{E}|_{X_c=+\infty} = \frac{3}{2E_{\infty}} \mathbf{S}^{dev}|_{X_c=+\infty}. \quad (\text{D.10})$$

Therefore, the expression of G becomes

$$G = \frac{H}{2} (\mathbf{S}^{dev} : \mathbf{E})|_{X_c=+\infty} = \frac{H}{2} (\mathbf{S} : \mathbf{E})|_{X_c=+\infty}, \quad (\text{D.11})$$

where we have used the identify that $\mathbf{S}^{dev} : \mathbf{E} = \mathbf{S} : \mathbf{E}$ because $tr(\mathbf{E}) = 0$. Note we can see that \hat{G}_0 and G are identical. Furthermore, denote σ_{∞} and ϵ_{∞} as the vertical tensile stress and strain far ahead of the crack tip ($X_{c1} = +\infty$). The matrices of \mathbf{S} and \mathbf{E} with respect to the Cartesian coordinate system \mathbf{e}_1 , \mathbf{e}_2 and \mathbf{e}_3 in Fig.(3.4a) are

$$[\mathbf{S}]|_{X_{c1}=+\infty} = \begin{bmatrix} \sigma_{\infty}/2 & 0 & 0 \\ 0 & \sigma_{\infty} & 0 \\ 0 & 0 & 0 \end{bmatrix}, [\mathbf{E}]|_{X_{c1}=+\infty} = \begin{bmatrix} 0 & 0 & 0 \\ 0 & \epsilon_{\infty} & 0 \\ 0 & 0 & -\epsilon_{\infty} \end{bmatrix}. \quad (\text{D.12})$$

Eq.(D.10) implies that $\epsilon_{\infty} = 3\sigma_{\infty}/4E_{\infty}$. As a result, we obtain

$$G = \hat{G}_0 = \frac{H}{2} \sigma_{\infty} \epsilon_{\infty} = \frac{2H}{3} E_{\infty} \epsilon_{\infty}^2. \quad (\text{D.13})$$

This is Eq.(3.38) in the main text. Additionally, combining Eq.(3.33), (D.2) and (D.3), we obtain Eq.(3.39) in the main text.

Appendix E

Derivatives of spatial distribution

To evaluate the spatial integrals in Eq.(3.34) and (3.35), we need to determine the partial derivative $\partial \mathbf{d}/\partial X_c$. In this section we provide the values of these derivatives for the LEFM approximation \mathbf{f} given as Eq.(3.36). We have,

$$X_c = r \cos \theta, \quad (\text{E.1})$$

$$\frac{\partial \mathbf{f}^{dev}}{\partial X_c} = \frac{\partial \mathbf{f}^{dev}}{\partial r} \cos \theta - \frac{\partial \mathbf{f}^{dev}}{\partial \theta} \frac{\sin \theta}{r}. \quad (\text{E.2})$$

The components of $\partial \mathbf{f}^{dev}/\partial r$ can be written as:

$$\frac{\partial f_{11}^{dev}}{\partial r} = -\frac{1}{2} \frac{\cos(\frac{\theta}{2})}{(2\pi r)^{3/2}} \left(\frac{1}{3} - \sin \frac{\theta}{2} \sin \frac{3\theta}{2} \right), \quad (\text{E.3})$$

$$\frac{\partial f_{22}^{dev}}{\partial r} = -\frac{1}{2} \frac{\cos(\frac{\theta}{2})}{(2\pi r)^{3/2}} \left(\frac{1}{3} + \sin \frac{\theta}{2} \sin \frac{3\theta}{2} \right), \quad (\text{E.4})$$

$$\frac{\partial f_{12}^{dev}}{\partial r} = -\frac{1}{2} \frac{\cos(\frac{\theta}{2})}{(2\pi r)^{3/2}} \sin \frac{\theta}{2} \cos \frac{3\theta}{2}. \quad (\text{E.5})$$

The components of $\partial \mathbf{f}^{dev}/\partial \theta$ can be written as:

$$\begin{aligned} \frac{\partial f_{11}^{dev}}{\partial \theta} &= \frac{1}{\sqrt{2\pi r}} \left[-\frac{1}{2} \sin \frac{\theta}{2} + \frac{1}{2} (\sin \frac{\theta}{2})^2 \sin \frac{3\theta}{2} - \frac{1}{2} (\cos \frac{\theta}{2})^2 \sin \frac{3\theta}{2} \right. \\ &\quad \left. - \frac{3}{2} \cos \frac{\theta}{2} \sin \frac{\theta}{2} \cos \frac{3\theta}{2} \right], \end{aligned} \quad (\text{E.6})$$

$$\begin{aligned} \frac{\partial f_{22}^{dev}}{\partial \theta} &= \frac{1}{\sqrt{2\pi r}} \left[-\frac{1}{2} \sin \frac{\theta}{2} - \frac{1}{2} (\sin \frac{\theta}{2})^2 \sin(\frac{3\theta}{2}) + \frac{1}{2} (\cos \frac{\theta}{2})^2 \sin(\frac{3\theta}{2}) \right. \\ &\quad \left. + \frac{3}{2} \cos(\frac{\theta}{2}) \sin(\frac{\theta}{2}) \cos(\frac{3\theta}{2}) \right], \end{aligned} \quad (\text{E.7})$$

$$\frac{\partial f_{12}^{dev}}{\partial \theta} = \frac{1}{\sqrt{2\pi r}} \left[-\frac{1}{2} (\sin \frac{\theta}{2})^2 \cos \frac{3\theta}{2} + \frac{1}{2} (\cos \frac{\theta}{2})^2 \cos(\frac{3\theta}{2}) - \frac{3}{2} \cos(\frac{\theta}{2}) \sin(\frac{\theta}{2}) \sin(\frac{3\theta}{2}) \right]. \quad (E.8)$$

Appendix F

Gains in computational time

F.0.1 Computational time for the numerical method

In the implicit method used to solve for $c(t)$, the bottleneck is the golden section search procedure (GSS). While this was expected, this claim was verified by running Python's deterministic profiling method *cProfile*. The GSS finds the minimum of the following function:

$$f_{gss}(\delta c_k) = \left| G_d^s(t_k) - K(t_k) \sum_{s=0}^k J_{t_k-t'_s} K(t'_s) \mathcal{D}_{cc'}(t_k, t'_s) \delta t \right|, \quad (\text{F.1})$$

where $\delta c_k = c_k - c_{k-1}$ is a guess for the crack extension at time t_k . The time it takes for our method to solve for $c(t)$ is directly proportional to how often we need to run the GSS procedure, and how many iterations it takes to find the minimum.

Note that, for times where $G_d^s(t_k) = 0$, we can set $\delta c_k = 0$ without minimizing any function. In the plot $K(t)$, we notice geometrically that $G_d^s(t) > 0$ happens for a fraction $\Delta = 1 - \sqrt{\Gamma_0/G_{max}}$ of each cycle (assuming $G_{max}/\Gamma_0 > 1$). Therefore, the number of time steps such that $G_d^s(t_k) > 0$ is

$$n_{st} = \lfloor \frac{N_{cy} T}{dt} (1 - \sqrt{\frac{\Gamma_0}{G_{max}}}) \rfloor, \quad (\text{F.2})$$

where N_{cy} is the number of cycles and $\lfloor \bullet \rfloor$ denotes the floor function.

We denote T_{gss} the time required to minimize f_{gss} using the GSS method. For our unimodal function, the method will converge toward the solution by reducing the size of the interval by a factor $(\sqrt{5} - 1)/2$ at each iteration. We consider an initial interval $[\delta c_L, \delta c_U] = [0, 5000l]$. We could estimate T_{gss} if we knew the tolerance in terms of the final acceptable size of this interval.

However, for accuracy, we decided to define the acceptable error relatively to the solution: $e_a = |\delta c_U - \delta c_L|/\delta c^{sol} < 10^{-4}$. Therefore the minimum number of iterations for convergence cannot be known *a priori*.

There are cases however, when the solution is $\delta c^{sol} = 0$. In these cases, the definition of e_a causes the method to over shrink the interval, and therefore we replaced the termination condition by $|\delta c_U - \delta c_L| < 10^{-20}$. Since such cases have an absolute termination condition, we may compute that it takes \mathcal{M} iterations to converge below the threshold with

$$\mathcal{M} > \frac{\ln(10^{-20}) - \ln(|\delta c_U - \delta c_L|)}{\ln(\sqrt{5} - 1) - \ln(2)}. \quad (\text{F.3})$$

With the parameters chosen, it takes 114 iterations to converge to the boundary of the interval which, with our hardware (Lenovo ThinkStation P620), corresponds to $6.2 \times 10^{-2}s$. Since, for $\delta c^{sol}/l > 10^{-15}$ we have $e_a > 10^{-20}$, we may write $T_{gss} < 6.2 \times 10^{-2}s$. Therefore we can expect a solution for $c(t)$ in $T_{sol} \leq 6.2n_{st} \times 10^{-2}s$. We can verify for a single cycle with $T = 100s$, $dt = 0.25s$ and $G_{max}/\Gamma_0 = 2$: it takes $3.61s$ with our hardware. Indeed, $3.61s < 6.2n_{st} \times 10^{-2} = 7.25s$.

Simulations with different parameters can be run in parallel. Therefore, to obtain one of the $dc/dN - G_{max}$ curves (e.g., Figs.(3.8a,e), Fig.(3.9) and Fig.(3.11a)), we can estimate the computational time by dividing the number of points on the curve by the number of available CPUs running in parallel and multiplying by T_{sol} . Note that T_{sol} may be larger than $3.61s$ if more than a cycle is required by the definition of dc/dN . In practice, the order of magnitude required to obtain a curve with 100 points (G_{max} values) with 20 CPUs is $\sim 100s$ with our hardware. In comparison, the order of magnitude to obtain such a result experimentally is between ~ 1 day (ignoring the near-threshold part) and ~ 100 days (for the full curve) [126].

F.0.2 Computational time for the FEA simulation

The computational time required to obtain $c(t)$ using the FEA model developed by Guo *et al* [49] depends on the time step dt at which outputs are written, the loading conditions, the domain and mesh sizes. While we may set the loading conditions and the time resolution similarly

to our numerical method, we have no relevant mesh or domain size to compare in the implicit method. A rigorous study of the influence of these parameters on the quality of the $c(t)$ solution is not within the scope of this work. Therefore we limit the discussion to orders of magnitude. To obtain the results of Fig.(3.7), it took $13s$ with our numerical method and $3258s$ with the FEA simulation (~ 250 times longer with the same hardware). One may argue that the domain size could be reduced in the simulation if we limit ourselves to 3 loading cycles. From Fig.(3.7d), it is also clear that reducing the size of the cohesive elements is required to reach the same accuracy as our numerical method on $V(t)$.

Appendix G

Influence of the ratio T/τ : supplementary data

The insensitivity of $d\bar{c}/dN$ to the ratio T/τ exhibited in Fig.(3.9b) is found for various ratio E_0/E_∞ .

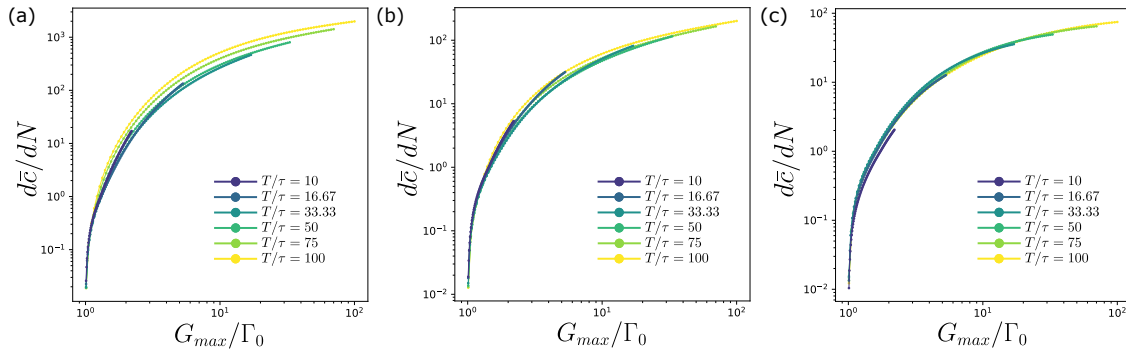


Figure G.1: (a) Increase in normalized crack length $\bar{c} = c/l$ per cycle N with normalized maximum global energy release rate G_{max}/Γ_0 , for varying T/τ and $E_0/E_\infty = 2$. (b) Same result for $E_0/E_\infty = 4$. (c) Same result for $E_0/E_\infty = 12$.

Appendix H

Table of parameters for the finite element simulations

SIM	<i>L</i>	<i>H</i>	<i>c</i> ₀	<i>h</i>	<i>h</i> _c	δ	σ	$\dot{\lambda}$	Γ_0	α	Figures
A	50.0	5.0	10.0	0.05	1.0	0.4	10.0	0.02	2.0	0.4	Fig.4.4
B	*	2.5	10.0	0.1	1.0	1.8	6.0	0.0352	5.4	1.0	Fig.4.5
C	50.0	5.0	10.0	0.01	1.0	0.4	10.0	0.005	2.0	*	Fig.4.6(a-c)
D	50.0	5.0	10.0	*	1.0	0.4	10.0	0.005	2.0	0.0	Fig.4.6(d,e)
E	50.0	5.0	10.0	0.01	1.0	*	*	0.005	2.0	0.0	Fig.4.6(f)
F	50.0	5.0	10.0	0.05	1.0	0.4	10.0	0.02	2.0	*	Fig.4.7
G	50.0	*	10.0	0.05	1.0	0.4	10.0	0.02	2.0	0.2	Fig.4.8, Fig.4.9
Units	[mm]	[mm]	[mm]	[mm]	[mm]	[mm]	[MPa]	[s ⁻¹]	[kJ/m ²]	[−]	N/A

Table H.1: Simulations parameters. Symbols * indicates the parameter was varied in the simulation, values are reported on the relevant figures. Throughout all simulations the thickness of the sample $w = 0.1\text{mm}$ and the shear modulus at low strain $\mu = 1\text{MPa}$ have been kept constant.